Institut für Osteologie und Biomechanik
Zentrum für experimentelle Medizin
Universitätsklinikum Hamburg-Eppendorf

Characterization of genetically modified mice carrying pathogenic mutations in the *Notch2* or *Wnt1* gene

Dissertation

zur Erlangung der Würde des Doktorgrades
an der Fakultät für Mathematik, Informatik und Naturwissenschaften
Fachbereich Chemie
an der Universität Hamburg

vorgelegt von
Nele Mareike Vollersen
aus Husum

Hamburg, 2018

Datum der Disputation: 14.12.2018

Datum der Druckfreigabe: 14.12.2018

1. Gutachter: Prof. Dr. rer. nat. Thorsten Schinke

2. Gutachter: Prof. Dr. rer. nat. Peter Heisig

Diese Dissertation wurde zwischen Februar 2016 und Oktober 2018 im Institut für Osteologie und Biomechanik am Universitätsklinikum Hamburg-Eppendorf unter Anleitung von Prof. Dr. rer. nat. Thorsten Schinke durchgeführt.

I. List of Publications

Publications

Yorgan, T., **N. Vollersen**, C. Riedel, A. Jeschke, S. Peters, B. Busse, M. Amling, and T. Schinke, *Osteoblast-specific Notch2 inactivation causes increased trabecular bone mass at specific sites of the appendicular skeleton.* Bone, 2016. **87**: p. 136-46.

Vollersen, N., I. Hermans-Borgmeyer, K. Cornils, B. Fehse, T. Rolvien, I. Triviai, A. Jeschke, R. Oheim, M. Amling, T. Schinke, and T.A. Yorgan, *High Bone Turnover in Mice Carrying a Pathogenic Notch2 Mutation Causing Hajdu-Cheney Syndrome.* J Bone Miner Res, 2018. **33**(1): p. 70-83.

Luther, J., T. A. Yorgan, T. Rolvien, L. Ulsamer, T. Koehne, N. Liao, D. Mau, **N. Vollersen**, S. Teufel, M. Neven, S. Peters, M. Schweizer, A. Trumpp, S. Rosigkeit, E. Bockamp, S. Mundlos, U. Kornak, R. Oheim, M. Amling, T. Schinke, and J. P. David, *Wnt1 is an Lrp5-independent bone-anabolic Wnt ligand.* (Submitted).

Vollersen, N., F. Schmidt, T. Rolvien, S. Sonntag, D. Shmerling, R. Oheim, A- Sharaf, M. Karsak, B. Busse, J. P. David, M. Amling, T. Schinke, T. A. Yorgan, *A new mouse model of osteogenesis imperfecta type XV with moderate osteopenia and a high skeletal fracture rate*. (Manuscript in preparation).

Poster Presentation

American Society for Bone and Mineral Research (ASBMR)

Annual Meeting 2016, Atlanta, Georgia, United States of America.

Poster presentation: "*High bone turnover in mice carrying a pathogenic Notch2-mutation causing Hajdu-Cheney syndrome."*

European Calcified Tissue Society (ECTS)

Annual Meeting 2018, Valencia, Spain.

Poster presentation: "*Low bone mass in mice with conditional Wnt1 deletion and an autosomal dominant WNT1 mutation causing early-onset osteoporosis*."

Oral Presentation

European Calcified Tissue Society (ECTS)

Annual Meeting 2018, Valencia, Spain.

Presentation entitled: "*Low bone mass in mice with conditional Wnt1 deletion and an autosomal dominant WNT1 mutation causing early-onset osteoporosis*."

14. Hamburger Studierendentagung zur innovativen Medizin & Biotechnologie

2017, Hamburg, Germany

Presentation entitled: „*Untersuchungen zur Aufklärung des erhöhten Knochenumsatzes in Notch2^{HCS}-Mäusen*."

II. Table of Contents

III. Abbreviations

µCT	Micro-computed tomography
AL	Alendronate
Alpl	Alkaline Phosphatase
BAT	Brown adipose tissue
BFR/BS	Bone formation rate per bone surface
Bglap	Osteocalcin
BMD	Bone mineral density
BMT	Bone marrow transplantation
BMU	Bone multicellular unit
bp	Base pairs
Bsp	Bone sialoprotein
BV/TV	Bone volume per tissue volume
Ca_{Mean}	Mean calcium concentration
Cbfa1	Core-binding factor subunit-α 1
cDNA	complementary DNA
Col1a1	Collagen type I α1
Col1a2	Collagen type I α2
Ct.Por	Cortical porosity
Ct.Th	Cortical thickness
Ctrl	Control
CTx	C-terminal telopeptides (Crosslaps)
Cux1	Cut like homeobox 1
DCX	Doublecortin
dd H_2O	Double destilled H_2O
Dex	Dexamethasone
Dkk1	Dickkopf 1
Dll1	Delta-like 1
Dlx5	Distal-less homeobox 5
Dmp1	Dentin matrix protein 1
DNA	Deoxyribonucleic acid
DXA	Dual-energy X-ray absorptiometry
ELISA	Enzyme-linked immunosorbent assay
EOOP	Early-onset osteoporosis
Fgf23	Fibroblast growth factor 23
F_{max}	Maximum force bone can withstand
FTH	Forschungstierhaltung
FTIR	Fourir-transform infrared spectroscopy
fx	Fracture
Gapdh	Glycerinaldehyde-3-phosphate-dehydrogenase
GP/Th	Growth plate thickness
HBM	High bone mass
HCS	Hajdu-Cheney syndrome
IGF-1	Insulin-like growth factor 1
IL	Interleukin
Lrp5	Low-density lipoprotein receptor-related protein 5

Maml	Mastermind-like
M-csf	Macrophage-colony stimulating factor
Mmp9	Matrix metalloprotease 9
Ms.D	Midshaft diameter
MSC	Mesenchymal stem cell
N.Ad/M.Ar	Number of adipocytes per marrow area
N.Ob/B.Pm	Number of osteoblasts per bone perimeter
N.Oc/B.Pm	Number of osteoclasts per bone perimeter
N.Ot/B.Ar	Number of osteocytes per bone perimeter
NICD	Notch intracellular domain
Oc.S/BS	Osteoclast surface per bone surface
OI	Osteogenesis Imperfecta
OI type XV	Osteogenesis Imperfecta type XV
Opg	Osteoprotegerin
OPPG	Osteoporosis pseudoglioma syndrome
Osx	Osterix
PCR	Polymerase chain reaction
PEST	Proline-, glutamine-, serine-, threonine-rich
PINP	Procollagen-I N-terminal propeptide
PTH(1-34)	Parathyroid hormone
Pth1r	Parathyroid hormone 1 receptor
PTHrP	Parathyroid hormone-related protein
PVDF	Polyvinylidene difluoride
qBEI	Quantitative backscattered electron imaging
qRT PCR	Quantitative real time PCR
r.e.	Relative expression
Rank	Receptor activator of NF-κB
Rankl	Receptor activator of NF-κB ligand
rec.	recombined
RIPA	Radio-immunoprecipitation assay
RNA	Ribonucleic acid
Runx2	Runt-related transcription factor 2
S1p	Sphingosine 1-phosphate
S1pr3	Sphingosine 1-phosphate receptor 3
SDS PAGE	Sodiumdodecyl sulfate-polyacrylamide gel electrophoresis
SGZ	Subgranular zone
SLR	Signal log ratio
Sost	Sclerostin
Sw	Swaying
TGF-β1	Transforming growth factor-β1
Tnfsf11	gene encoding Rankl
TNF-α	Tumor necrosis factor α
Trap	Tartrate resistant acid phosphatase
VitD	1,25-$(OH)_2$ vitamin D_3
WAT	White adipose tissue
$W_{Rp0.2}$	Work until plastic deformation

1 Abstract

Bone is a highly dynamic tissue that constantly undergoes a physiologically relevant remodeling process mediated by coordinated activities of bone-forming osteoblasts and bone-resorbing osteoclasts. Imbalanced activities of these two cell types can cause a variety of skeletal disorders among which osteoporosis shows the highest prevalence and socio-economic impact. On a cellular level, osteoporosis is caused by a relative increase of bone resorption over bone formation resulting in decreased bone mineral density and increased skeletal fracture risk. Since underlying mechanisms causing this pathology are highly variable, understanding the mode of action of osteoblasts and osteoclasts is of high importance. This also includes the identification of regulatory molecules and signaling pathways controlling the function of these two cell types.

Notch signaling was long known for its impact in neuronal development, where it controls intracellular communication. Only recently, its role in bone remodeling was uncovered by the identification of a pathogenic *NOTCH2* mutation in individuals with Hajdu-Cheney syndrome (HCS). More specifically, HCS is a rare autosomal dominant disorder primarily affecting the skeleton, since patients display early-onset osteoporosis, acro-osteolyses, short stature, and coarse facies. All identified *NOTCH2* mutations causing HCS result in the absence of the C-terminal PEST-domain, which is required for proteasomal degradation of the protein. Consequently, these mutations are predicted to result in a prolonged NOTCH2 signal. To understand the role of NOTCH2 in bone remodeling, a mouse model carrying a pathogenic 6272delT mutation in *Notch2*, causing HCS in humans, was generated and analyzed. Studies of the skeleton of these mice revealed generalized osteopenia caused by a high bone turnover, *i.e.* osteoblast and osteoclast indices were both increased. After ruling out cell-autonomous gain-of-functions in either osteoblasts or osteoclasts, RNA sequencing revealed increased expression of the pro-osteoclastogenic genes *Tnfsf11* and *Il6* in bone marrow cells obtained from *Notch2*$^{+/HCS}$ mice cultured under osteogenic conditions. Furthermore, anti-resorptive alendronate treatment fully corrected the high bone turnover phenotype observed in *Notch2*$^{+/HCS}$ mice, which is potentially explained by impaired release of osteoclast-derived factors coupling bone formation to bone resorption. Analyses of two osteoclast-derived coupling factors, S1P and Wnt1, did however not reveal any impact on the bone phenotype of *Notch2*$^{+/HCS}$ mice.

In the context of this study, it was however important that analysis of mice lacking *Wnt1* either in the osteoclast or osteoblast lineage revealed remarkable results. In fact, while Wnt1 inactivation in osteoclasts did not affect bone remodeling, all mice with Wnt1 inactivation in osteoblasts displayed low bone mass and various skeletal fractures. Since *WNT1* mutations were previously identified in patients with osteogenesis imperfecta type XV (OI type XV), the final part of this thesis aimed at generating and analyzing a mouse model of this disorder, which was achieved by introducing a pathogenic mutation (G177C) into the murine *Wnt1* gene. The resulting $Wnt1^{G177C/G177C}$ mice exhibited a moderate reduction of trabecular and cortical bone mass, explained by reduced osteoblast activity. Most importantly, the majority of 24 weeks old $Wnt1^{G177C/G177C}$ mice displayed skeletal fractures in various locations, suggesting that Wnt1 primarily controls bone matrix quality. This newly developed mouse model of OI type XV was further utilized to demonstrate that the $Wnt1^{G177C/G177C}$ mutation does not interfere with the osteoanabolic influence of parathyroid hormone 1-34 (PTH (1-34)) treatment, both *in vitro* and *in vivo*.

Taken together, the results of this thesis demonstrate that the low bone mass phenotypes of $Notch2^{+/HCS}$ and $Wnt1^{G177C/G177C}$ mice are explained by different underlying mechanisms. Whereas the $Notch2^{+/HCS}$ mutation favors pro-osteoclastogenic gene expression, triggering a high bone turnover pathology, the $Wnt1^{G177C/G177C}$ mutation specifically affects bone formation and bone matrix quality. In both cases, the mouse models were additionally used to demonstrate possible treatment options, *i.e.* bisphosphonate administration for HCS and daily PTH(1-34) injections for OI type XV.

2 Zusammenfassung

Knochen ist ein hochdynamisches Gewebe, welches einem stetigen Umbau unterliegt. Dieser physiologisch relevante Prozess wird von knochenformenden Osteoblasten und knochenresorbierenden Osteoklasten vermittelt. Gerät jedoch die Aktivität dieser beiden Zelltypen aus dem Gleichgewicht, können erhebliche Störungen des Skelettsystems entstehen. Unter diesen Störungen stellt Osteoporose die am häufigsten vorkommende skelettale Krankheit mit der höchsten sozial-ökonomischen Auswirkung dar. Auf zellulärer Ebene wird Osteoporose durch eine erhöhte Knochenresorption gegenüber der Knochenformation verursacht. Dies hat eine verringerte Knochenmasse und ein erhöhtes Frakturrisiko zur Folge. Da die Auslöser dieser Störung unterschiedlichsten Ursprungs sein können, ist die Erforschung von Funktionsweisen sowie die Identifizierung regulatorischer Moleküle und Signalwege, die die Aktivität von Osteoblasten und Osteoklasten beeinflussen, von enormer Bedeutung.

Notch-Signale waren lange für ihren Einfluss auf die neuronale Entwicklung bekannt, bei der sie die intrazelluläre Kommunikation kontrollieren. Erst kürzlich wurde ihre Rolle im Knochenmetabolismus durch die Identifizierung von Mutationen im *NOTCH2*-Gen, welche zum Hajdu-Cheney Syndrom (HCS) führen, aufgedeckt. Hierbei handelt es sich um eine seltene autosomal-dominante Erkrankung, die sich primär durch früh einsetzende Osteoporose, Acro-Osteolysen, Minderwuchs und grobe Gesichtszüge auszeichnet. Alle bereits identifizierten HCS-assoziierten *NOTCH2*-Mutationen führen zum Fehlen der C-terminalen PEST-Domäne, welche für den proteasomalen Abbau des Proteins verantwortlich ist. Daraus resultiert ein anhaltendes NOTCH2-Signal im Patienten. Um die Rolle von *NOTCH2* während des Umbaus von Knochen genauer zu verstehen, wurde ein Mausmodell generiert und analysiert, welches eine pathogene 6272delT Mutation im *Notch2*-Gen trägt, die im Menschen zu HCS führt. Skelettale Untersuchungen ergaben einen erhöhten Knochenumsatz, der durch eine erhöhte Osteoblasten- und Osteoklastenanzahl verursacht wird und in einer Osteopenie resultiert. Nachdem zellautonome Störungen in beiden Zelltypen ausgeschlossen werden konnten, wurden osteogen-kultivierte Knochenmarkszellen aus *Notch2*$^{+/HCS}$-Mäusen mittels RNA-Sequenzierung analysiert und eine erhöhte Expression von *Tnfsf11* und *Il6* festgestellt. Diese beiden Faktoren sind für die Unterstützung der Osteoklastogenese bekannt. Darüber hinaus konnte in dieser Arbeit

gezeigt werden, dass eine anti-resorptive Behandlung von *Notch2*$^{+/HCS}$-Mäusen mit Alendronat den erhöhten Knochenumsatz in *Notch2*$^{+/HCS}$-Mäusen korrigiert. Diese Korrektur wird vermutlich durch eine verminderte Freisetzung von osteoklastären Faktoren, die Knochenformation und Knochenresorption miteinander koppeln, vermittelt. Allerdings wiesen Untersuchungen der Kopplungsfaktoren S1P und Wnt1 keinen Einfluss in Bezug auf den Knochenphänotypen von *Notch2*$^{+/HCS}$-Mäusen auf.

In Zusammenhang mit den eben beschriebenen Untersuchungen lieferte die Analyse von Mäusen mit einem inaktivierten *Wnt1*-Gen im Osteoklasten bzw. im Osteoblasten bemerkenswerte Ergebnisse. Während eine Wnt1-Inaktivierung im Osteoklasten den Umbau des Knochens nicht beeinflusste, konnten in allen Mäusen, die eine Wnt1-Inaktivierung im Osteoblasten trugen, eine verringerte Knochenmasse und diverse Frakturen nachgewiesen werden. Da im Menschen kürzlich Mutationen im *WNT1*-Gen identifiziert wurden, die zu Osteogenesis Imperfecta Typ XV (OI Typ XV) führen, beschäftigt sich der letzte Teil dieser Arbeit mit der Generierung und Untersuchung eines Mausmodells, welches eine mit OI Typ XV-assoziierte Mutation (G177C) im *Wnt1*-Gen trägt. Resultierende *Wnt1*$^{G177C/G177C}$-Mäuse wiesen eine moderat verminderte trabekuläre und kortikale Knochenmasse auf, die durch eine verminderte Aktivität von Osteoblasten erklärt werden konnte. Zusätzlich wiesen diese Mäuse im Alter von 24 Wochen skelettale Frakturen in verschiedenen Regionen auf, wodurch die Rolle von Wnt1 in Bezug auf die Knochenqualität verdeutlicht wurde. Des Weiteren konnte mit diesem OI Typ XV-Mausmodell gezeigt werden, dass die Mutation sowohl *in vitro* als auch *in vivo* keinen Einfluss auf die osteoanabole Wirkung des Parathormonfragments 1-34 (PTH(1-34)) hat.

Zusammenfassend zeigt diese Arbeit, dass der verringerten Knochenmasse in *Notch2*$^{+/HCS}$- und *Wnt1*$^{G177C/G177C}$-Mäusen unterschiedliche Mechanismen zugrunde liegen. Während Osteoblasten von Mäusen, die die *Notch2*$^{+/HCS}$-Mutation tragen, vermehrt Gene exprimieren, die die Osteoklastogenese unterstützen und dadurch den erhöhten Knochenumsatz veranlassen, führt die *Wnt1*$^{G177C/G177C}$-Mutation zu einer beeinträchtigten Knochenformation und Knochenqualität. In beiden Fällen wurden die Mausmodelle zusätzlich verwendet, um potenzielle Behandlungsmöglichkeiten, wie beispielsweise eine Bisphosphonatgabe für HCS-Patienten und eine tägliche PTH(1-34)-Injektion für Patienten mit OI typ XV, aufzuzeigen.

3 Introduction

3.1 Skeletal system

The skeleton is a complex and multifunctional system composed of bones, cartilage, tendons, and ligaments. Whereas bone provides structural support for the complete body, cartilage provides flexibility for locomotion and is found between joints and the vertebral bodies. Ligaments, however, surround joints and hold skeletal components together. All components enable movement and serve as a protection of internal organs from external injuries. Moreover, bone tissue serves as a reservoir of minerals, especially calcium and phosphorus. If required, incorporated minerals can be released into the blood circulation for different physiological processes[1].

3.2 Bone anatomy and physiology

3.2.1 Bone structure

Bones are divided into different categories based on their shape and function. These categories include long bones (humerus, ulna, radius, femur, tibia, fibula, metacarpus, phalanges, metatarsus), short bones (carpus and tarsus), flat bones (cranium, scapulae, sternum, costae), irregular bones (vertebrae and mandible), and sesamoid bones (patellae)[2].

More specifically, long bones comprise the medullary cavity, which is located between the proximal and distal ends of the bone, termed diaphysis. The end parts of a long bone are termed the proximal and distal epiphyses. In contrast to the diaphysis, the epiphyses contain spongy trabecular bone together with bone marrow[1]. Both epiphyses encounter the diaphysis at the metaphyses, where bone elongation occurs during growth. The specific region of bone elongation is termed growth plate, where chondrocytes undergo a coordinated program of proliferation, differentiation, and hypertrophy. Is the bone fully grown, an epiphyseal line remains in the metaphysis (Figure 1).

The outer walls of bone are composed of very dense cortical bone, except for epiphyseal region that is in contact with other bones, which is covered with articular cartilage[2].

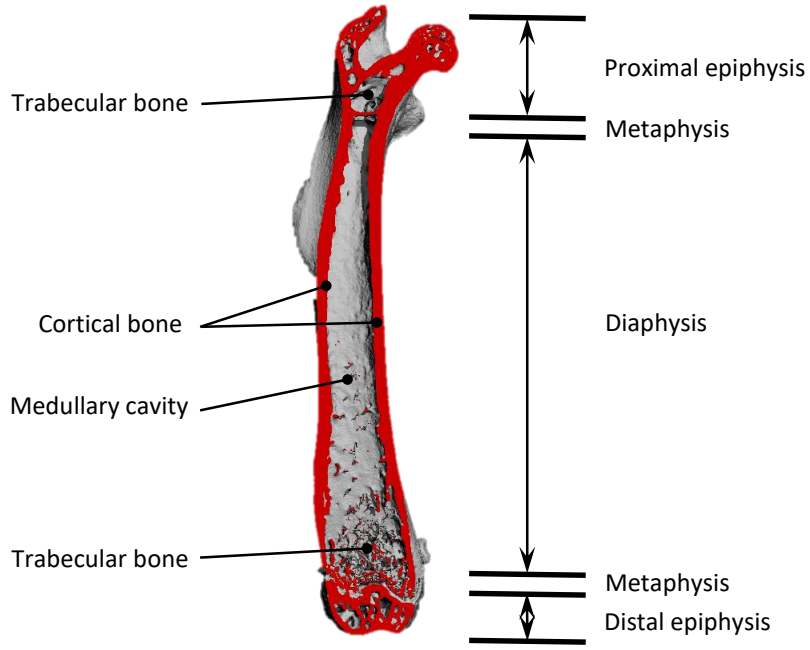

Figure 1: Macroscopic structure of a murine long bone. Representative µCT image showing anatomical parts of a long bone consisting of epiphyses, metaphyses, and the diaphysis. It also shows the structural composition with trabecurlar bone, cortical bone, and the medullary cavity.

3.2.2 Bone composition

The bone matrix is composed of 50 to 70 % mineral, 20 to 40 % organic matrix, 5 to 10 % water, and <3 % lipids[2].The mineral component mostly consists of small hydroxyapatite crystals developing when calcium and phosphate combine. These crystals represent the rigid part of the bone. In contrast, the organic matrix of bone consists of 85 to 90 % collagenous proteins, mostly collagen type I[3]. Other collagen types present in the organic matrix are type X, type III and type V. The remaining 10 to 15 % of organic matrix are non-collagenous proteins like proteoglycans, glycosylated proteins, and γ-carboxylated proteins. Hence, the organic matrix of bone provides a scaffold for the mineral[2].

3.2.3 Collagen synthesis

The process of collagen synthesis starts with the transcription of the genes *COL1A1* and *COL1A2*, encoding the α1 and α2 chains of collagen. The transcripts are further translated to pre-pro-polypeptide chains. The amino acid sequence of basic collagen molecules is either glycine-proline-X or glycine-X-hydroxyproline, at which X means any of the other 17 amino acids. After post-translational modification, the chains form a triple helix consisting of 2 pro-α1 chains and 1 pro-α2 chain. The newly formed procollagen molecule is further modified at the Golgi apparatus, before it is secreted into the extracellular space. Here, collagen peptidases remove the ends of the procollagen molecule, forming tropocollagen. The

collagen fibril arises by covalent bonding between tropocollagen molecules, whereas the collagen fiber consists of several collagen fibrils[4] (Figure 2).

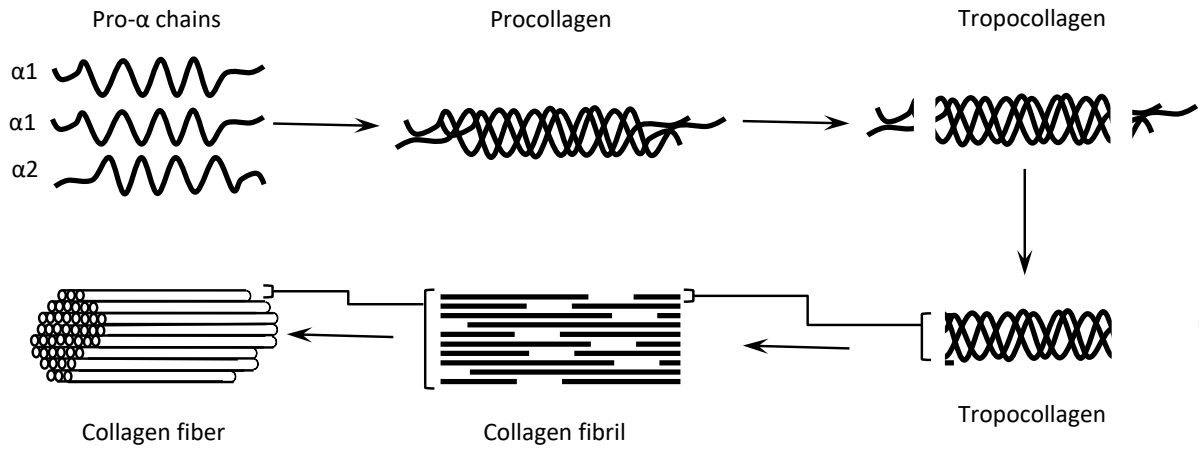

Figure 2: Synthesis of collagen type I. 2 pro-α1 chains and 1 pro-α2 chain self-assemble to form a triple helix, termed procollagen. When collagen peptidases remove the ends of procollagen, tropocollagen is formed. Several tropocollagen molecules form a collagen fibril. Several collagen fibrils self-assemble to from a collagen I fiber.

3.2.4 Bone mineralization

The bone matrix mineralizes in two principle steps. Firstly, hydroxyapatite crystals are formed within extracellular matrix vesicles. Although the process of hydroxyapatite formation is not completely understood, it is known that accumulation of calcium within the matrix vesicles requires calcium-binding proteins, calcium-binding phospholipids and calcium-forming annexins, whereas the intake of phosphate requires a Type III sodium/phosphate co-transporter and PHOSPHO1 phosphatase[5, 6]. If successful, accumulation of calcium and phosphate exceeds the point of solubility and hydroxyapatite is formed within the vesicles. As hydroxyapatite crystals expand, they are released into the extracellular space where they fill the gaps between collagen fibers, thereby hardening the tissue.

3.3 Bone cells

Bone contains several types of cells, *e.g.* bone-forming osteoblasts, bone-resorbing osteoclasts, and mechano-sensitive osteocytes. Together, these cells ensure a balance in bone formation and bone resorption.

3.3.1 Osteoblasts

Osteoblasts and several other celltypes including adipocytes, myocytes, fibroblasts, and chondrocytes arise from mesenchymal stem cells (MSCs). Therefore, the differentiation and proliferation event of each cell type has to be highly regulated and needs a definite program of gene expression[1, 7]. In case of MSC-commitment towards osteprogenitors, the synthesis of bone morphogenic proteins (BMPs) and members of the Wnt/β-catenin signaling pathway (Wnt10b, Wnt5a) are crucial[8]. Furthermore, during this commitment the activation of transcription factors like runt-related transcription factor 2 (Runx2), distal-less homeobox 5 (Dlx5) and osterix (Osx) are of high importance[9]. *Runx2*, also known as *core-binding Factor Subunit-α 1* (*Cbfa1*), was identified in 1997 as the master gene of osteoblast differentiation. It is pivotal in the early stages of osteoblast development as *Runx2*-null mice are completely deprived of osteoblasts[10]. Runx2 further induces the expression of osteoblast-related genes like *osteocalcin* (*Bglap*), *collagen type I* (*Col1a1*), *bonesialoprotein* (*Bsp*) and *alkaline phosphatase* (*Alp*)[11]. Another transcription factor activated by BMPs during MCS-commitment towards osteoprogenitors is Osx, also known as Sp7. As it is not expressed in *Runx2*-null mice, it is supposed to act downstream of Runx2[12]. Furthermore, Osx is responsible for the development and proliferation of immature osteoblasts, but likewise inhibits these from differentiating into mature osteoblasts[13].

Mature osteoblasts represent 4 to 6 % of total bone cells, have a cuboidal shape, and are found in clusters of more than hundred cells on the surface of bone matrix (Figure 3). They secrete osteoid matrix composed of collagen type I as well as non-collagenous matrix proteins such as osteocalcin and alkaline phosphatase. The adhesion of mature osteoblasts to osteoid is mediated by cadherins[1, 2, 14, 15]. In a final step, unmineralized organic matrix incorporates hydroxyapatite crystals to form mineralized bone[16]. Aging osteoblasts can undergo apoptosis, they can differentiate into osteocytes or they become lining cells. The

latter cells are mostly quiescent and have a flat shape. They are found on bone surface presumably to prevent bone resorption[17].

3.3.2 Osteocytes

Osteocytes are cells that are incorporated into mineralized bone matrix. They are interconnected through a network of cannaliculi and they originate from MSCs through osteoblast differentiation (Figure 3). Osteocytes represent 90 to 95 % of bone cells, having a life span of up to 25 years[9]. A subpopulation of 5 to 20 % of osteoblasts differentiate first into osteoblastic osteocytes (Type I preosteocyte), then into osteoid-osteocytes (Type II preosteocyte), and finally into young and old osteocytes (Type II preosteocyte)[18, 19]. Whereas type I preosteocytes are only partially incorporated into the bone matrix, type II preosteocytes are totally encased in unmineralized bone matrix, *i.e.* osteoid. Furthermore, preosteocytes undergo morphological and ultrastructural changes. More specifically, this involves a reduction in size, a decrease in the number of cell organelles and an increase in nucleus-to-cytoplasm ratio (type III preosteocytes). After mineralization of osteoid, a reduction in endoplasmic reticula, Golgi apparatus and a subsequent reduction in collagen synthesis and secretion take place (mature or old osteocytes)[20]. Moreover, the expression of osteoblast marker genes like *Bglap*, *Bsp*, *Col1a1*, and *Alp* are either reduced or completely turned off. Instead, osteocytes express marker genes including phosphate-regulating neutral endopeptidase (*Phex*), dentin matrix protein 1 (*Dmp1*), matrix extracellular phosphoglycoprotein (*Mepe*), fibroblast growth factor 23 (*Fgf23)*, and sclerostin (*Sost*). Sost and Fgf23 are known as physiologically relevant molecules inhibiting bone formation and renal phosphate reabsorption, respectively[21, 22]. Regarding their function, osteocytes are involved in translating mechanical stimuli into biomechanical signals. The cells communicate via gap junctions, which are able to reach cortical and cancellous bone, as well as blood vessels within bone marrow[22].

3.3.3 Osteoclasts

Osteoclasts are large, multinucleated bone-resorbing cells originating from mononuclear cells of the hematopoietic lineage, similar to macrophages, lymphocytes and dendritic cells[23]. They become multinucleated by fusion of mononuclear monocytes[24]. Their differentiation is dependent on the influence of several factors including PU.1, macrophage-

colony stimulating factor (M-CSF) and receptor activator of NF-κB ligand (RANKL). PU.1 drives the expression of the *c-fms* gene, encoding the tyrosine kinase receptor of M-csf, and the receptor activator of NF-κB receptor (Rank)[25]. M-csf is secreted by osteoprogenitors and osteoblasts and binds to its receptor c-fms on mononuclear precursor cells, which stimulates osteoclast proliferation and survival[26, 27]. Furthermore, this cytokine stimulates the spreading, motility and cytoskeletal organization of a mature osteoclast[28]. Moreover, Rankl is released by osteoblasts, osteocytes, and stromal cells and binds to its receptor Rank on osteoclast precursors. This interaction induces the commitment and the terminal differentiation into mature osteoclasts[29, 30]. Another molecule controlling osteoclastogenesis is osteoprotegerin (Opg). Like M-csf, Opg is also expressed by osteoprogenitors and osteoblasts, but in contrast to M-csf, it competes with Rank as a decoy receptor for Rankl[31] (Figure 3).

Functionally, osteoclasts have the unique ability to resorb bone and are found on the surface of mineralized matrix. This resorption process requires high levels of energy expenditure, mediated through a high number of mitochondria inside the osteoclast. More specifically, proteolytic enzymes like tartrate-resistant acid phosphatase (TRAP), cathepsin K, and matrix metalloproteinase 9 (MMP9) are released to digest organic components of bone tissue, while the acidification of the resorption lacuna dissolves the inorganic components of the bone matrix[32].

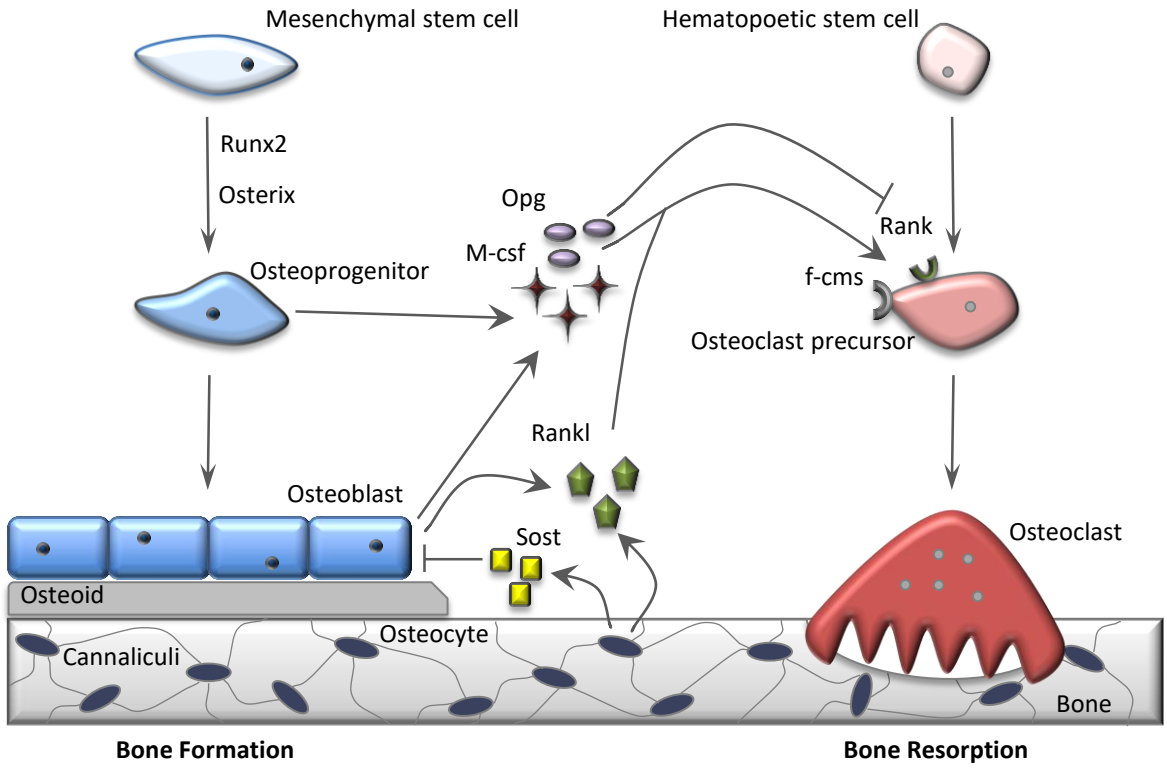

Figure 3: Schematic representation of bone remodeling cells. Mesenchymal stem cells differentiate into osteoprogenitors and finally into mature osteoblasts. These cells secrete unmineralized osteoid that later mineralizes to bone. Hematopoetic stem cells differentiate towards osteoclast precursors. These cells receive stimulating signals from molecules such as Rankl, M-csf that are secreted by cells of the osteoblast lineage, and further differentiate into mature osteoclasts. Additionally, osteoprogenitors and osteoblasts secrete Opg, which inhibits osteoclast precursors from differentiating into mature osteoclasts. Furthermore, osteocytes secrete Sost, thereby inhibiting bone formation.

3.4 Bone remodeling

Bones seem to be unchanging, but in fact, they are highly dynamic and constantly remodeled during development, growth, and also throughout adult life. To ensure life-long skeletal stability and health, a coordinated activity of antagonistically acting osteoblasts and osteoclasts is indispensable[1]. Bone remodeling occurs at so-called bone multicellular units (BMUs), including a cohort of cells such as osteoclasts, osteoblasts, osteocytes, lining cells, as well as capillary blood supply[33]. The process is initiated through different activating signals such as micro-fractures, mechanical loading, or different factors released in the bone microenvironment including insulin-like growth factor-1 (IGF-1), tumor necrosis factor-α (TNF-α), PTH and interleukin-6 (IL-6) (activation phase)[34]. These signals lead to the recruitment of osteoclast precursors, which further differentiate into mature osteoclasts to

resorb bone (resorption phase)[35]. After that, osteoclast activity arrests and cells go into apoptosis (reverse phase)[36]. In addition to their function in bone resorption, osteoclasts are also able to regulate bone formation. As the resorption takes place, different growth factors such as BMPs, FGFs, TGF-β and IGF-II are released from the bone matrix[37-39]. However, these resorption-derived factors are not essential for bone formation to occur, as patients with impaired osteoclast function are still able to form bone[40, 41].

Apart from releasing bone-forming factors from the bone matrix, osteoclasts are able to secrete molecules triggering bone formation, termed coupling factors. One reported osteoclast-secreted factor coupling bone resorption to bone formation is the lipid mediator sphingosine 1-phosphate (S1P). It is secreted by osteoclasts and binds to its receptor sphingosine 1-phosphate receptor 3 (S1pr3) on osteoblasts[42]. The release of S1P is inhibited by calcitonin[43]. An interaction of S1P and S1pr3 increases the production of Rankl in osteoblasts. Furthermore, it supports the migration in osteoblasts and osteoclast precursors and it promotes the survival of osteoblasts[44, 45]. Another potentially relevant coupling factor secreted by osteoclasts could be Wnt1, which was reported to be secreted after TGF-β-stimulation of osteoclasts, thus promoting bone formation[46].

When stimulated, osteoblasts start to form osteoid, which later mineralizes (formation phase). Besides its role in bone formation, osteoblasts additionally support osteoclast differentiation. To do so, they produce factors such as M-csf, Rankl and Opg. While M-csf and Rankl stimulate osteoclast differentiation, Opg competes with Rank as a decoy receptor of Rankl[31] (Figure 3). Furthermore, osteoblasts regulate the movement of osteoclast precursors towards the bone surface. For that, osteoblasts incorporate chemoattractants like osteocalcin and collagen type I into the bone matrix during bone formation. However, during bone resorption, these factors are released and attract osteoclast precursors towards the remodeling site to continue the process of resorption. Other factors, indirectly regulating osteoclastogenesis, are PTH, PTH-related protein (PTHrP), TNF-α, IL-1, and 1,25-$(OH)_2$ vitamin D_3 (VitD)[23, 47-50]. These soluble factors act on both osteoclasts and osteoblasts and increase the expression of Rankl, but also inhibit the expression of Opg[51].

Also osteocytes can regulate the activity and differentiation of osteoblasts and osteoclasts. However, there is evidence that osteocytes can both negatively and positively regulate

osteoblastogenesis. More specifically, the density of osteocytes is negatively correlated with bone formation, whereas other studies reported a severely reduction in bone formation due to *in vivo* target ablation of osteocytes[52]. Furthermore, mechanical loading activates the expression of *Sost*, encoding a secreted glycoprotein, which antagonizes canonical Wnt signaling and thereby inhibits bone formation[53, 54] (Figure 3). Additionally, also apoptotic osteocytes are able to regulate osteoclastogenesis by secreting pro-osteoclastogenic factors such as Rankl, TNF-α, IL-6 and IL-11.

3.5 Disorders of bone remodeling

Imbalanced bone remodeling may lead to different kinds of clinical diseases like osteopetrosis, osteosclerosis, osteogenesis imperfecta (OI), and osteoporosis, the latter representing the most prevalent bone remodeling disorder.

3.5.1 Osteopetrosis

Osteopetrosis or “marble bone disease” is a rare, heritable disorder characterized by an increased bone mass due to impaired osteoclast function. Despite increased bone mass, bones are weaker and patients suffer from skeletal fractures, as osteopetrotic bone matrix is composed of mineralized cartilage. Moreover, the expanding bone may lead to displacement of hematopoiesis from the bone to the spleen and liver, it can lead to narrow nerve foramina, leading to deafness, blindness, and facial palsy. Dependent on the mutations, an osteopetrotic phenotype can vary in severity ranging from incidental findings on radiographs to early onset life-threatening complications. Most patients of osteopetrosis receive a symptomatic treatment, whereas severe forms are treated with bone marrow transplantation, thereby replacing affected hematopoetic stem cells that further differentiate into osteoclasts[55].

3.5.2 Osteosclerosis

Osteosclerosis is also characterized by high bone mass. Patients of osteosclerosis suffer from bone overgrowth, leading to facial distortions and cranial nerve deficits, which can result in deafness, facial palsy, and the loss of vision or smell. In contrast to osteopetrosis, the osteosclerotic phenotype evolves due to increased osteoblast activity and decreased fracture risk. Sclerosteosis and Van Buchem Disease, both being caused by different loss-of-

function mutations affecting the *SOST* gene, are two well-known examples of osteosclerosis. Also gain-of-function mutations of the *low-density lipoprotein receptor-related protein 5* (*LRP5*) gene have been identified to cause osteosclerosis[56]. Both proteins were described in the context of Wnt signaling, where Sost was identified to bind to the Lrp5 receptor, thereby inhibiting the Wnt signaling pathway[53, 57].

3.5.3 Osteogenesis imperfecta

OI is a monogenetic disease affecting connective tissues. It is also known as "brittle bone disease" as typical clinical characteristics are high bone fragility together with a low bone mass, skeletal deformities, and a short stature. Other clinical manifestations are dentinogenesis imperfecta, blue-gray sclera, hearing impairment, muscle hypotonia, joint hypermobility, cardiovascular abnormalities, and restrictive pulmonary disease[58]. The prevalence of OI is estimated at about 1 in 15.000 to 20.000 births ranging from very mild forms to perinatal lethality with most cases having an autosomal dominant inheritance[59]. Due to a high genetic heterogeneity, an extensive phenotypic variability is found in patients of OI. About 90 % of OI forms are associated with mutations in *COL1A1* and *COL1A2*, encoding the α1 and α2 chains of collagen type I, respectively[60]. These mutations typically result in an altered structure or quantity of collagen type I. In addition, several genes required for bone mineralization, posttranslational modifications of collagen type I, and collagen processing such as *SERPINF1*, *CRTAP*, *LEPRE1*, *PPIB*, *SERPINH1*, *FKBP10*, *PLOD2*, and *BMP1* were identified to be mutated in different OI patients[58]. Genes like *IFITM5*, *SP7*, *TMEM38B*, *WNT1*, *CREB3L1*, *SPARC*, and *MBTPS2* were further identified as genes causing OI without being directly related to collagen processing. A complete genetic classification of OI with related genes and clinical characteristics is shown in Table1.

Table1: Genetic classification of OI modified from[61]. AD: autosomal dominant; AR: autosomal recessive; XR: X-linked recessive

Mutated gene	Encoded protein	OI type	Inheri-tance	Clinical characteristics
Impairment of collagen synthesis and structure				
COL1A1, COL1A2	Collagen α1(I) (COL1A1) or α2(I) (COL1A2)	I, II, III or IV	AD	Classic phenotype
Compromized bone mineralization				
SERPINF1	Pigment epithelium-derived factor (PEDF)	VI	AR	Moderate-to-severe skeletal deformity, the presence of osteoid, fish-scale appearance of lamellar bone pattern and childhood onset
Abnormal collagen post-translational modification				
CRTAP	Cartilage-associated protein (CRTAP)	VII	AR	Severe rhizomelia with white sclerae
LEPRE1	Prolyl 3-hydroxylase 1 (P3H1)	VIII	AR	
PPIB	Peptidyl-prolyl *cis–trans*isomerase B (PPIase B)	IX	AR	Severe bone deformity with grey sclerae
Compromised collagen processing and crosslinking				
SERPINH1	Serpin H1 (also known as HSP47)	X	AR	Severe skeletal deformity, blue sclerae, dentinogenesis imperfecta, skin abnormalities and inguinal hernia
FKBP10	65 kDa FK506-binding protein (FKBP65)	XI	AR	Mild-to-severe skeletal deformity, normal-to-grey sclerae and congenital contractures
PLOD2	Lysyl hydroxylase 2 (LH2)	No type	AR	Moderate-to-severe skeletal deformities and progressive joint contractures
BMP1	Bone morphogenetic protein 1 (BMP1)	XII	AR	Mild-to-severe skeletal deformity and umbilical hernia
Altered osteoblast differentiation and function				
IFITM5	Bone-restricted interferon-induced transmembrane protein-like protein (BRIL; also known as IFM5)	V	AD	Normal-to-severe skeletal deformity, intraosseous membrane ossifications, radiodense band and radial head dislocation, normal-to-blue sclerae and sometimes hearing loss
SP7	Transcription factor SP7 (also known as osterix)	XIII	AR	Severe skeletal deformity with delayed tooth eruption and facial hypoplasia
TMEM38B	Trimeric intracellular cation channel type B (TRIC-B; also known as TM38B)	XIV	AR	Severe bone deformity with normal-to-blue sclerae
WNT1	Proto-oncogene Wnt-1 (WNT1)	XV	AR, AD	Severe skeletal abnormalities, white sclerae and possible neurological defects
CREB3L1	Old astrocyte specifically induced substance (OASIS; also known as CR3L1)	XVI	AR	Severe bone deformities
SPARC	SPARC (also known as osteonectin)	XVII	AR	Progressive severe bone fragility
MBTPS2	Membrane-bound transcription factor site-2 protease (S2P)	XVIII	XR	Moderate-to-severe skeletal deformity, light blue sclerae, scoliosis and pectoral deformities

3.5.4 Osteoporosis

Among all disorders of bone remodeling, osteoporosis represents the highest prevalence affecting 200 million people worldwide[62]. It is characterized by a decrease in bone mineral density leading to an enhanced risk of skeletal fractures without experiencing a significant trauma. On a cellular basis, it is caused by a relative increase in bone resorption over bone formation resulting in an overall decreased bone mass. Underlying mechanisms causing osteoporosis can be highly variable and interfere at different stages of the complete bone remodeling process.

In humans, the severity of osteoporosis is clinically evaluated by measuring the bone mineral density (BMD) by dual-energy X-ray absorptiometry (DXA), thereby determining the T-score, a value that compares the measured BMD to a healthy 30-year old adult. Whereas T-scores between -1 and +1 are considered as normal, a T-score lower than -1 indicates osteopenia, and a T-score below -2.5 is diagnosed as osteoporosis[63].

Currently approved treatment options for osteoporosis are either anti-resorptive drugs (bisphosphonates), a RANKL inhibitor (Denosumab), or osteoanabolic agents (PTH analogues like Teriparatide)[64-67].

3.5.5 Pathways affecting bone remodeling

Several signaling pathways have been described to regulate bone remodeling. Among all of them, the Notch and the Wnt signaling pathway have been analyzed in greater detail in this thesis.

3.5.5.1 Notch signaling in bone metabolism

Notch signaling was long time known for its role in neuronal development where it controls lateral inhibition. This is an intercellular communication process, which allows the differentiation of single cells, whereas the neighboring cells are inhibited from adopting the same fate[68]. In vertebrates, 4 different Notch receptors were identified (Notch1 to 4) that can be activated by different ligands such as Jagged1, Jagged2, Delta-like (Dll) 1, Dll3, or Dll4[69]. Activation further leads to 2 proteolytic cleavage events on the receptor, which are mediated by ADAM metalloproteases and the γ-secretase complex. The latter proteolytic complex leads to the release of the Notch intracellular domain (NICD). This domain further

translocates into the nucleus to activate the transcription of target genes including members of the *Hey* and *Hes* family[70, 71]. Notch signaling is negatively regulated by the C-terminal proline-, glutamine-, serine-, threonine-rich domain (PEST-domain), which is required for proteasomal degradation of the NICD[72, 73].

The importance of Notch signaling as a critical regulator of bone metabolism was established through the analyses of several mouse models in the past years. More specifically, mouse models lacking different components of the signaling pathway displayed defects in the axial skeleton[74-76]. Further in depth studies of Notch function in the osteoblast lineage revealed that conditional inactivation of components of the γ–secretase complex in limb mesenchymal cells resulted in excessive trabecular bone formation in the hindlimbs together with a loss of osteoprogenitors. Similarly, a mouse model with *Notch1* and *Notch2* deletion in limb mesenchymal cells exhibited initial high bone mass, which turned into severe bone loss with age[77]. Furthermore, overexpression of the NICD in early osteoblastic cells resulted in a low bone mass and impaired growth[78]. Overexpression of the NICD of Notch1 at a later stage of osteoblast differentiation, however, revealed excessive proliferation of osteoprogenitors combined with inhibition of osteoprogenitors to differentiate into mature osteoblasts[77, 79]. Together, these observations show that Notch signaling positively influences the maintenance of osteoprogenitors and additionally negatively affects the differentiation of osteoprogenitors to mature osteoblasts. In humans, identified mutations in genes of the Notch signaling pathway were also associated with different skeletal disorders such as Spondylocostal dysostosis and Alagille syndrome[80-82].

The recent identification of *NOTCH2* mutations in individuals with HCS confirmed its role in human bone metabolism. HCS is a rare skeletal disorder characterized by osteoporosis, acro-osteolyses, short stature, coarse facies and renal cysts[83-85]. All identified *NOTCH2* mutations causing HCS were reported to result in a truncation of the receptor lacking the PEST-domain, which is further predicted to result in a prolonged NOTCH2 signal. Additionally, a HCS patient was analyzed at the Department for Osteology and Biomechanics displaying severe osteoporosis with a T-score below -5, together with increased bone formation and bone resorption markers like bone alkaline phosphatase (Bone AP) and the deoxypyridinoline/creatinine ratio (Dpd/Crea) (Figure 4).

A **B** **C**

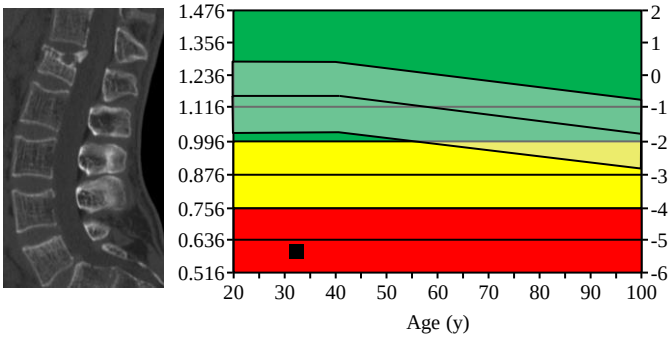

Parameter	HCS	Ref. range
Calcium [mM]	2.27	2.13 – 2.63
Phosphorus [mM]	0.93	0.77 – 1.50
1.25-OH-VitD_3 [µg/l]	31.82	> 30
PTH [pg/ml]	31.08	17 – 84
Bone AP [µg/ml]	35.0	5.5 – 22.9
Dpd/Crea [nmol/mmol]	8.0	2.0 - 5.0

Figure 4: Characterization of a 32-years old male HCS patient. (A) CT image of the patient´s lumbar spine (sagittal view). **(B)** DXA determination of the T-Score in L2 to L4 vertebral bodies showing a T-score below -5, indicating severe osteoporosis. **(C)** Serum analysis of bone metabolic parameters. Bone AP: Bone Alkaline Phosphatase; DPD/Crea: deoxypyridinoline/creatinine ratio. Values outside the reference range appear red.

Motivated by the findings obtained in the course of my master thesis in 2015, where an osteoblast-specific inactivation of *Notch2* was found to cause high bone formation at specific sites of the appendicular skeleton[86], a mouse model carrying the 6272delT mutation in *Notch2* was generated and initially characterized by Timur Yorgan at the Department for Osteology and Biomechanics (UKE). Further analyses including the uncovering of molecular mechanisms were performed in the course of this thesis and published in 2017 in the Journal for Bone and Mineral Research under the title “High Bone Turnover in Mice Carrying a Pathogenic Notch2 Mutation Causing Hajdu-Cheney Syndrome”[87].

3.5.5.2 Wnt signaling in bone metabolism

Wnt signaling is an evolutionary conserved signaling pathway that is required for cell fate determination, proliferation, polarity and cell death, both during embryonic development and also throughout adult life[88]. WNT proteins belong to a family of 19 different secreted glycoproteins that are required for the activation of their cell-surface receptors. Activation of the pathway occurs through the binding of a WNT ligand to a Frizzled receptor and an additional binding to a LRP5 or 6 co-receptor[89, 90]. The intracellular transmission of the Wnt signal inhibits the proteolysis of β-catenin[91, 92]. An accumulation of β-catenin in the cytoplasm enables its translocation into the nucleus where it activates the transcription of target genes[93].

The high importance of WNT signaling in bone metabolism emerged with the identification of mutations affecting different components of the pathway, causing alterations in skeletal development. More specifically, a loss-of-function mutation in LRP5 was found to result in osteoporosis-pseudoglioma syndrome (OPPG), characterized by severely reduced bone mass[94], whereas activating mutations of LRP5 were described to result in high bone mass (HBM), caused by an altered binding site for WNT antagonists like dickkopf 1 (DKK1) and Sost[95-98]. To date, several transgenic mouse models have been created to examine the role of Wnt signaling in bone metabolism. Analyses of these mouse models suggested that Wnt signaling was involved in the regulation of mature osteoblast activity[99], in osteoclast differentiation by influencing the production of Opg[14], and by enhancing the expression of Rank on osteoclast precursor cells[100, 101]. The pathway was also found to influence the responsiveness of osteoblasts to osteoanabolic PTH(1-34)[102]. Furthermore, specific inactivation of β-catenin in early osteoblasts caused a striking osteopenic phenotype due to an increased number of osteoclasts[14, 103, 104].

What was still unknown is which of the 19 WNT ligands is physiologically involved in controlling bone homeostasis. However, the identification of *WNT1* mutations in individuals with early-onset osteoporosis (EOOP) and OI type XV highlighted the impact of this ligand in bone homeostasis[105-108]. Mutations in *Wnt1* were already described in a swaying mouse model (*Wnt1*$^{sw/sw}$), carrying a spontaneous mutation in *Wnt1*. These mice were previously only analyzed for their brain phenotype, *i.e*. a defect of cerebellar development. In 2014 however, it was reported that they additionally develop an osteoporotic phenotype associated with spontaneous fractures[109]. More recently, osteocyte-specific inactivation of *Wnt1* was reported to cause a similar phenotype to the swaying mice[110]. Consistently, investigations of a mouse model overexpressing Wnt1 revealed excessive bone formation, underscoring the importance of Wnt1 as an osteoanabolic molecule (Luther *et al.*, 2018, submitted).

To further analyze the role of Wnt1 in bone formation, a mouse model carrying a pathogenic 529G>T mutation in *Wnt1*, identified in patients with OI type XV, was generated and characterized in the course of this thesis.

4 Aims of the work

Among all skeletal disorders, osteoporosis represents the highest prevalence with the most socio-economic impact. Because the underlying mechanisms can be highly variable, it is important to focus on genetic diseases associated with osteoporosis and to uncover the underlying cellular and molecular mechanisms. By the identification of *NOTCH2* mutations in patients with HCS, which is primarily characterized by osteoporosis and acro-osteolyses, the importance of Notch signaling in bone metabolism gained significance. Therefore, the main aim of this thesis was the elucidation of underlying mechanisms causing the osteoporotic phenotype in HCS patients. To do so, a mouse model carrying a pathogenic *Notch2* mutation, identified to cause HCS in humans, was generated. These mice were phenotypically characterized by performing micro-computed tomography (µCT) and histomorphometric analyses. Additionally, cell culture experiments were performed to examine molecular mechanisms. In the context of this study, also the Wnt signaling pathway was analyzed regarding its role in bone metabolism. Therefore, a second mouse model carrying a pathogenic mutation in *Wnt1*, which was associated with OI type XV in humans, was generated and analyzed by µCT-, histomorphometric-, cell culture- and mechanical analyses.

5 Results

5.1 Notch2^{HCS} mice

5.1.1 Initial characterization of *Notch2*$^{+/HCS}$ mice

After generating *Notch2*^{HCS} mice by homologous recombination, *Notch2*$^{+/+}$, *Notch2*$^{+/HCS}$ and *Notch2*$^{HCS/HCS}$ mice were analyzed for the presence or absence of the mutation by Sanger sequencing. The presence of the *Notch2* mutation could be confirmed in *Notch2*$^{+/HCS}$ and *Notch2*$^{HCS/HCS}$, resulting in a premature stop codon eight nucleotides further downstream (Figure 5A). To further confirm the truncation of the Notch2 protein in mice carrying the HCS mutation, a western blot with an antibody against the truncated PEST-domain on protein extracts from cultured calvarial osteoblasts isolated from *Notch2*$^{+/+}$, *Notch2*$^{+/HCS}$ and *Notch2*$^{HCS/HCS}$ mice was performed. The results of the western blot showed a clear reduction of PEST-domain expression in heterozygous mice and no expression in homozygous mice compared to control samples. The expression of β-Actin was used as a general loading control (Figure 5B). Furthermore, *Notch2*$^{+/+}$, *Notch2*$^{+/HCS}$, and *Notch2*$^{HCS/HCS}$ offspring were born at the expected Mendelian ratio. However, a reduced viability of homozygous *Notch2*$^{HCS/HCS}$ mice, with 60 % of them not surviving the first 5 weeks of age, could be observed (Figure 5C).

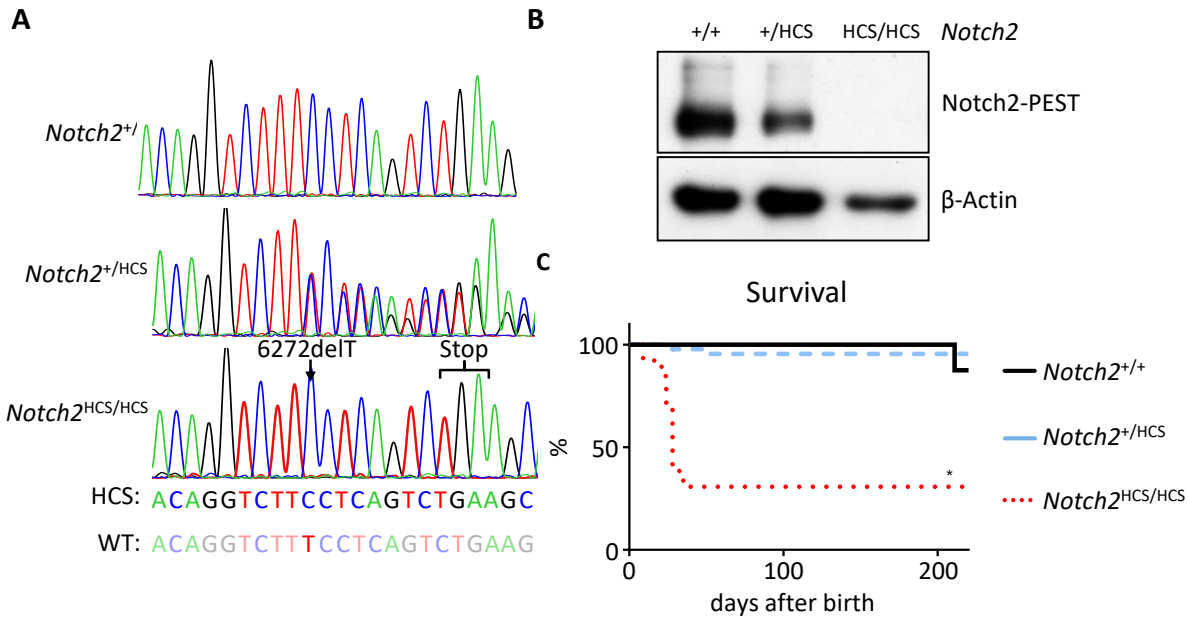

Figure 5: Generation of a mouse model lacking the PEST-domain of Notch2. (A) Sanger sequencing results of *Notch2*$^{+/+}$, *Notch2*$^{+/HCS}$, and *Notch2*$^{HCS/HCS}$ mice. Black arrow: introduced frameshift mutation resulting in premature stop codon. **(B)** Western blot with an antibody specific for the Notch2 PEST-domain of protein lysates from calvarial osteoblasts derived from *Notch2*$^{+/+}$, *Notch2*$^{+/HCS}$ and *Notch2*$^{HCS/HCS}$ mice at day 5 of osteogenic differentiation. β-Actin was used as a loading control. **(C)** Survival curve of *Notch2*$^{+/+}$, *Notch2*$^{+/HCS}$, and *Notch2*$^{HCS/HCS}$ mice. Data were analyzed by Mantel-Cox log rank test. n≥13 mice per group *p<0.05 vs. wild-type littermates.

5.1.2 Characterization of *Notch2*$^{+/HCS}$ mice with respect to skeletal pathologies seen in HCS patients

To study if *Notch2*$^{+/HCS}$ mice display pathologies typically associated with HCS in humans, the distal phalanges of *Notch2*$^{+/+}$ and *Notch2*$^{+/HCS}$ mice were examined pertaining to acro-osteolyses by contact X-ray and the skulls of both genotypes were analyzed by µCT for characteristic deformities seen in HCS patients. All parameters were analyzed at 12, 24, and 52 weeks of age. The analyses revealed no presence of acro-osteolyses in *Notch2*$^{+/HCS}$ mice at all ages analyzed (Figure 6).

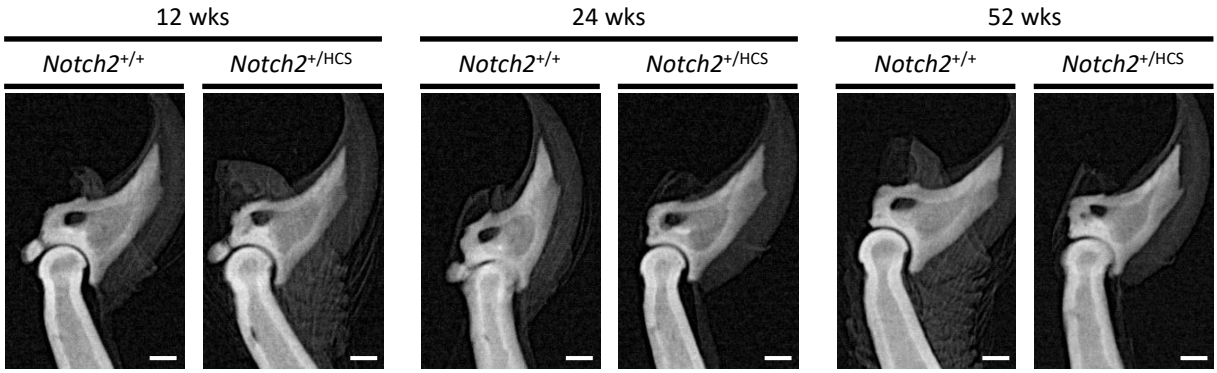

Figure 6: Analysis on acro-osteolyses. Representative contact X-rays of the distal phalanges of female *Notch2*$^{+/+}$ and *Notch2*$^{+/HCS}$ mice at 12, 24, and 52 weeks (wks) of age.

When analyzing the skull, *Notch2*$^{+/HCS}$ mice displayed subtle changes in skull morphology. More specifically, the skull and nasal lengths were significantly decreased in *Notch2*$^{+/HCS}$ mice compared to controls at 24 weeks of age. The skull width was decreased in *Notch2*$^{+/HCS}$ mice at 24 and 52 weeks of age. Importantly, an increase in calvarial porosity observed in *Notch2*$^{+/HCS}$ animals at all ages analyzed indicated excessive bone resorption (Figure 7).

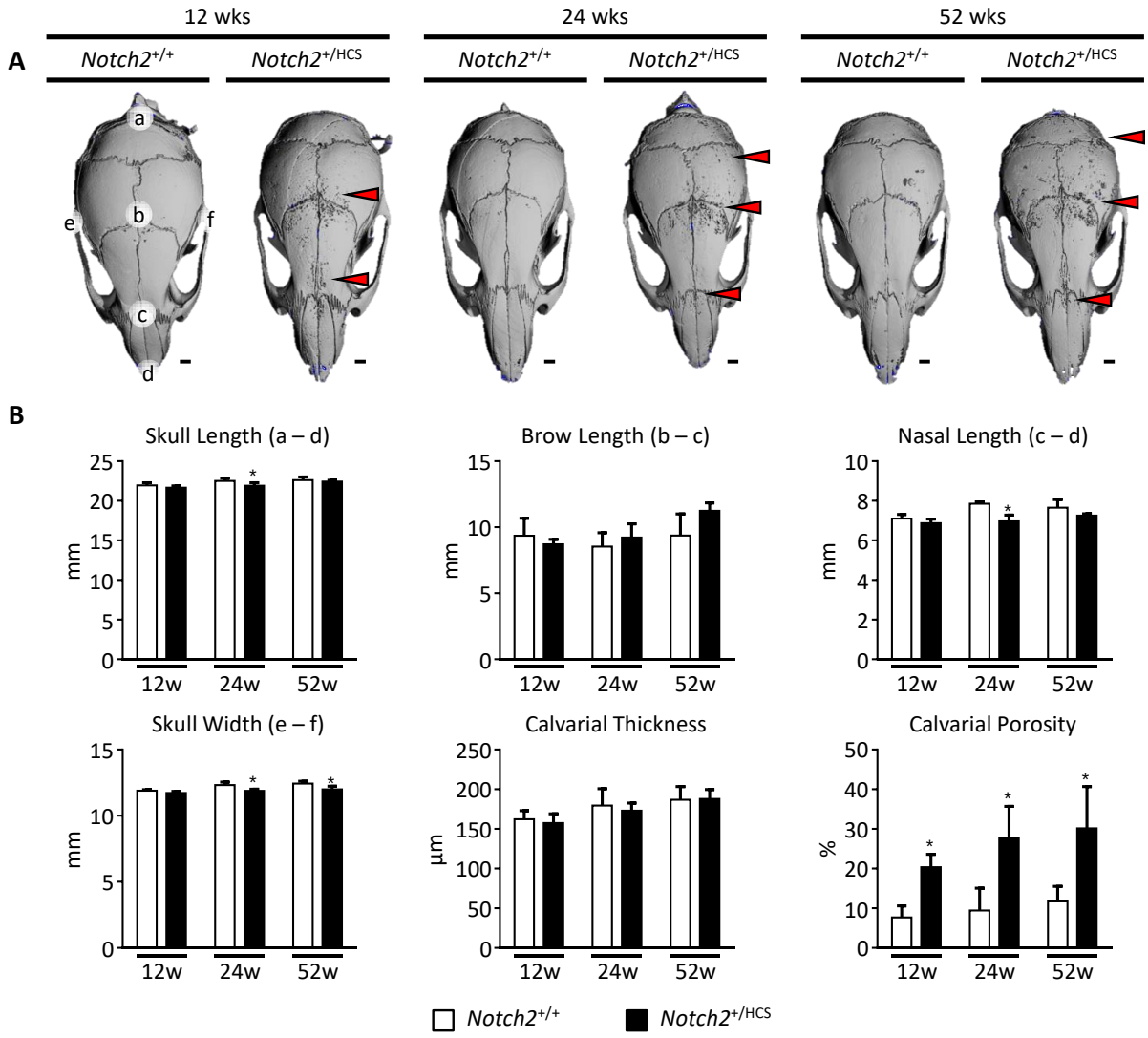

Figure 7: Analysis of facial deformities. (A) Representative µCT images of skulls from female *Notch2*$^{+/+}$ and *Notch2*$^{+/HCS}$ mice at 12, 24, and 52 weeks (wks) of age. The letters on the first skull mark the morphological positions used for quantitative analysis. Scale bar=1 mm. Red arrows indicate calvarial porosity. **(B)** Quantification of morphological parameters analyzed by µCT. Letters in brackets refer to the positions marked in A. w: weeks. Data were analyzed by two-tailed Student´s t test. n≥5 mice per group *p<0.05 vs. age-matched wild-type littermates.

5.1.3 Structural bone phenotype of *Notch2*$^{+/HCS}$ mice

As HCS patients display an osteoporotic bone phenotype together with a high bone turnover, *Notch2*$^{+/HCS}$ mice were analyzed with regard to these pathologies. Starting with the length of several bones, such as femur, tibia and L4 vertebral body, subtle but significant reductions could be observed in *Notch2*$^{+/HCS}$ mice compared to *Notch2*$^{+/+}$ controls, especially at 24 weeks of age (Figure 8).

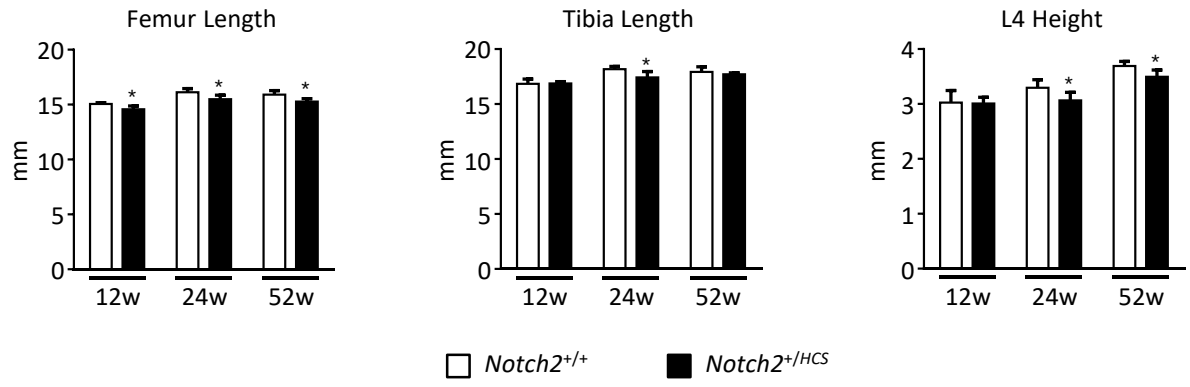

Figure 8: Structural length and height analysis of bones. Femur and tibia lengths and L4 vertebral body height of female *Notch2*$^{+/+}$ and *Notch2*$^{+/HCS}$ mice at 12, 24, and 52 weeks (w) of age. Data were analyzed by two-tailed Student´s t test. n≥5 mice per group *p<0.05 vs. age-matched wild-type littermates.

Furthermore, µCT analysis of the femora of 12, 24, and 52 weeks old *Notch2*$^{+/+}$ and *Notch2*$^{+/HCS}$ mice were performed to analyze the bone structure in more detail. The analyses revealed a reduction of trabecular bone volume (BV/TV) in the distal metaphysis of the femur in *Notch2*$^{+/HCS}$ mice compared to wild-type littermates at 12, 24, and 52 weeks of age. The cortical thickness (Ct.Th) was also decreased, reaching significance at 52 weeks of age. Additionally, the midshaft diameter (Ms.D) was decreased in *Notch2*$^{+/HCS}$ mice compared to controls at all ages analyzed (Figure 9).

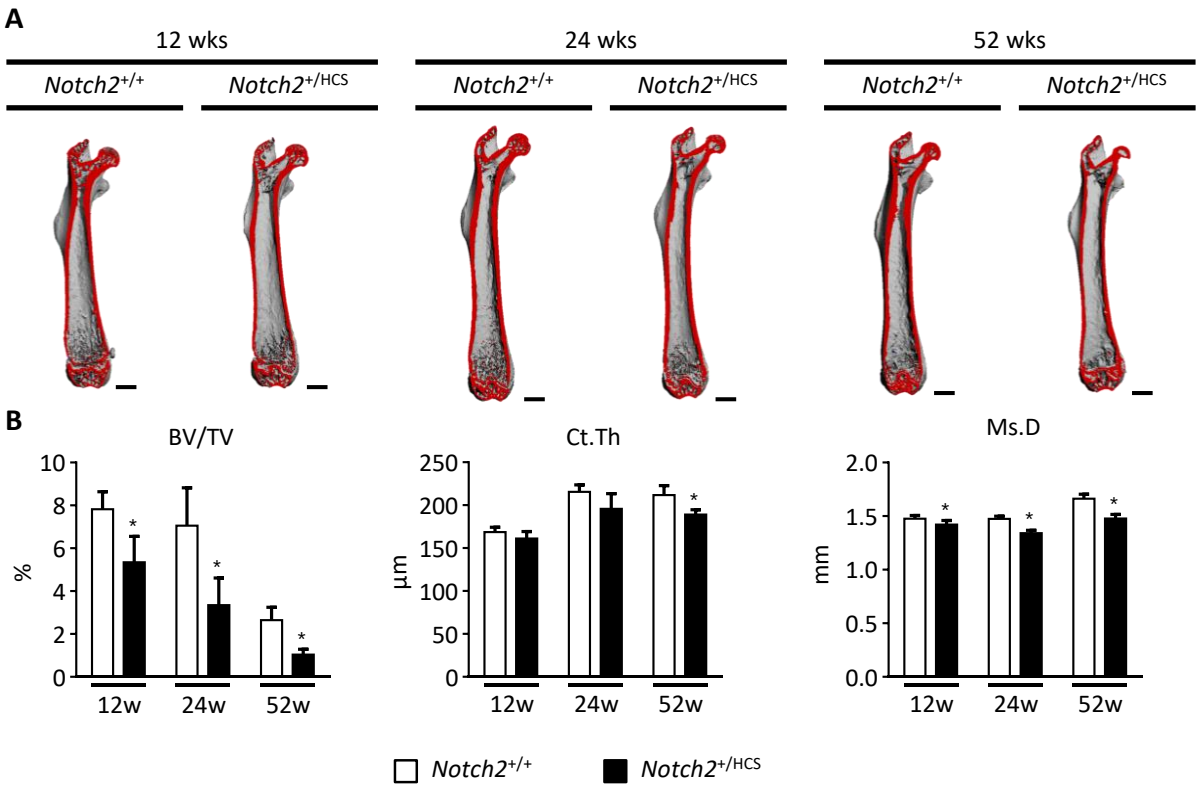

Figure 9: *Notch2*$^{+/HCS}$ mice display osteopenia in femora. (A) Representative µCT images of femora from female *Notch2*$^{+/+}$ and *Notch2*$^{+/HCS}$ mice at 12, 24, and 52 weeks (wks) of age. The virtual cutplane appears in red. Scale bar=1 mm. **(B)** Quantification of BV/TV, Ct.Th and Ms.D of µCT analyses from A. w: weeks. Data were analyzed by two-tailed Student´s t test. n≥5 mice per group *p<0.05 vs. age-matched wild-type littermates.

For the analysis of vertebral bodies, undecalcified histology of spine sections was performed. Here, the lumbar vertebral bodies L3 and L4 were analyzed for structural histomorphometry. The investigations revealed a significant decrease in trabecular bone volume compared to wild-type littermates in all age groups analyzed. This was caused by both trabecular thinning (Tb.Th) and a reduction in trabecular numbers (Tb.N) in *Notch2*$^{+/HCS}$ mice (Figure 10).

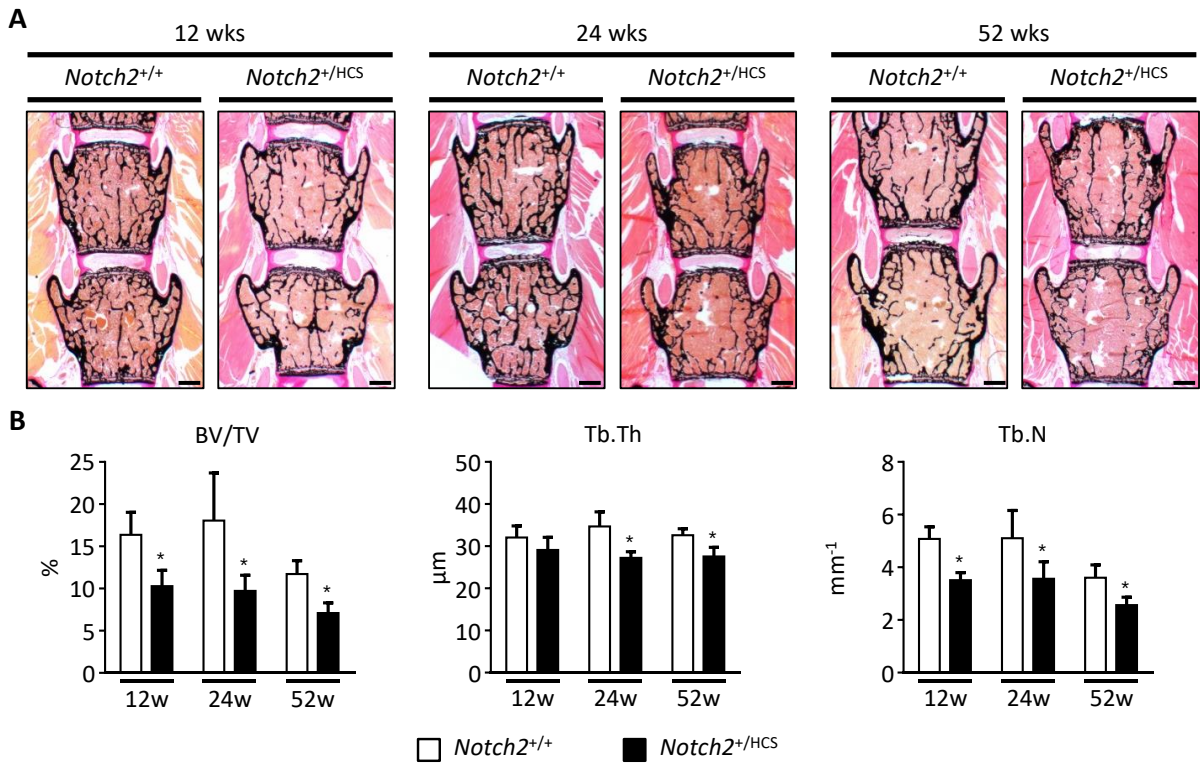

Figure 10: *Notch2*$^{+/HCS}$ mice display osteopenia in the spine. (A) Representative undecalcified spine sections from female *Notch2*$^{+/+}$ and *Notch2*$^{+/HCS}$ mice at 12, 24, and 52 weeks (wks) of age stained with von Kossa/van Giesson. Scale bar=500 µm **(B)** Quantification of trabecular parameters in spine sections from A. w: weeks. Data were analyzed by two-tailed Student´s t test. n≥5 mice per group *p<0.05 vs. age-matched wild-type littermates.

Taken together, these results demonstrate that *Notch2*$^{+/HCS}$ mice serve as an excellent model for the osteoporotic phenotype of human HCS, although acro-osteolyses were not observed, unlike it is the case in patients.

5.1.4 Cellular bone phenotype of *Notch2*$^{+/HCS}$ mice

To study the underlying cellular mechanism causing the reduction in bone mass in *Notch2*$^{+/HCS}$ mice, cellular histomorphometry was applied. Here, the number of bone-resorbing osteoclasts per bone perimeter (N.Oc/B.Pm), the osteoclast surface per bone surface (Oc.S/BS), as well as the number of bone-forming osteoblasts per bone perimeter (N.Ob/B.Pm), and the number of osteocytes per bone area (N.Ot/B.Ar) was analyzed in *Notch2*$^{+/+}$ and *Notch2*$^{+/HCS}$ mice at 12, 24, and 52 weeks of age.

The results of cellular histomorphometry revealed an increase in osteoclast indices as well as an increase in osteoclast surface in *Notch2*$^{+/HCS}$ mice compared to wild-type littermate controls with significance at 24 weeks of age (Figure 11A). Likewise, osteoblast indices were elevated compared to controls especially at 24 and 52 weeks of age (Figure 11B), together indicating a high bone turnover situation similar to the pathology found in human HCS patients. The reason for quantifying the number of osteocytes was the initial assumption that the process of osteocyte differentiation is reminiscent of lateral inhibition. As the indices of osteocytes did not differ between *Notch2*$^{+/+}$ and *Notch2*$^{+/HCS}$ mice, this assumption could be neglected (Figure 11C).

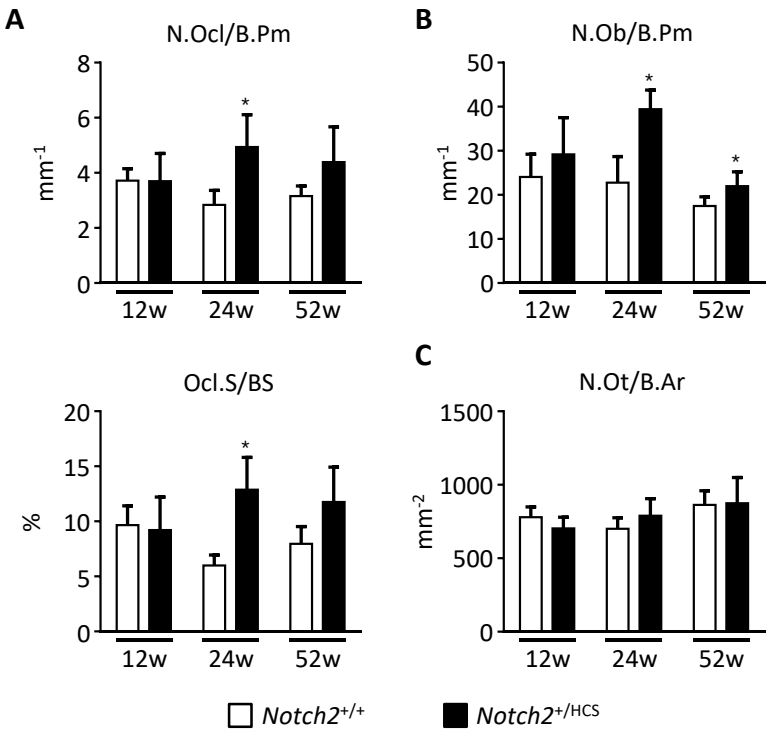

Figure 11: *Notch2*$^{+/HCS}$ mice display a high bone turnover. (A) Quantification of histomorphometric osteoclast indices in female *Notch2*$^{+/+}$ and *Notch2*$^{+/HCS}$ mice at 12, 24, and 52 weeks (w) of age. **(B)** Quantification of the number of osteoblasts in female *Notch2*$^{+/+}$ and *Notch2*$^{+/HCS}$ mice at 12, 24, and 52 weeks (w) of age. **(C)** Quantification of the number of osteocytes in female *Notch2*$^{+/+}$ and *Notch2*$^{+/HCS}$ mice at 12, 24, and 52 weeks (w) of age. Data were analyzed by two-tailed Student´s t test. n≥5 mice per group *p<0.05 vs. age-matched wild-type littermates.

To quantify the osteoclast resorbing activity *in vivo*, serum crosslaps (CTx) levels were measured by ELISA. Molecular fragments, including C-terminal telopeptides that are secreted during collagen degradation, were quantified, indicating an increased rate of bone resorption, especially at 52 weeks of age, which is in agreement with increased osteoclast indices (Figure 12A). Referring to the reduced bone mass observed in *Notch2*$^{+/HCS}$ mice, increased CTx levels further underline the increase in bone resorption. The bone formation rate per bone surface (BFR/BS) was analyzed by dynamic histomorphometry in *Notch2*$^{+/+}$ and *Notch2*$^{+/HCS}$ mice at 12, 24, and 52 weeks of age. At all ages analyzed, the bone formation

rate was significantly increased compared to wild-type littermate controls, underscoring the high bone turnover situation (Figure 12B).

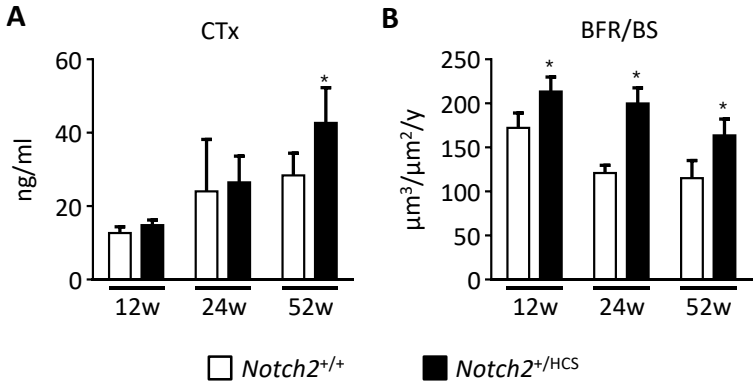

Figure 12: High bone turnover in *Notch2*$^{+/HCS}$ mice. (A) Serum CTx concentrations in female *Notch2*$^{+/+}$ and *Notch2*$^{+/HCS}$ mice at 12, 24, and 52 weeks (w) of age. **(B)** Quantification of the bone formation rate in the vertebral bodies of female *Notch2*$^{+/+}$ and *Notch2*$^{+/HCS}$ mice at 12, 24, and 52 weeks of age. Data were analyzed by two-tailed Student´s t test. n≥5 mice per group *p<0.05 vs. age-matched wild-type littermates.

5.1.5 Analysis of *Notch2*$^{+/HCS}$ osteoclasts

To analyze if *Notch2*$^{+/HCS}$ mice display cell-autonomous changes of bone remodeling cells, *ex vivo* cultures of osteoclasts and osteoblasts were examined. First, by culturing bone marrow cells from *Notch2*$^{+/+}$ and *Notch2*$^{+/HCS}$ mice in the presence of VitD (starting at day of plating), with or without further addition of Rankl and M-csf (starting at day 5 after plating), the intrinsically differentiation capacity of pre-osteoclasts was analyzed. When counting the number of osteoclasts from day 6 until day 10 after plating, no differences were observed between *Notch2*$^{+/+}$ and *Notch2*$^{+/HCS}$ cultures in terms of osteoclastogenesis (Figure 13A). To analyze the activity of osteoclasts from *Notch2*$^{+/+}$ and *Notch2*$^{+/HCS}$ cultures, a dentin resorption assay was performed. When quantifying the resorbed area (stained in dark purple), no significant changes between *Notch2*$^{+/+}$ and *Notch2*$^{+/HCS}$ osteoclasts were observed (Figure 13B). In summary, both experiments indicated no cell-autonomous changes in osteoclastogenesis.

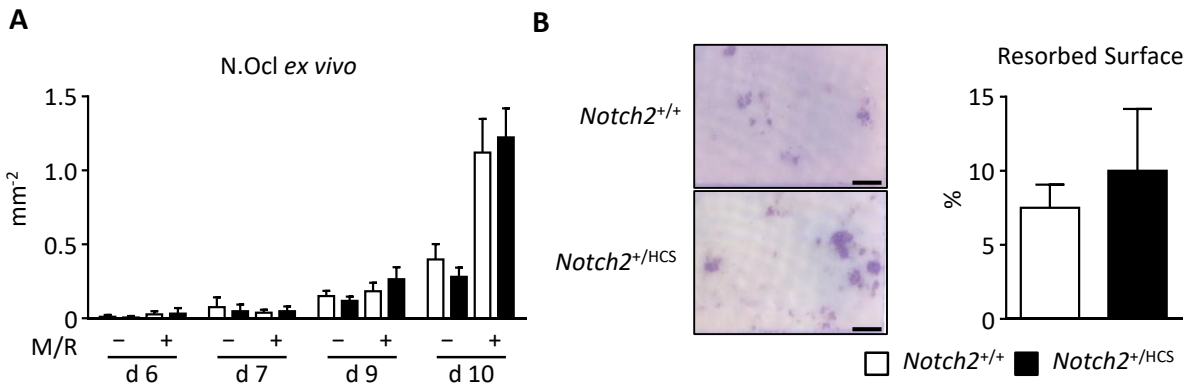

Figure 13: No cell-autonomous defect in *Notch2*$^{+/HCS}$ osteoclasts. (A) Quantification of the number of osteoclasts present in *ex vivo* bone marrow cultures derived from *Notch2*$^{+/+}$ and *Notch2*$^{+/HCS}$ mice at day (d) 6, 7, 9, and 10 of differentiation with (+) or without (-) M-csf and Rankl (M/R). Data were analyzed by two-tailed Student´s t test. n=3 samples per group. **(B)** Representative images and quantification of dentin resorption assay after 10 days of *ex vivo* culture with osteoclasts derived from *Notch2*$^{+/+}$ or *Notch2*$^{+/HCS}$ mice. Scale bar=1 mm. Data were analyzed by two-tailed Student´s t test. n=3 samples per group.

Another method to study cell-autonomous modifications in osteoclasts *in vivo* is bone marrow transplantation (BMT), where hematopoetic stem cells from a donor mouse are transplanted into an irradiated recipient mouse. In this thesis, bone marrow from *Notch2*$^{+/+}$ mice was transplanted into irradiated *Notch2*$^{+/HCS}$ mice and into *Notch*$^{+/+}$ mice as a control at the age of 8 weeks. These animals were sacrificed and histomorphometrically analyzed at the age of 24 weeks.

BMT led to an overall loss of trabecular bone mass in both genotypes (Figure 14B). Most importantly, however, a further increase in osteoclast indices in *Notch2*$^{+/HCS}$ and also *Notch2*$^{+/+}$ mice was observed (Figure 14C). Furthermore, the bone formation rate significantly increased in both *Notch2*$^{+/+}$ and *Notch2*$^{+/HCS}$ treated mice compared to untreated controls (Figure 14D). All BMT findings together did not provide a definite conclusion as osteoclast indices were further increased in both *Notch2*$^{+/HCS}$ and also *Notch2*$^{+/+}$ mice.

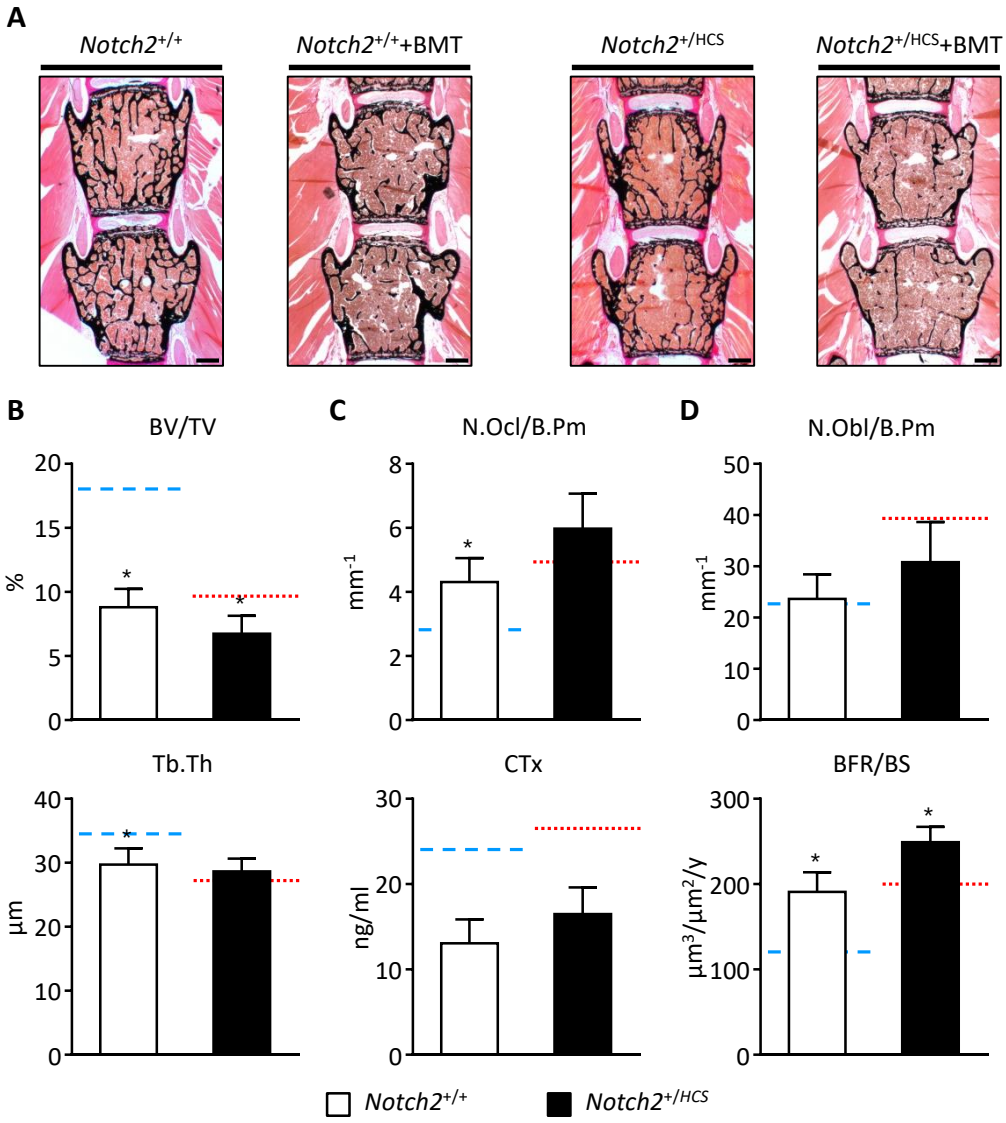

Figure 14: No correction of osteopenic phenotype after BMT. (A) Representative images of von Kossa/van Giesson-stained undecalcified spine sections from 24 weeks old *Notch2*$^{+/+}$ and *Notch2*$^{+/HCS}$ mice that have (BMT) or have not received BMT at the age of 8 weeks. Scale bar=500 µm. **(B)** Quantification of structural parameters in vertebral bodies from bone marrow transplanted *Notch2*$^{+/+}$ and *Notch2*$^{+/HCS}$ mice from A. Data were analyzed by two-tailed Student´s t test. n≥5 mice per group *p<0.05 vs. age-matched wild-type littermates. **(C)** Quantification of osteoclast indices in vertebral bodies and serum CTx levels of bone marrow transplanted *Notch2*$^{+/+}$ and *Notch2*$^{+/HCS}$ mice from A. Data were analyzed by two-tailed Student´s t test. n≥5 mice per group *p<0.05 vs. age-matched wild-type littermates. **(D)** Quantification of osteoblast indices and BFR/BS in vertebral bodies of bone marrow transplanted *Notch2*$^{+/+}$ and *Notch2*$^{+/HCS}$ mice from A. Dotted lines represent the mean value of each parameter of untreated mice of the corresponding genotype (blue: *Notch2*$^{+/+}$; red: *Notch2*$^{+/HCS}$). Data were analyzed by two-tailed Student´s t test. n≥5 mice per group *p<0.05 vs. untreated controls of the same genotype.

However, when analyzing the calvariae of the BMT-treated mice by µCT, the elevated calvarial porosity found in untreated *Notch2*$^{+/HCS}$ mice was not corrected by BMT (Figure 15B), indicating that increased osteoclastogenesis found in untreated *Notch2*$^{+/HCS}$ mice is not caused by a cell-autonomous gain-of-function.

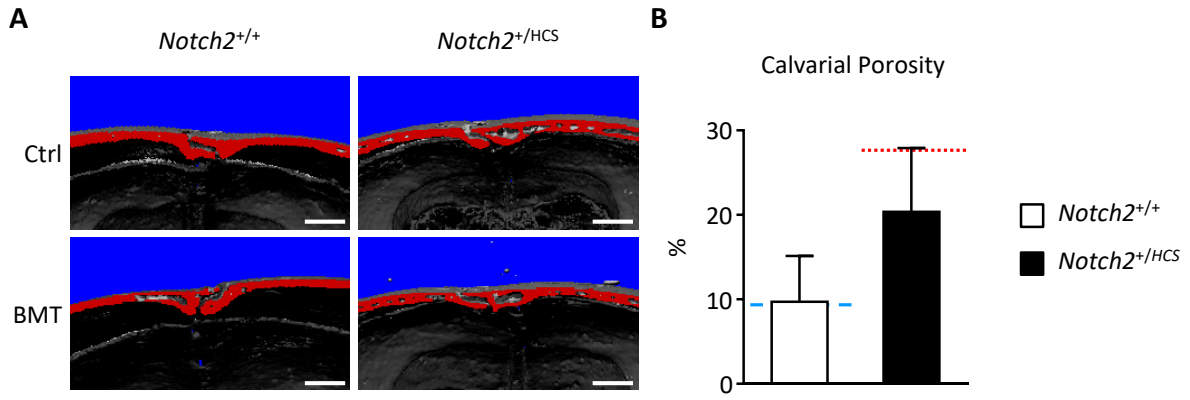

Figure 15: No correction of calvarial porosity after BMT. (A) Representative µCT images of calvarial bone from 24 weeks old *Notch2*$^{+/+}$ and *Notch2*$^{+/HCS}$ mice that have (BMT) or have not (Ctrl) received BMT at the age of 8 weeks. Scale bar=500 µm. **(B)** Quantification of calvarial porosity of bone marrow transplanted *Notch2*$^{+/+}$ and *Notch2*$^{+/HCS}$ mice from A. Dotted lines represent the mean value of calvarial porosity of untreated mice of the corresponding genotype (blue: *Notch2*$^{+/+}$; red: *Notch2*$^{+/HCS}$). Data were analyzed by two-tailed Student´s t test. n≥5 mice per group *p<0.05 vs. age-matched wild-type littermates.

5.1.6 Analysis of *Notch2*$^{+/HCS}$ osteoblasts

To analyze if *Notch2*$^{+/HCS}$ osteoblasts display cell-autonomous alterations causing a high bone formation rate, primary calvarial osteoblasts were cultured in the presence of ascorbic acid and β-glycerophosphate to examine the mineralization capacity of these cells. Quantitative alizarin red staining revealed no difference in mineralization after 10 and 20 days of differentiation (Figure 16A).

Using quantitative real time PCR (qRT PCR) expression analysis, no significant changes in the expression of the osteoblastic marker genes *Runx2* and *Alpl* at day 10 and day 20 of differentiation could be observed (Figure 16B). Both analyses suggest that there is no cell-autonomous gain-of-function of *Notch2*$^{+/HCS}$ osteoblasts causing elevated bone formation.

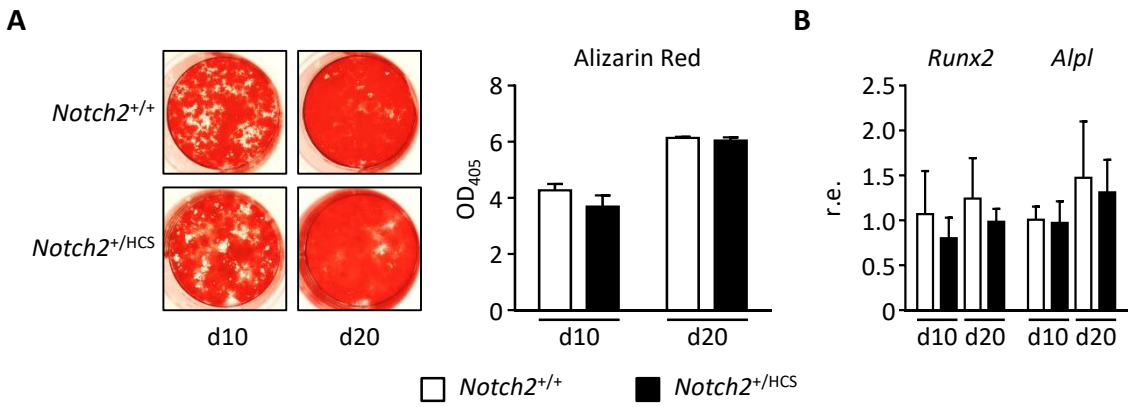

Figure 16: No cell-autonomous defect in *Notch2*$^{+/HCS}$ osteoblasts. (A) Representative images of alizarin red stained *Notch2*$^{+/+}$ and *Notch2*$^{+/HCS}$ bone marrow cells cultured for 10 or 20 days (d) under osteogenic conditions. Quantification of alizarin red staining is shown on the right. Data were analyzed by two-tailed Student´s t test. n=3 samples per group. **(B)** Relative expression (r.e.) levels of *Runx2* and *Alpl* in bone marrow-derived osteoblast cultures at day (d) 10 or 20 of osteogenic differentiation relative to the expression of the same gene in control cells at day 10 of osteogenic differentiation. Data were analyzed by two-tailed Student´s t test. n=3 samples per group.

5.1.7 Gene expression pattern of *Notch2*$^{+/HCS}$ osteoblasts

To find a potential explanation for the observed high bone turnover phenotype in *Notch2*$^{+/HCS}$ mice, an unbiased approach, *i.e.* RNA sequencing, was applied. With this technique, the expression pattern of *Notch2*$^{+/+}$ and *Notch2*$^{+/HCS}$ bone marrow cells at day 7 of osteogenic differentiation was investigated. These cells were additionally incubated for 12 hours with or without recombinant Dll1, which is an established ligand of Notch2. More specifically, the gene expression of *Notch2*$^{+/+}$ and *Notch2*$^{+/HCS}$ osteoblasts treated with or without Dll1 was compared to untreated controls. Using this technique, 27 genes, displaying a signal log ratio (SLR) higher than 1 in all three comparisons, were identified compared to wild-type controls. The most strongly induced gene was the Notch target gene *Heyl*, which is an excellent proof-of-principle for the success of the approach. Furthermore, *Il6* and *Tnfsf11*, encoding IL-6 and Rankl, were strongly induced after Dll1 treatment. These two proteins are known to have a pro-osteoclastogenic influence. Also other induced genes, *i.e. Ocstamp*, *Mmp9*, *Bmp5*, *Lcn2*, *Fgf18*, and *Col20a1* are known to play a role in bone metabolism, but these genes do so far not fit in the elucidation of a potential mechanism causing the HCS specific phenotype (Figure 17A).

In contrast, the expression of genes serving as typical osteoblast differentiation markers was only moderately affected by the HCS mutation or by the treatment of Dll1, ruling out a cell-autonomous gain-of-function in *Notch2*$^{+/HCS}$ osteoblasts (Figure 17B).

A

Gene	SLR: Dll1 vs WT	SLR: HCS vs WT	SLR: HCS & Dll1 vs WT
Heyl	4.88	1.29	6.70
Ocstamp	4.26	3.53	5.74
Fmo2	5.17	1.98	5.62
Mmp9	2.70	4.09	5.54
Abca8a	3.85	1.47	4.96
Bmp6	3.66	2.12	4.84
Slc22a2	2.93	2.61	4.47
Cyp2s1	2.18	3.88	4.36
Il6	3.09	4.30	4.20
Eln	2.13	1.21	4.09
Tnfsf11	2.91	2.28	4.07
Atp9b	1.30	2.46	4.00
Cd300e	1.84	4.05	3.93
Zbtb21	2.60	1.89	3.92
Gzf1	1.31	1.87	3.83
Lcn2	2.72	4.82	3.71
Tmem175	2.37	2.44	3.53
Cxcl9	1.61	4.12	3.52
Ccar1	3.14	2.83	3.51
Tarm1	2.00	3.93	3.47
9530026P05Rik	2.90	2.41	3.29
Ly6i	2.26	3.32	3.20
Fgf18	1.89	1.87	3.16
Mrps35	1.30	2.46	3.15
Alg12	1.90	2.19	3.15
Madd	2.38	1.44	3.15
Col20a1	1.86	1.48	3.08

B

Gene	SLR: Dll1 vs WT	SLR: HCS vs WT	SLR: HCS & Dll1 vs WT
Runx2	-0.01	-0.27	-0.34
Bglap	0.64	-0.36	-0.46
Alpl	0.07	-0.57	-0.49
Spp1	-0.04	-0.63	-0.57
Col1a1	0.13	-0.66	-0.67
Ibsp	0.19	-0.98	-0.79
Phex	0.54	-0.75	-0.85
Sp7	-0.23	-0.51	-0.97
Dmp1	0.47	-0.90	-1.05
Pth1r	-0.32	-0.83	-1.05
Mepe	-0.25	-1.45	-1.90

Figure 17: Expression pattern of *Notch2*$^{+/HCS}$ osteoblasts. (A) 27 genes displaying a signal log ratio (SLR) above 1.0 in all of the three relevant comparisons towards non-treated wild-type cultures (*i.e. Notch2*$^{+/+}$ + Dll1; *Notch2*$^{+/HCS}$; *Notch2*$^{+/HCS}$ + Dll1). Genes were sorted according to the SLR between Dll1-stimulated *Notch2*$^{+/HCS}$ and non-stimulated wild-type cells. **(B)** SLR values of 11 genes serving as osteoblast differentiation markers of the three relevant comparisons towards non-treated wild-type cultures (*i.e. Notch2*$^{+/+}$ + Dll1; *Notch2*$^{+/HCS}$; *Notch2*$^{+/HCS}$ + Dll1). Colors correlate with the SLR value: red=high expression, black=unchanged expression, green=low expression.

The results of the highest-ranked genes obtained from RNA sequencing were additionally tested by qRT PCR expression analysis. Here, the cells were cultured under the same conditions with a Dll1-treatment of 12 hours. The results show a marked increase in the expression of *Heyl*, *Ocstamp*, *Fmo2*, and *Mmp9*. Interestingly, *Notch2*$^{+/HCS}$ cultures reacted more strongly to the treatment of Dll1 than *Notch2*$^{+/+}$ cells supporting the proposed pathomechanism of increased Notch signaling (Figure 18). This confirms the results obtained from RNA sequencing.

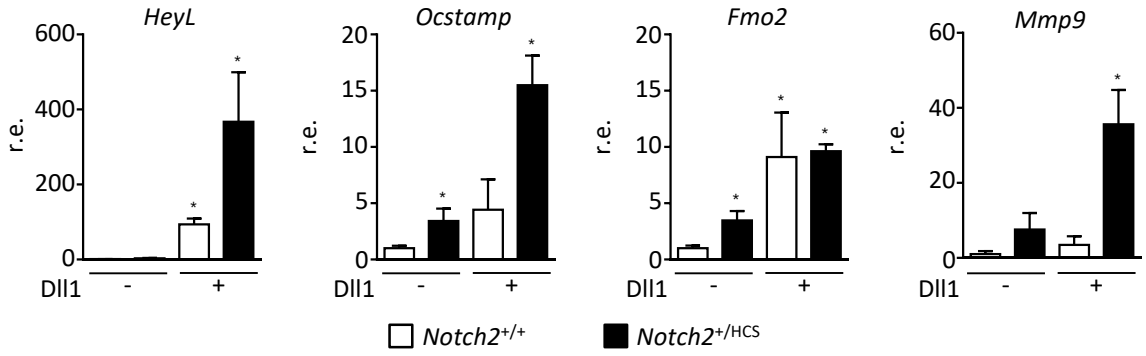

Figure 18: qRT PCR analysis of highest ranked induced genes from RNA sequencing. qRT PCR expression analysis of indicated genes in *ex vivo* bone marrow cultures derived from *Notch2*$^{+/+}$ and *Notch2*$^{+/HCS}$ mice at day 7 of osteogenic differentiation stimulated for 12 h with 100 ng/ml Dll1 relative to non-stimulated *Notch2*$^{+/+}$ control cultures. Data were analyzed by two-tailed Student´s t test. n=3 samples per group; *p<0.05 vs. non-stimulated wild-type littermates.

Likewise, the expression of some selected osteoblast marker genes of the same cells were also tested by qRT PCR expression analyses. The results revealed no significant differences between *Notch2*$^{+/+}$ and *Notch2*$^{+/HCS}$ osteoblasts with or without stimulation of Dll1 in all indicated genes (Figure 19), thereby also verifying the results obtained by RNA sequencing.

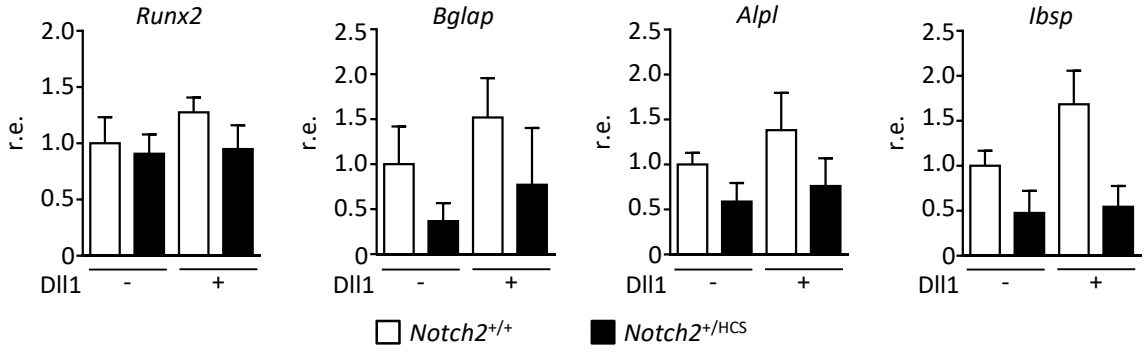

Figure 19: qRT PCR analysis of osteoblast marker genes. qRT PCR expression analysis of indicated genes in *ex vivo* bone marrow cultures derived from *Notch2*$^{+/+}$ and *Notch2*$^{+/HCS}$ mice at day 7 of osteogenic differentiation stimulated for 12 h with 100 ng/ml Dll1 relative to non-stimulated *Notch2*$^{+/+}$ control cultures. Data were analyzed by two-tailed Student´s t test. n=3 samples per group; *p<0.05 vs. non-stimulated wild-type littermates.

Since increased *Il6* and *Rankl* expression could provide the best explanation for the high bone turnover phenotype in *Notch2*$^{+/HCS}$ mice, the expression of both genes was also confirmed by qRT PCR. The results demonstrated that the expression of the indicated genes was highly induced, especially in Dll1-treated *Notch2*$^{+/HCS}$ osteoblasts (Figure 20).

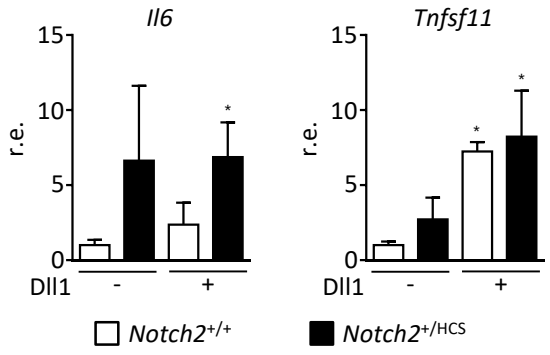

Figure 20: qRT PCR analysis of pro-osteoclastogenic genes. qRT PCR expression analysis of indicated genes in *ex vivo* bone marrow cultures derived from *Notch2*$^{+/+}$ and *Notch2*$^{+/HCS}$ mice at day 7 of osteogenic differentiation stimulated for 12 h with 100 ng/ml Dll1 relative to non-stimulated *Notch2*$^{+/+}$ control cultures. Data were analyzed by two-tailed Student´s t test. n=3 samples per group; *p<0.05 vs. non-stimulated wild-type littermates.

The production of the pro-osteoclastogenic cytokine IL-6 was further measured in cell culture medium conditioned for 72 hours by bone marrow cultures derived from *Notch2*$^{+/+}$ or *Notch2*$^{+/HCS}$ mice. More specifically, these cells were treated for 11 days with or without VitD and dexamethasone (Dex). In line with the results above, IL-6 levels were significantly increased with the addition of VitD and Dex (Figure 21A). Moreover, serum analysis of 24 weeks old *Notch2*$^{+/HCS}$ animals revealed increased IL-6 concentrations compared to wild-type littermates (Figure 21B).

Bone marrow from 24 weeks old *Notch2*$^{+/+}$ and *Notch2*$^{+/HCS}$ mice was analyzed for IL-6 positive cells by immunohistochemistry. The results of this approach revealed a marked increase in IL-6 positive cells in the bone marrow of *Notch2*$^{+/HCS}$ mice compared to wild-type controls, suggesting that the production of IL-6 contributes to the elevated osteoclastogenesis displayed in *Notch2*$^{+/HCS}$ mice (Figure 21C). In contrast, serum concentrations of secreted Rankl revealed no significant differences in *Notch2*$^{+/HCS}$ compared to *Notch2*$^{+/+}$ mice (Figure 21D).

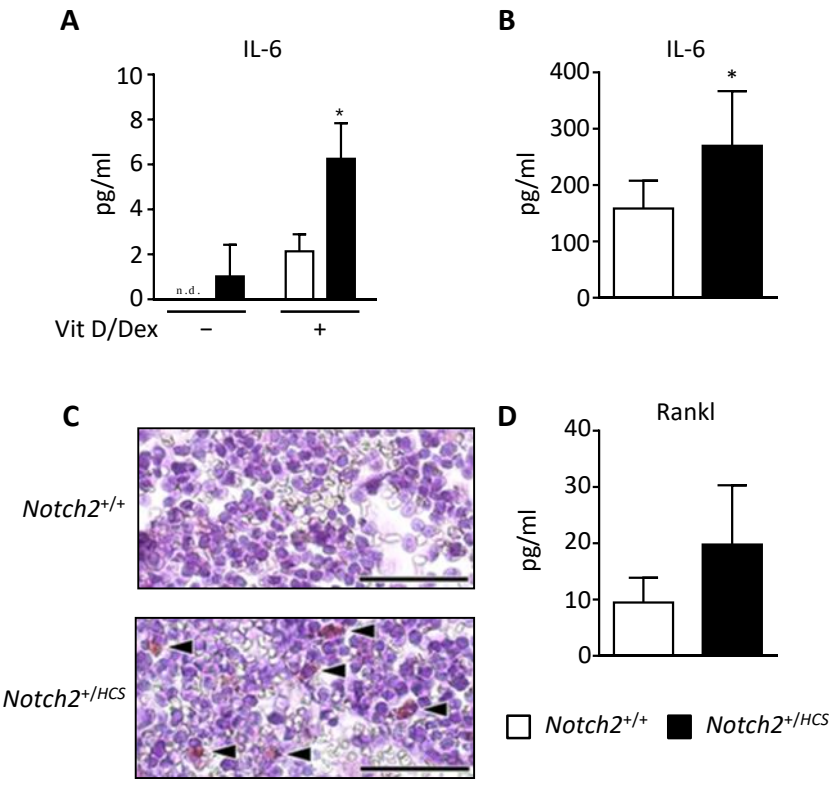

Figure 21: IL-6 is highly expressed in cell culture supernatant and serum of *Notch2$^{+/HCS}$* mice. **(A)** IL-6 concentrations in cell culture medium conditioned for 72 h with bone marrow cells derived from *Notch2$^{+/+}$* and *Notch2$^{+/HCS}$* mice treated for 11 days with or without VitD and Dex. Data were analyzed by two-tailed Student´s t test. n=3 samples per group; *p<0.05 vs. wild-type controls. **(B)** IL-6 serum concentrations in 24 weeks old female *Notch2$^{+/+}$* and *Notch2$^{+/HCS}$* mice. Data were analyzed by two-tailed Student´s t test. n≥5 samples per group; *p<0.05 vs. wild-type controls. **(C)** Representative images of anti-IL-6 stained and hematoxylin counter-stained femur sections from female 24 weeks old *Notch2$^{+/+}$* and *Notch2$^{+/HCS}$* mice. Arrows indicate IL-6 positive cells. Scale bar=50 µm. **(D)** Rankl serum concentrations in 24 weeks old female *Notch2$^{+/+}$* and *Notch2$^{+/HCS}$* mice. Data were analyzed by two-tailed Student´s t test. n≥5 samples per group; *p<0.05 vs. wild-type controls.

5.1.8 Bisphosphonate treatment of *Notch2$^{+/HCS}$* mice

Bisphosphonate treatment is commonly used to prevent bone loss in osteoporotic patients. More specifically, bisphosphonates attach to the bone surface and inhibit the activation of osteoclastic enzymes. It is also known that anti-resorptive bisphosphonate treatment, both in mice and humans causes not only a reduction in bone resorption but also a reduction in bone formation. The latter reduction is potentially explained by impaired release of osteoclastic coupling factors[111-113]. In this thesis, bisphosphonate treatment was performed because the collective findings raised the hypothesis that the increased bone formation found in *Notch2$^{+/HCS}$* mice could be secondary to increased osteoclastogenesis. For that reason, *Notch2$^{+/+}$* and *Notch2$^{+/HCS}$* mice were treated by weekly bisphosphonate injections.

More specifically, alendronate, a bisphosphonate drug used for osteoporosis and other bone diseases, was weekly injected intraperitoneally starting at the age of 18 weeks up to the age of 24 weeks, when the mice were analyzed. The results of the alendronate treatment of *Notch2*$^{+/+}$ and *Notch2*$^{+/HCS}$ mice showed an increase in bone volume visible in both genotypes. In contrast, serum levels of CTx, a biomarker for bone resorption, were significantly decreased by the addition of alendronate in both genotypes, suggesting a successful therapy. Most importantly, the number of osteoblasts and the bone formation rate significantly decreased in both *Notch2*$^{+/+}$ and *Notch2*$^{+/HCS}$ mice, indicating that the observed increased bone formation arises secondary to increased osteoclastogenesis (Figure 22).

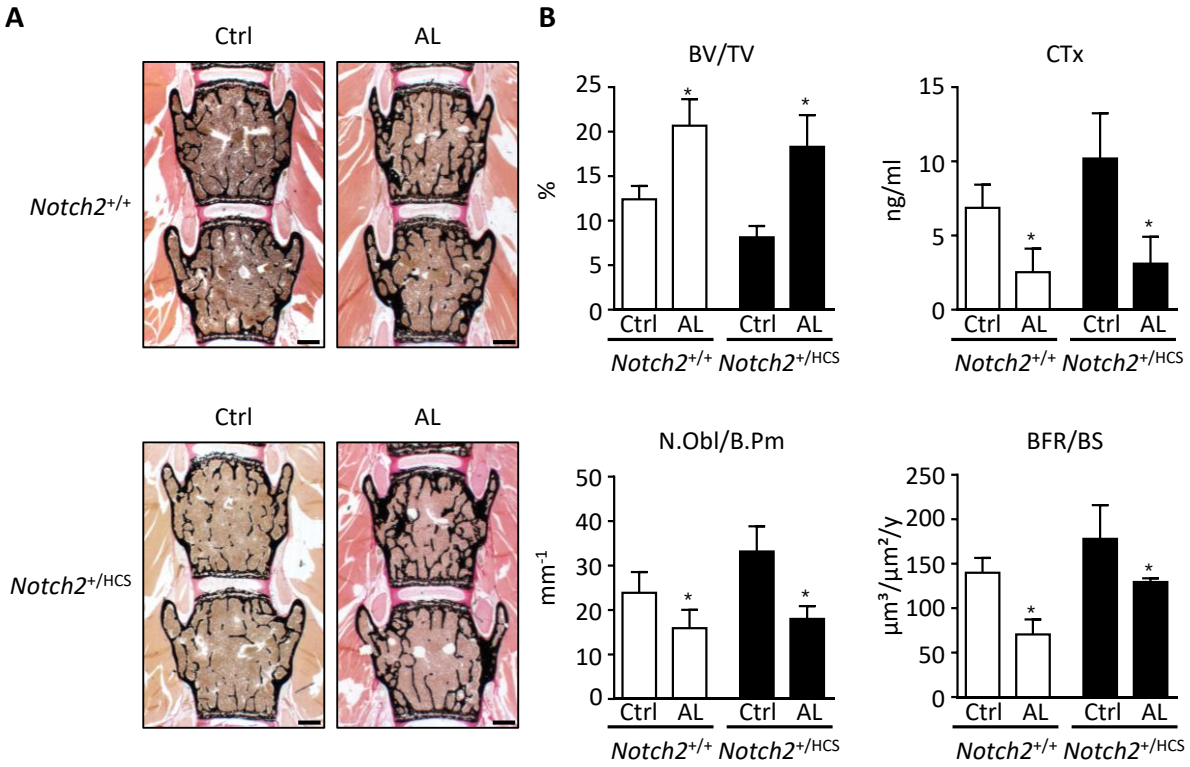

Figure 22: Alendronate treatment corrected increased bone formation in *Notch2*$^{+/HCS}$ mice. **(A)** Representative images of von Kossa/van Giesson-stained undecalcified spine sections from 24 weeks old female *Notch2*$^{+/+}$ and *Notch2*$^{+/HCS}$ mice treated for 6 weeks with 300 µg/kg/w alendronate (AL) or the equivalent volume of PBS as a control (Ctrl). Scale bar=500 µm. **(B)** Quantification of histomorphometric parameters in spine sections and CTx values in the serum of alendronate-treated (AL) and control (Ctrl) female *Notch2*$^{+/+}$ and *Notch2*$^{+/HCS}$ mice from A. Data were analyzed by two-tailed Student´s t test. n=5 mice per group; *p<0.05 vs. genotype-matched controls.

5.2 S1pr3-deficient mice

5.2.1 S1P as an osteoclast-released coupling factor in *Notch2$^{+/HCS}$* mice

Since the elevated bone formation found in *Notch2$^{+/HCS}$* mice was observed to be secondary to increased osteoclastogenesis, it was of high importance to identify specific coupling factors causing this phenotype. One recently identified coupling factor, known to be released by osteoclasts and having a stimulating effect on osteoblasts and bone formation, is S1P. It acts by binding to its receptor S1pr3 on osteoblasts, thus, increasing bone formation[43]. To address the question, if the high bone formation phenotype in *Notch2$^{+/HCS}$* mice depends on S1P, *S1pr3*-deficient mice (*S1pr3$^{-/-}$*) were crossed with *Notch$^{+/HCS}$* mice to generate *Notch2$^{+/+}$*, *Notch2$^{+/HCS}$* and *Notch2$^{+/HCS}$*; *S1pr3$^{-/-}$* mice. These mice were analyzed by histomorphometric analysis of spine sections at the age of 24 weeks. It was observed that *Notch2$^{+/HCS}$*; *S1pr3$^{-/-}$* mice still displayed osteopenia and a significantly elevated bone formation rate compared to wild-type controls. Most importantly, there were no significant changes between *Notch2$^{+/HCS}$* and *Notch2$^{+/HCS}$*; *S1pr3$^{-/-}$* littermates observed (Figure 23). These data essentially exclude S1P as a potential coupling factor causing the bone phenotype in *Notch2$^{+/HCS}$* mice.

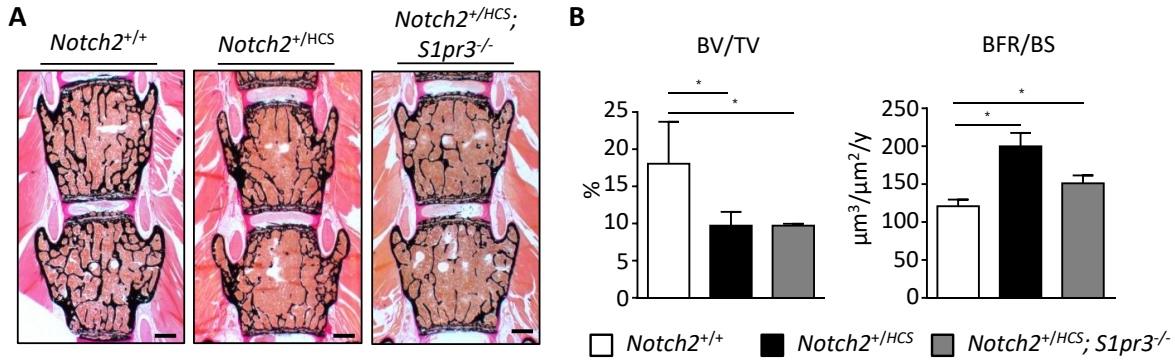

Figure 23: S1P is not a potential coupling factor causing the HCS phenotype. (A) Representative images of von Kossa/van Giesson-stained undecalcified spine sections from 24 weeks old female *Notch2$^{+/+}$*, *Notch2$^{+/HCS}$*, and *Notch2$^{+/HCS}$; S1pr3$^{-/-}$* mice. Scale bar=500 µm. **(B)** Quantification of histomorphometric parameters in spine sections from female *Notch2$^{+/+}$*, *Notch2$^{+/HCS}$*, and *Notch2$^{+/HCS}$; S1pr3$^{-/-}$* mice from A. Data were analyzed by two-tailed Student´s t test. n≥4 mice per group; *p<0.05 vs. genotype-matched controls.

5.3 Wnt1-floxed mice

5.3.1 Wnt1 as an osteoclast-released coupling factor

The recent identification of osteoclastic Wnt1 secretion potentially coupling bone resorption and formation further led to the assumption that increased Wnt1 production by osteoclasts could be a potential cause of the increased bone formation in *Notch2*$^{+/HCS}$ mice[46]. To initially study the role of Wnt1 in osteoclasts in more detail, mice with a conditional inactivation of *Wnt1* in cells of the osteoclast lineage (*Wnt1*$^{fl/fl;\ Lyz2\text{-}Cre}$ mice) were utilized and cultured osteoclasts were isolated from *Wnt1*$^{fl/fl}$ or *Wnt1*$^{fl/fl;\ Lyz2\text{-}Cre}$ mice. The efficacy of Lyz2-Cre-mediated recombination was confirmed by genomic PCR in different tissues and cultured osteoclasts (Figure 24A). Importantly, µCT analyses demonstrated that trabecular bone volume and cortical thickness were not significantly different between *Wnt1*$^{fl/fl}$ and *Wnt1*$^{fl/fl;\ Lyz2\text{-}Cre}$ mice (Figure 24C). These data reveal that osteoclast-mediated Wnt1 secretion does not affect bone formation nor bone resorption in this transgenic mouse model, which furthermore excluded Wnt1 from being a potential coupling factor causing increased bone formation in *Notch2*$^{+/HCS}$ mice.

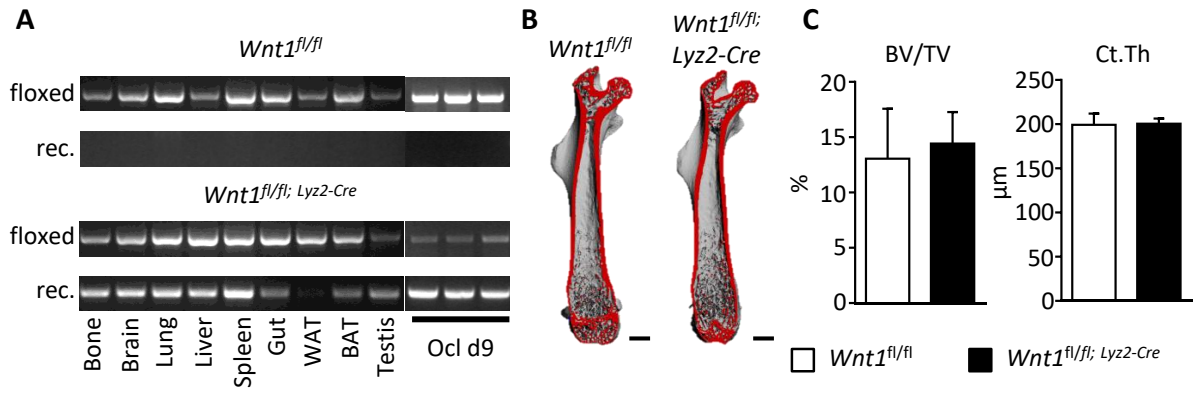

Figure 24: No bone phenotype in *Wnt1*$^{fl/fl;\ Lyz2\text{-}Cre}$ mice. (A) Recombination analysis of various tissues and cultured osteoclasts (Ocl) at day (d) 9 of osteogenic differentiation isolated from *Wnt1*$^{fl/fl}$ and *Wnt1*$^{fl/fl;\ Lyz2\text{-}Cre}$ mice. rec: recombined. WAT: white adipose tissue. BAT: brown adipose tissue. **(B)** Representative µCT images of femora from male *Wnt1*$^{fl/fl}$ and *Wnt1*$^{fl/fl;\ Lyz2\text{-}Cre}$ mice at 24 weeks of age. The virtual cutplane appears in red. Scale bar=1 mm. **(C)** Quantification of BV/TV and Ct.Th of µCT analyses from B. Data were analyzed by two-tailed Student´s t test. n≥4 mice per group; *p<0.05 vs. genotype-matched controls.

Since osteoclast-specific Wnt1 inactivation did not have an effect on the bone structure, the function of Wnt1 on bone was further studied in mice with an osteoblast-specific *Wnt1* inactivation (*Wnt1*$^{fl/fl;\ Runx2\text{-}Cre}$ mice). Here, the *Runx2-Cre*-mediated recombination was specifically observed in bone and cultured osteoblasts of *Wnt1*$^{fl/fl;\ Runx2\text{-}Cre}$ mice, whereas tissues and osteoblasts derived from *Wnt1*$^{fl/fl}$ mice as a control did not display a recombined *Wnt1* allele (Figure 25A). µCT analysis of *Wnt1*$^{fl/fl;\ Runx2\text{-}Cre}$ mice further revealed a significant reduction of trabecular bone volume and cortical thickness compared to *Wnt1*$^{fl/fl}$ controls (Figure 25C).

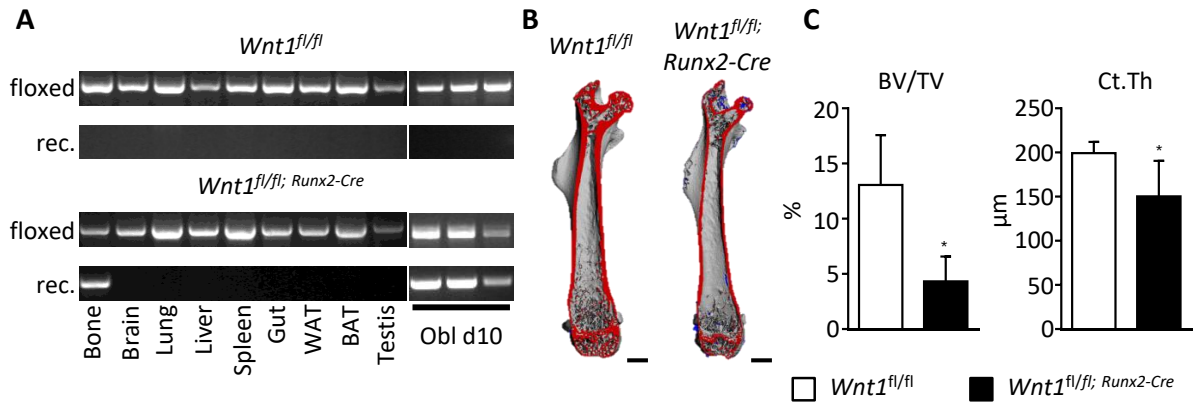

Figure 25: Osteopenic phenotype in *Wnt1*$^{fl/fl;\ Runx2\text{-}Cre}$ mice. (A) Recombination analysis of various tissues and cultured osteoblasts (Obl) at day (d) 10 of osteogenic differentiation isolated from *Wnt1*$^{fl/fl}$ and *Wnt1*$^{fl/fl;\ Runx2\text{-}Cre}$ mice. rec: recombined. WAT: white adipose tissue. BAT: brown adipose tissue. **(B)** Representative µCT images of femora from male *Wnt1*$^{fl/fl}$ and *Wnt1*$^{fl/fl;\ Runx2\text{-}Cre}$ mice at 24 weeks of age. The virtual cutplane appears in red. Scale bar=1 mm. **(C)** Quantification of BV/TV and Ct.Th of µCT analyses from B. Data were analyzed by two-tailed Student´s t test. n≥4 mice per group; *p<0.05 vs. genotype-matched controls.

Most importantly, however, when analyzing *Wnt1*$^{fl/fl}$, *Wnt1*$^{fl/fl;\ Runx2\text{-}Cre}$ and *Wnt1*$^{fl/fl;\ Lyz2\text{-}Cre}$ mice by contact X-ray, multiple skeletal fractures were observed in *Wnt1*$^{fl/fl;\ Runx2\text{-}Cre}$ mice but not in *Wnt1*$^{fl/fl;\ Lyz2\text{-}Cre}$ mice and controls (Figure 26A). More specifically, 38 % of all fractures observed were tibial fractures, 30 % were rib fractures, 9 % hip fractures, 9 % radius fractures, 9 % ulna fractures, and 5 % femoral fractures (Figure 26B). Furthermore, by µCT analysis and von Kossa/van Giesson-stained undecalcified sections of the tibia, the observed skeletal fractures of *Wnt1*$^{fl/fl;\ Runx2\text{-}Cre}$ mice were found to display callus formation, thus indicating that fracture healing was still possible and that fractures did not appear when mice were dissected (Figure 26C). In summary, the absence of *Wnt1* in osteoblasts causes osteoporosis with high bone fragility, whereas *Wnt1* deletion in osteoclasts did not result in

an altered bone phenotype. This finding furthermore highlighted the importance of *Wnt1* expression in osteoblasts.

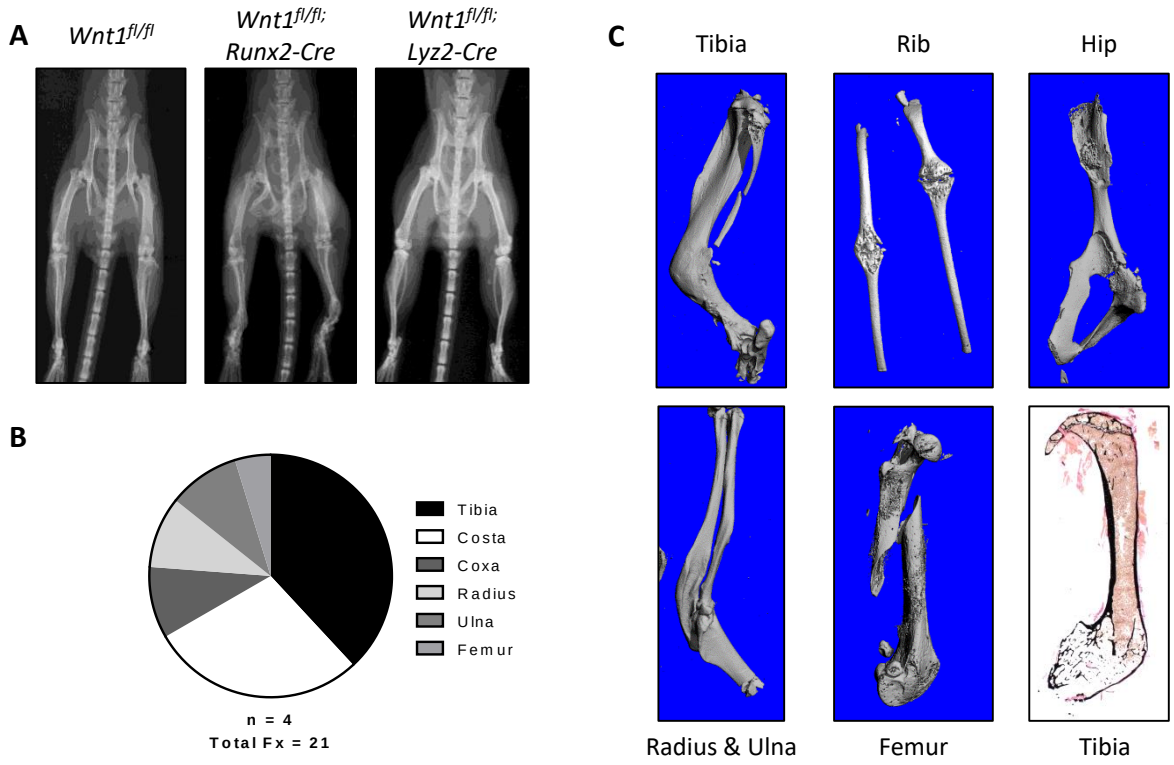

Figure 26: Multiple skeletal fractures in *Wnt1*$^{fl/fl;\ Runx2\text{-}Cre}$ mice. (A) Representative contact X-ray images of male *Wnt1*$^{fl/fl}$, *Wnt1*$^{fl/fl;\ Runx2\text{-}Cre}$ and *Wnt1*$^{fl/fl;\ Lyz2\text{-}Cre}$ mice at 24 weeks of age. **(B)** Frequency distribution of fractures observed in *Wnt1*$^{fl/fl;\ Runx2\text{-}Cre}$ mice at 24 weeks of age. n=4 mice carrying 21 fractures in total. **(C)** µCT images of fractured tibia, rib, hip, radius and ulna, and femur observed in *Wnt1*$^{fl/fl;\ Runx2\text{-}Cre}$ mice. Undecalcified section of a fractured tibia observed in a *Wnt1*$^{fl/fl;\ Runx2\text{-}Cre}$ mouse at the age of 24 weeks.

5.4 Wnt1^{G177C} mice

5.4.1 Initial characterization of the *Wnt1*^{G177C} mouse model

Because the generalized osteoporosis with high bone fragility in *Wnt1*$^{fl/fl;\ Runx2\text{-}Cre}$ mice phenocopies the skeletal pathologies found in patients with homozygous *WNT1* mutations causing OI type XV, one of the previously described causing mutations (G177C) was introduced into the murine *Wnt1* gene[105].

Sponsored by the European Community´s Seventh Framework Programme (SYBIL), a G177C mutation was introduced into the murine *Wnt1* gene by Polygene AG, Switzerland. A corresponding targeting plasmid was transfected into embryonic stem cells (Figure 27A). After blastocyst injection of positive clones, chimeric mice were mated to obtain $Wnt1^{+/G177C}$ mice. These heterozygous mice were then intercrossed to obtain homozygous $Wnt^{G177C7/G177C}$ offspring. To identify the presence of the G177C mutation in a heterozygous or homozygous state, Sanger sequencing analyses were performed. These analyses confirmed the existence of the G177C mutation as well as a silent mutation 5 bp more upstream of the actual mutation in $Wnt1^{+/G177C}$ and $Wnt^{G177C7/G177C}$ mice (Figure 27B).

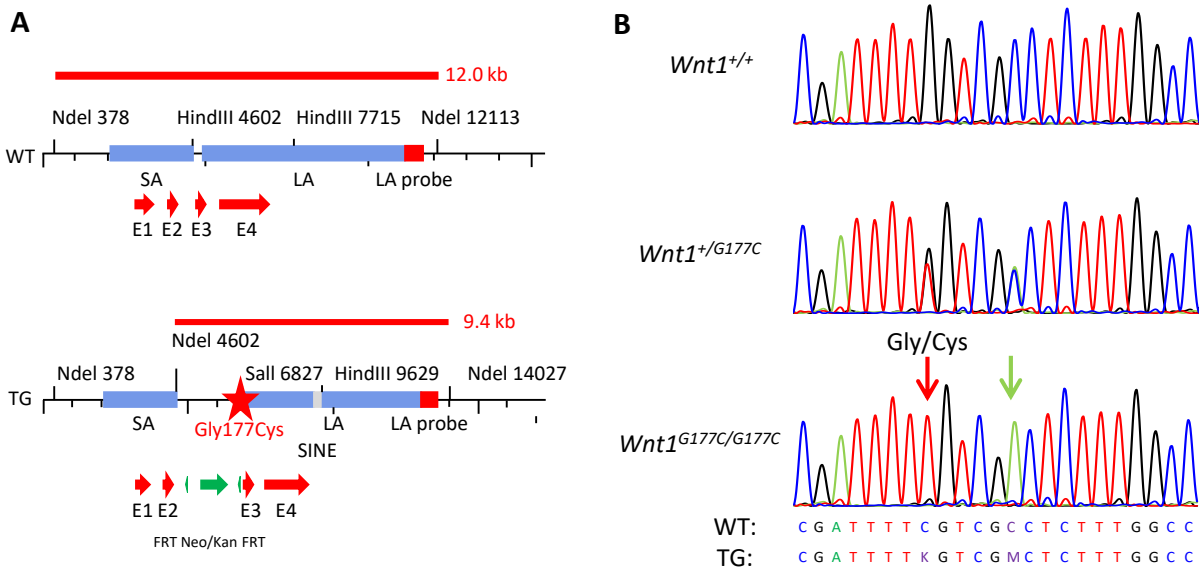

Figure 27: Generation of a mouse model carrying the Wnt1^{G177C} mutation. (A) Schematic representation of wild-type (WT) and mutated (TG) *Wnt1* allele. Thin red line: fragments detectable by southern blot after restriction with NdeI; blue bars: homologous regions for recombination; red bars: binding site for southern blot (LA) probe; red star: introduced point mutation; red arrows: Wnt1 exons 1-4; green triangle: FRT site; green arrow: neomycin cassette; SA: short arm; LA: long arm. **(B)** Sanger sequencing results of $Wnt1^{+/+}$, $Wnt1^{+/G177C}$, and $Wnt1^{G177C/G177C}$ mice. Red arrow: mutation resulting in amino acid exchange; green arrow: silent mutation.

To examine whether $Wnt1^{+/+}$, $Wnt1^{+/G177C}$, and $Wnt1^{G177C/G177C}$ animals were viable, the survival rate of all three genotypes was analyzed at the age of 3 weeks. This analysis revealed that $Wnt1^{G177C/G177C}$ mice were born at the expected Mendelian ratio and did not display perinatal lethality until the age of 3 weeks (Figure 28).

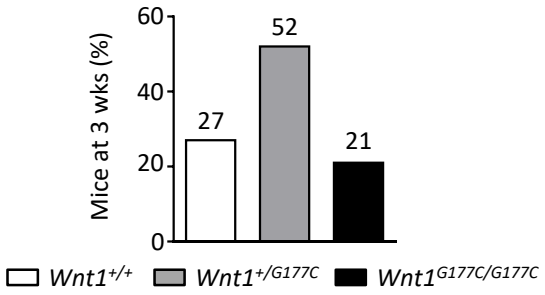

Figure 28: *Wnt1*$^{G177C/G177C}$ did not display perinatal lethality. Genotype ratio of *Wnt1*$^{+/+}$, *Wnt1*$^{+/G177C}$, and *Wnt1*$^{G177C/G177C}$ mice at 3 weeks (wks) of age. Numbers on top of bars indicate the number of animals. Data were analyzed by χ^2 test.

5.4.2 Brain phenotype of *Wnt1*$^{G177C/G177C}$ mice

Since *Wnt1*$^{sw/sw}$ mice have been described to display a combination of osteoporosis and cerebellar defects[109, 114], we first analyzed if *Wnt1*$^{G177C/G177C}$ mice also have a brain phenotype. Using histological stainings specific for structures in cortex, hippocampus and cerebellum of mice, no morphological differences in all 3 brain regions were observed in 4 weeks old *Wnt1*$^{G177C/G177C}$ mice compared to wild-type controls (Figure 29A, 29B). Furthermore, layer thickness analysis of cortical Cut like Homeobox 1 (Cux1)-positive cells as well as the number of doublecortin (DCX)-positive neuroblasts in the subgranular zone were unaltered compared to controls (Figure 29C, 29D). In summary, these results indicate that *Wnt1*$^{G177C/G177C}$ mice do not display an alteration in brain development and morphology, unlike it is has been described for the *Wnt1*$^{sw/sw}$ mice.

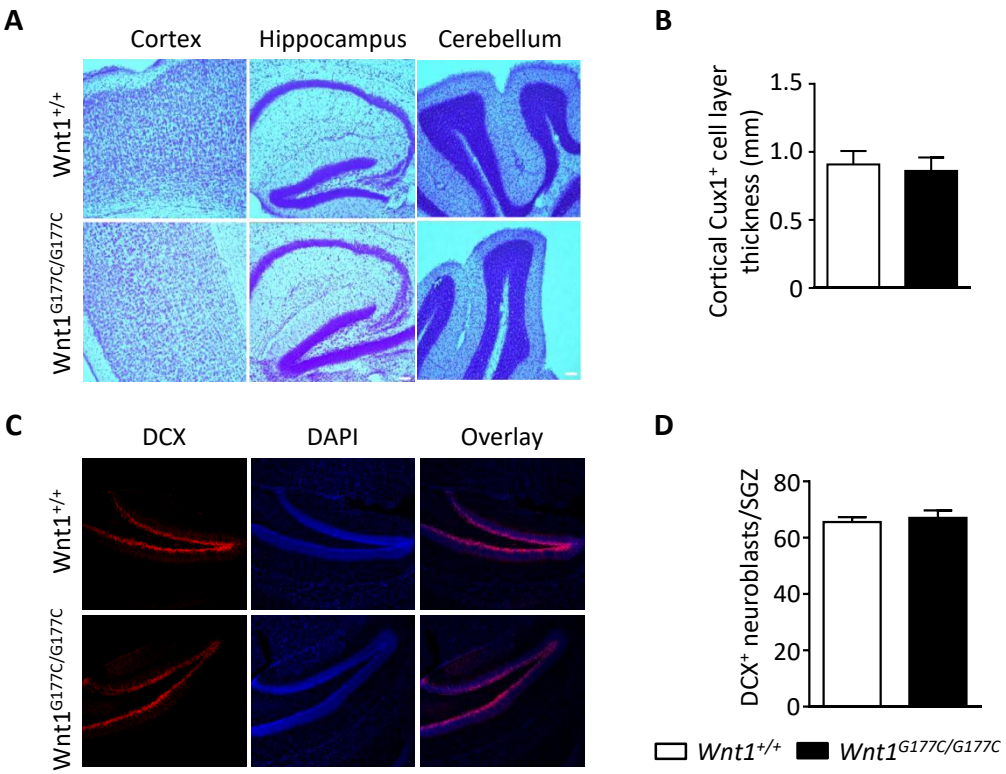

Figure 29: *Wnt1*$^{G177C/G177C}$ mice do not display a brain phenotype at 4 weeks of age. (A) Representative images of Niss1 stained sections of the cortex, hippocampus and cerebellum from 4 weeks old male *Wnt1*$^{+/+}$ and *Wnt1*$^{G177C/G177C}$ mice. **(B)** Quantification of cortical Cux1-positive cell layer thickness. **(C)** Representative immunofluorescent images of hippocampus region in 4 weeks old male *Wnt1*$^{+/+}$ and *Wnt1*$^{G177C/G177C}$ mice. Red: Anti-doublecortin (DCX), Blue: DAPI. **(D)** Quantification of DCX-positive neuroblasts in the subgranular zone (SGZ) of the hippocampus. Data were analyzed by two-tailed Student´s t test. n=3 mice per group.

5.4.3 Skeletal phenotype of *Wnt1*$^{G177C/G177C}$ mice

To first investigate if the mutation has an impact on skeletal growth, 4 weeks old *Wnt1*$^{+/+}$, *Wnt1*$^{+/G177C}$, and *Wnt1*$^{G177C/G177C}$ male and female mice were analyzed for the length of femur and tibia, for alterations of growth plate morphology, and for growth plate thickness (GP.Th). Both the analysis of femur and tibia lengths revealed no differences in male and female *Wnt1*$^{+/+}$, *Wnt1*$^{+/G177C}$, and *Wnt1*$^{G177C/G177C}$ mice at 4 weeks of age (Figure 30A). Furthermore, no alterations in growth plate morphology and growth plate thickness were observed (Figure 30B, 30C), indicating that the Wnt1^{G177C} mutation in mice had no impact on skeletal growth.

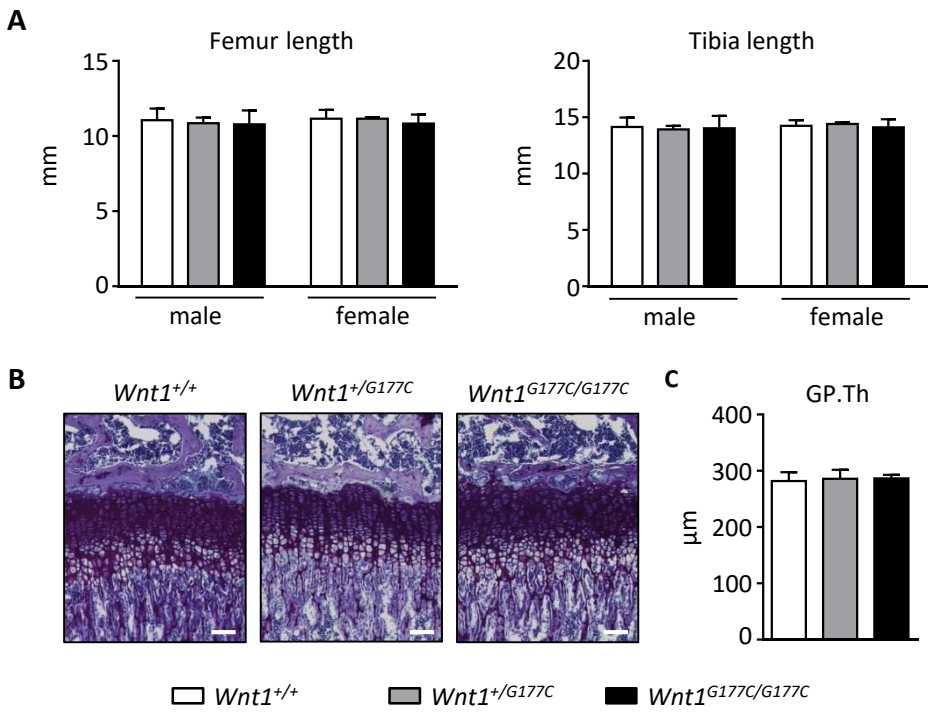

Figure 30: Skeletal morphology of *Wnt1*$^{G177C/G177C}$ mice at 4 weeks of age. (A) Quantification of femoral and tibial length of female and male *Wnt1*$^{+/+}$, *Wnt1*$^{+/G177C}$, and *Wnt1*$^{G177C/G177C}$ mice. **(B)** Representative images of toluidine blue stained sections showing the proximal tibia growth plate of male *Wnt1*$^{+/+}$, *Wnt1*$^{+/G177C}$, and *Wnt1*$^{G177C/G177C}$ mice. Scale bar=100 µm. **(C)** Quantification of the proximal tibia growth plate thickness of male *Wnt1*$^{+/+}$, *Wnt1*$^{+/G177C}$, and *Wnt1*$^{G177C/G177C}$ mice. Data were analyzed by two-tailed Student´s t test with Bonferroni correction. n≥3 mice per group.

Furthermore, using µCT, the femora of 4 weeks old *Wnt1*$^{+/+}$, *Wnt1*$^{+/G177C}$, and *Wnt1*$^{G177C/G177C}$ male and female mice were analyzed. This revealed a significant reduction in trabecular bone volume in *Wnt1*$^{G177C/G177C}$ mice compared to *Wnt1*$^{+/+}$ and *Wnt1*$^{+/G177C}$ littermates, in both male and female mice (Figure 31B).

Analysis of cortical thickness revealed a significant reduction in male and female *Wnt1*$^{G177C/G177C}$ mice compared to *Wnt1*$^{+/+}$ and *Wnt1*$^{+/G177C}$ littermates. In contrast, there was no significant difference observed in cortical porosity (Ct. Por) between the groups (Figure 31C).

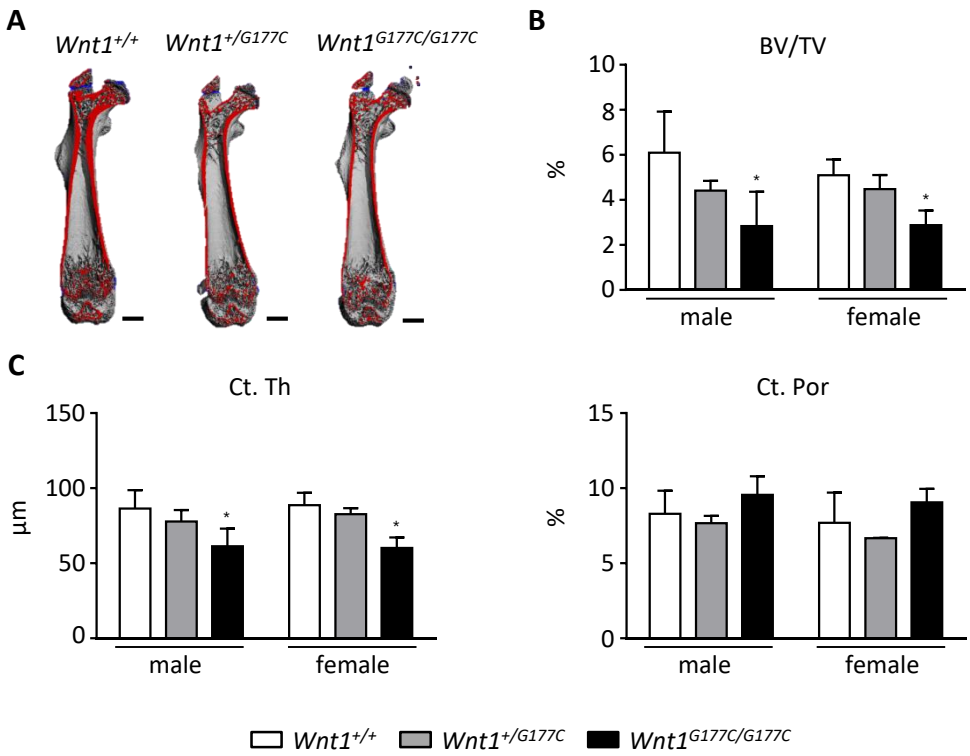

Figure 31: *Wnt1*$^{G177G/G177C}$ mice display osteopenia in the femur at 4 weeks of age. (A) Representative µCT images of femora from male *Wnt1*$^{+/+}$, *Wnt1*$^{+/G177C}$, and *Wnt1*$^{G177C/G177C}$ mice. The virtual cutplane appears red. Scale bar=1 mm. **(B)** Quantification of BV/TV in the distal femoral metaphysis of male and female *Wnt1*$^{+/+}$, *Wnt1*$^{+/G177C}$, and *Wnt1*$^{G177C/G177C}$ mice from A. **(C)** Quantification of Ct. Th and Ct. Por in the central diaphysis of male and female *Wnt1*$^{+/+}$, *Wnt1*$^{+/G177C}$ and *Wnt1*$^{G177C/G177C}$ mice from A. Data were analyzed by two-tailed Student´s t test with Bonferroni correction. n≥4 mice per group; *p<0.05 vs. genotype-matched controls.

The observed osteopenic phenotype was also analyzed by undecalcified histology of spine sections. Here, the trabecular bone volume was reduced in *Wnt1*$^{G177C/G177C}$ mice compared to littermate controls, in both, male and female mice. Furthermore, the trabecular bone volume was also reduced in male *Wnt1*$^{+/G177C}$ mice compared to controls (Figure 32B). The same extend of reduction was found for the osteoblast indices, whereas the number of osteoclasts was significantly increased only in female *Wnt1*$^{G177C/G177C}$ mice compared to littermate controls (Figure 32C). Summarized, these results indicate that the G177C mutation had a negative impact on the trabecular and cortical bone, yet this skeletal phenotype appeared rather moderate compared to the phenotype observed in *Wnt1*$^{sw/sw}$ mice[109].

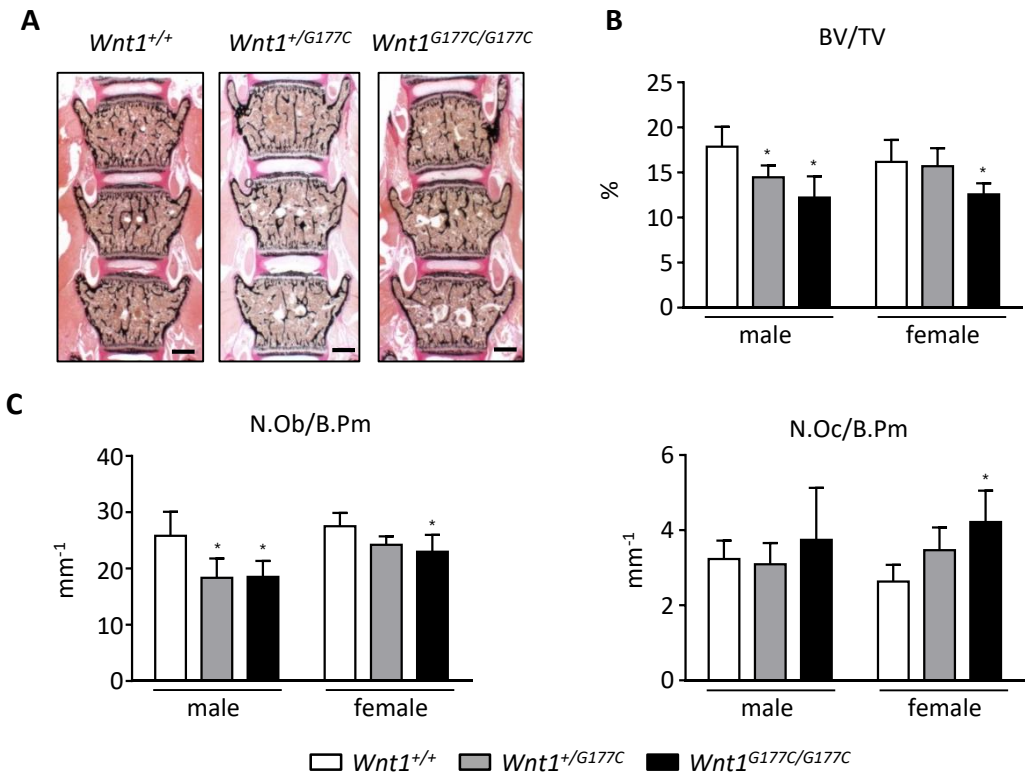

Figure 32: *Wnt1*$^{G177G/G177C}$ mice display osteopenia in the spine at 4 weeks of age. (A) Representative images of undecalcified spine sections from male *Wnt1*$^{+/+}$, *Wnt1*$^{+/G177C}$ and *Wnt1*$^{G177C/G177C}$ mice. Scale bar=500 µm. **(B)** Quantification of BV/TV in the lumbar vertebral bodies of male and female *Wnt1*$^{+/+}$, *Wnt1*$^{+/G177C}$, and *Wnt1*$^{G177C/G177C}$ mice from A. **(C)** Quantification of the N.Obl/B.Pm and N.Oc/B.Pm in the lumbar vertebral bodies of male and female *Wnt1*$^{+/+}$, *Wnt1*$^{+/G177C}$, and *Wnt1*$^{G177C/G177C}$ mice from A. Data were analyzed by two-tailed Student´s t test with Bonferroni correction. n≥4 mice per group; *p<0.05 vs. genotype-matched controls.

We next analyzed, if *Wnt1*$^{G177C/G177C}$ mice would display a more pronounced low bone mass phenotype at 24 weeks of age. Here we found by contact X-ray that the majority of *Wnt1*$^{G177C/G177C}$ mice, but not *Wnt1*$^{+/+}$ and *Wnt1*$^{+/G177C}$ littermates, displayed multiple skeletal fractures in the rib cage, tibiae and hips (Figure 33A). Rib fractures were mostly found in male *Wnt1*$^{G177C/G177C}$ mice, whereas hip fractures were only identified in female *Wnt1*$^{G177C/G177C}$ animals (Figure 33B). Furthermore, undecalcified histology revealed an over-abundance of adipocytes in the fracture callus of tibial fractures in *Wnt1*$^{G177C/G177C}$ mice, suggesting that fracture healing could be impaired as well (Figure 33C). Additionally, non-fractured tibiae of *Wnt1*$^{G177C/G177C}$ mice displayed a significantly increased number of adipocytes (N.Ad/M.Ar) as well (Figure 33D and E).

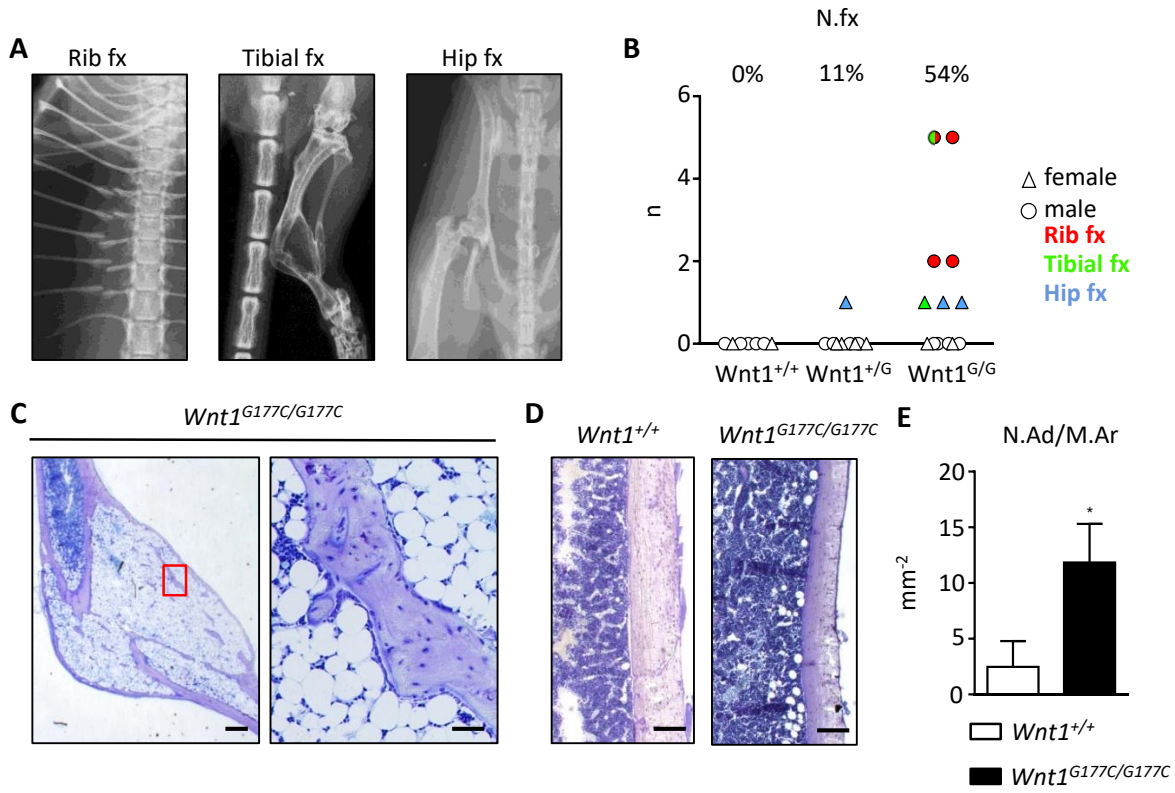

Figure 33: Multiple skeletal fractures in *Wnt1*$^{G177C/G177C}$ mice at 24 weeks of age. (A) Exemplary contact X-rays of fractures (fx) observed in *Wnt1*$^{G177C/G177C}$ mice. **(B)** Quantification of observed location of fractures in *Wnt1*$^{+/+}$, *Wnt1*$^{+/G177C}$, and *Wnt1*$^{G177C/G177C}$ mice. Each point represents one mouse. The shape indicates the gender, the color indicates the location of the fracture. N.Fx = Number of fractures. **(C)** Exemplary image of toluidine blue-stained fractured tibia observed in a *Wnt1*$^{G177C/G177C}$ mouse. Left scale bar=500 µm, Right scale bar=50 µm. **(D)** Representative images of toluidine blue-stained non-fractured tibiae at the cortical diaphysis from *Wnt1*$^{+/+}$ and *Wnt1*$^{G177C/G177C}$ mice. Scale bar=100 µm **(E)** Quantification of the N.Ad/M.Ar in the diaphysis of non-fractured tibiae from male *Wnt1*$^{+/+}$ and *Wnt1*$^{G177C/G177C}$ mice. Data were analyzed by two-tailed Student´s t test. n≥3 mice per group; *p<0.05 vs. genotype-matched controls.

Analysis of undecalcified spine sections of *Wnt1*$^{+/+}$, *Wnt1*$^{+/G177C}$, and *Wnt1*$^{G177C/G177C}$ mice at 24 weeks of age revealed a moderate, but significant decrease of trabecular bone volume, trabecular thickness and osteoblast number per bone surface in *Wnt1*$^{G177C/G177C}$ mice compared to *Wnt1*$^{+/+}$ and *Wnt1*$^{+/G177C}$ littermates. Moreover, the bone formation rate was significantly reduced in non-fractured *Wnt1*$^{G177C/G177C}$ mice compared to *Wnt1*$^{+/+}$ and *Wnt1*$^{+/G177C}$ controls (Figure 34).

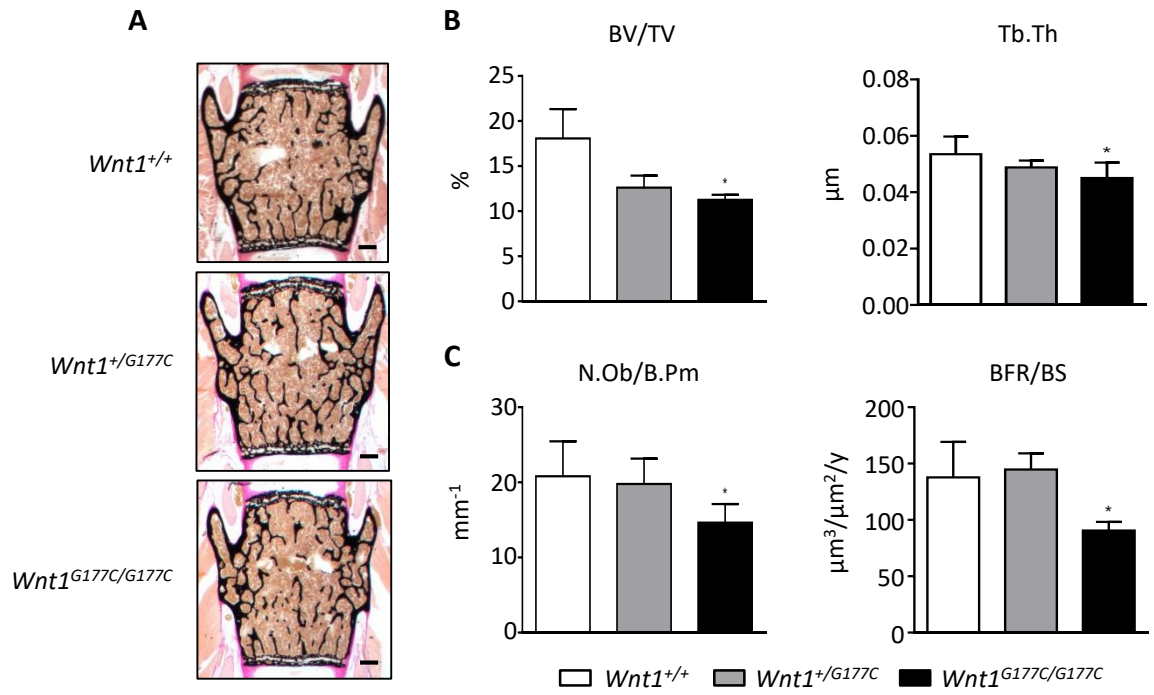

Figure 34: *Wnt1*$^{G177G/G177C}$ mice display osteopenia in the spine at 24 weeks of age. (A) Representative images of undecalcified spine sections stained after von Kossa/van Giesson from male *Wnt1*$^{+/+}$, *Wnt1*$^{+/G177C}$, and *Wnt1*$^{G177C/G177C}$ mice. Scale bar=1000 µm **(B)** Quantification of BV/TV and Tb.Th in the lumbar vertebral bodies of male *Wnt1*$^{+/+}$, *Wnt1*$^{+/G177C}$ and *Wnt1*$^{G177C/G177C}$ mice from A. **(C)** Quantification the N.Ob/B.Pm and BFR/BS in the lumbar vertebral bodies of male *Wnt1*$^{+/+}$, *Wnt1*$^{+/G177C}$, and *Wnt1*$^{G177C/G177C}$ mice from A. Data were analyzed by two-tailed Student´s t test with Bonferroni correction. n≥3 mice per group; *p<0.05 vs. genotype-matched controls.

Using µCT analysis, both trabecular bone mass and cortical thickness were significantly reduced in femora from 24 weeks old *Wnt1*$^{G177C/G177C}$ mice compared to *Wnt1*$^{+/+}$ and *Wnt1*$^{+/G177C}$ littermate controls (Figure 35). Taken together, the skeletal analysis of this mouse model suggested that the *G177C* mutation only moderately affects bone mass, but as indicated by the high fracture rate, appears to have a profound negative influence on bone quality.

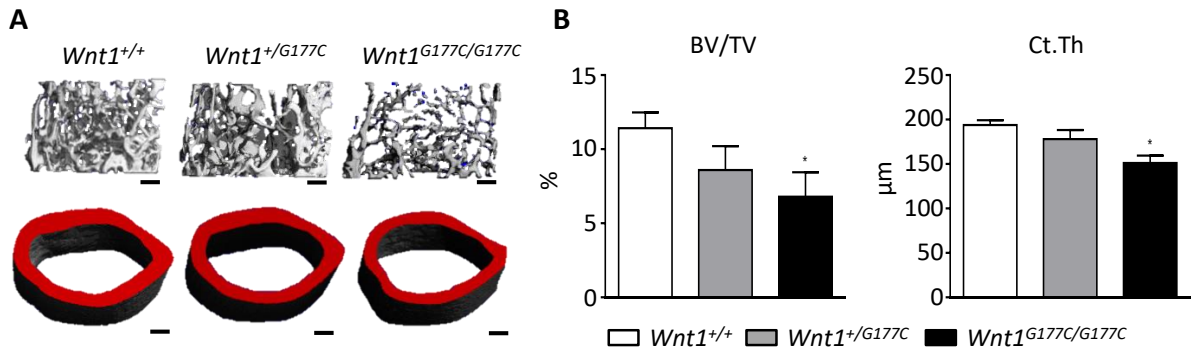

Figure 35: *Wnt1*$^{G177G/G177C}$ mice display osteopenia in the femur at 24 weeks of age. (A) Representative µCT images of the femoral trabecular (distal metaphysis) and cortical (central diaphysis) compartment from male *Wnt1*$^{+/+}$, *Wnt1*$^{+/G177C}$, and *Wnt1*$^{G177C/G177C}$ mice. The virtual cutplane appears in red. Scale bar=200 µm **(B)** Quantification of BV/TV in the distal femoral metaphysis and Ct.Th at the central disphysis of male *Wnt1*$^{+/+}$, *Wnt1*$^{+/G177C}$, and *Wnt1*$^{G177C/G177C}$ mice from A. Data were analyzed by two-tailed Student´s t test with Bonferroni correction. n≥3 mice per group; *p<0.05 vs. *Wnt1*$^{+/+}$ littermates.

5.4.4 Biomechanical analysis of *Wnt1*$^{G177C/G177C}$ mice

Bone strength, in general, is determined by bone quantity and bone quality. As the G177C mutation in murine *Wnt1* seemed to have only a moderate effect on bone mass, the bone quality was investigated in more detail. To first evaluate the stiffness and strength of *Wnt1*$^{G177C/G177C}$ bones, a three-point bending-test was performed. For this technique, femora of 24 weeks old *Wnt1*$^{G177C/G177C}$ and littermate control mice were tested for mechanical properties of the mid-diaphysis. The testing revealed a significant decrease in maximum force the bone can withstand (F_{max}). Furthermore, a significant reduction of work required until plastic deformation ($W_{Rp0.2}$) was observed, indicating an overall reduced biomechanical stability in *Wnt1*$^{G177C/G177C}$ mice (Figure 36A). If these data were normalized for bone geometric properties obtained from µCT analysis, F_{max} was no longer different between *Wnt1*$^{+/+}$ and *Wnt1*$^{G177C/G177C}$ femora, suggesting that the failure only happened due to geometrical differences between the bones. Interestingly, however, when normalizing $W_{Rp0.2}$ for geometric properties obtained by µCT, there was still a significant reduction found in *Wnt1*$^{G177C/G177C}$ femora compared to wild-type controls, suggesting altered bone matrix quality (Figure 36B).

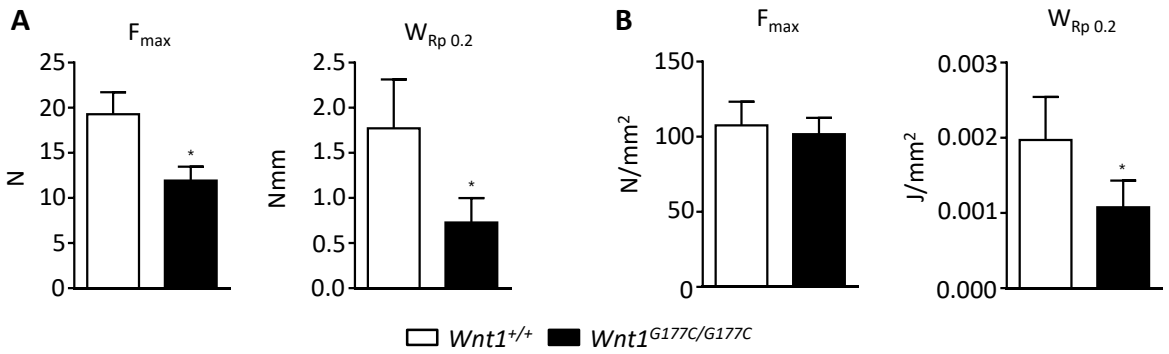

Figure 36: *Wnt1*$^{G177G/G177C}$ mice display reduced biomechanical stability. (A) Quantification of mechanical properties of femora from male *Wnt1*$^{+/+}$ and *Wnt1*$^{G177C/G177C}$ mice at 24 weeks of age measured by 3-point bending. F_{max}: Maximum force the bone can withstand; $W_{Rp\ 0.2}$: Work required until plastic deformation of the bone. **(B)** Quantification of parameters analyzed in A after normalization for structural differences. Data were analyzed by two-tailed Student´s t test. n≥3 mice per group; *p<0.05 vs. *Wnt1*$^{+/+}$ littermates.

Another parameter contributing to the mechanical quality of bone is the degree of mineralization. The degree of mineralization and the distribution throughout the cortical bone matrix of the tibia of 24 weeks old *Wnt1*$^{+/+}$ and *Wnt1*$^{G177C/G177C}$ mice was measured by quantitative back-scattered electron imaging (qBEI). This analysis revealed an overall shift towards lower mineralization in *Wnt1*$^{G177C/G177C}$ mice. (Figure 37A). Quantitative analysis of the weighted mean calcium concentration (Ca_{Mean}) further showed a reduction in *Wnt1*$^{G177C/G177C}$ mice compared to *Wnt1*$^{+/+}$ control mice (Figure 37B).

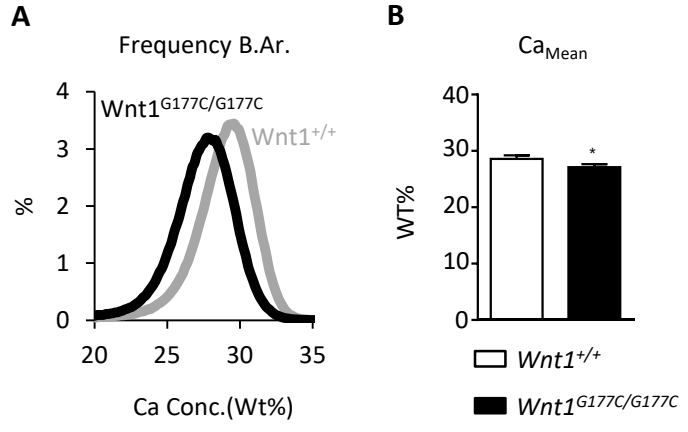

Figure 37: *Wnt1*$^{G177G/G177C}$ mice display lower mineralization. (A) Frequency distribution of calcium concentration in the central cortical tibia from male *Wnt1*$^{+/+}$ and *Wnt1*$^{G177C/G177C}$ mice at 24 weeks of age. **(B)** Quantification of the mean calcium content. Data were analyzed by two-tailed Student´s t test. n≥3 mice per group; *p<0.05 vs. *Wnt1*$^{+/+}$ littermates.

5.4.5 Osteoanabolic treatment of *Wnt1*$^{G177C/G177C}$ cultures and mice

Finding a potential treatment option for diseases like OI type XV is very important. Teriparatide (PTH(1-34)) is an osteoanabolic agent approved for osteoporosis treatment and fracture healing. To address the clinically relevant question, if the G177C mutation impairs the responsiveness of osteoblasts to the osteoanabolic effect of PTH(1-34), two different experiments were performed. The first experiment was carried out with cavarial osteoblasts cultured under osteogenic conditions. Here, the capacity of *Wnt1*$^{G177C/G177C}$ osteoblasts to form mineralized matrix was analyzed by alizarin red staining of these cultures. This revealed a significant reduction in mineralized matrix at day 10 and day 20 of osteogenic differentiation in *Wnt1*$^{G177C/G177C}$ compared to *Wnt1*$^{+/+}$ osteoblast cultures (Figure 38A). Consistently, qRT PCR expression analyses demonstrated significantly decreased expression levels of osteoblastogenesis markers like *Runx2* and *Col1a1* (Figure 38B). Cells cultured until day 20 of osteogenic differentiation were additionally treated with PTH(1-34) for 6 hours under serum-free conditions prior to RNA isolation. The qRT PCR expression analysis of these samples revealed a marked induction of PTH-responsive genes like *Cited1* and *Tnfsf11* both in *Wnt1*$^{+/+}$and *Wnt1*$^{G177C/G177C}$ cultures, indicating that the mutation did not impair the responsiveness of osteoblasts to PTH(1-34). Nevertheless, the overall expression of PTH-responsive genes was lower in *Wnt1*$^{G177C/G177C}$ than in *Wnt1*$^{+/+}$ cultures. This observation was consistent with the finding of a significantly decreased expression level of *Pth1r*, encoding the PTH receptor, in untreated cultures (Figure 38C).

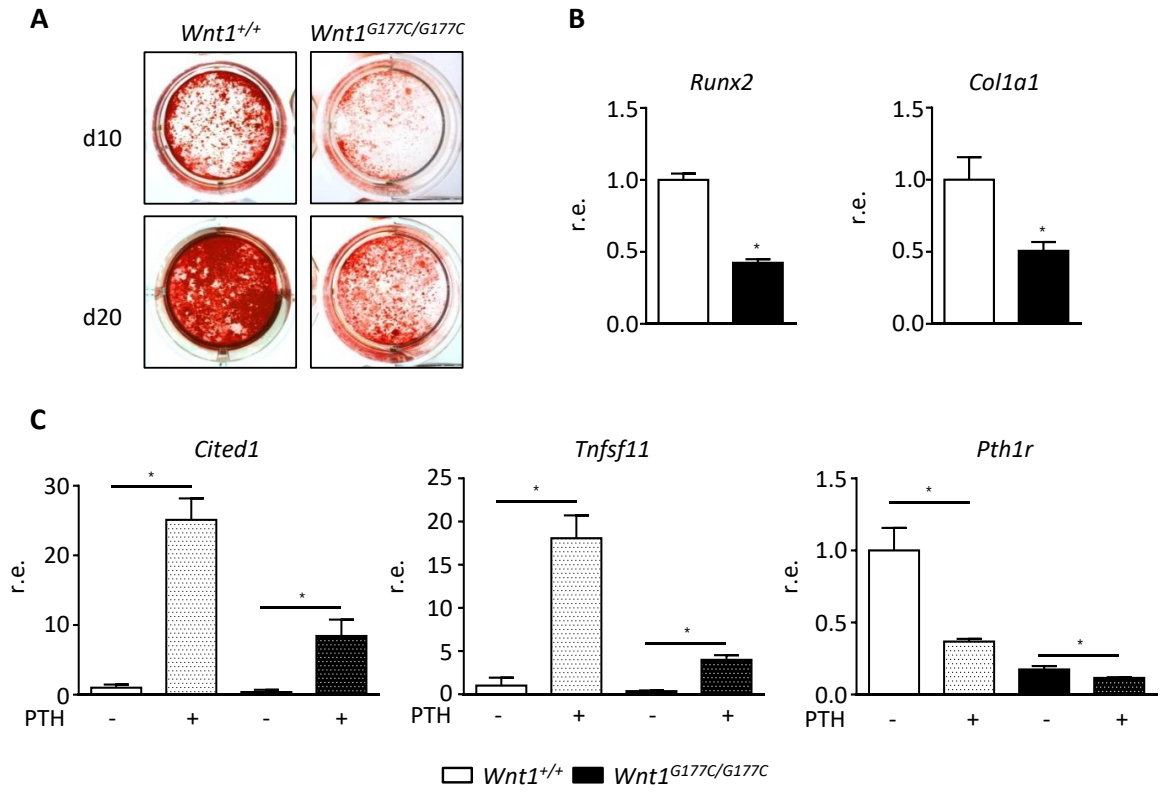

Figure 38: Cultured *Wnt1*$^{G177C/G177C}$ osteoblasts respond to PTH treatment. (A) Representative images of alizarin red stained primary calvarial osteoblasts isolated from *Wnt1*$^{+/+}$ and *Wnt1*$^{G177C/G177C}$ mice after 10 and 20 days (d) of osteogenic differentiation. **(B)** qRT PCR expression analysis of *Runx2* and *Col1a1* in *ex vivo* calvarial osteoblast cultures after 20 days of osteogenic differentiation. **(C)** qRT PCR expression analysis of PTH-responsive genes in *ex vivo* cultured calvarial osteoblasts after 20 days of osteogenic differentiation after 6 h of stimulation with 10 nM PTH(1-34) (+) compared to untreated controls (-).Data were analyzed by two-tailed Student´s t test. n=3 samples per group; *p<0.05 vs. *Wnt1*$^{+/+}$ littermates.

To examine, if the positive response to PTH(1-34) seen in cultured osteoblasts could also be confirmed *in vivo*, *Wnt1*$^{+/+}$ and *Wnt1*$^{G177C/G177C}$ mice were treated by daily intraperitoneal injection of PTH(1-34) from the age of 10 weeks until the age of 12 weeks. At this age, femora of these mice were analyzed by µCT, vertebrae were analyzed by structural and cellular histomorphometry, and serum PINP levels were measured by ELISA. The analysis of femora from 12 weeks old PTH(1-34)-treated *Wnt1*$^{+/+}$ and *Wnt1*$^{G177C/G177C}$ mice demonstrated a significant increase in osteoblast surface (Figure 39A) and serum levels of the bone formation biomarker PINP in treated *Wnt1*$^{+/+}$ and *Wnt1*$^{G177C/G177C}$ mice compared to untreated littermates (Figure 39B). Furthermore, treated *Wnt1*$^{G177C/G177C}$ mice displayed increased cortical thickness compared to untreated controls (Figure 39C).

In summary, these results indicate an increase in bone formation due to intermittent PTH(1-34) treatment, which further demonstrates that a mutational Wnt1 does not impair the responsiveness to this osteoanabolic drug *in vivo*. This suggests that individuals with OI type XV could profit from treatment with Teriparatide.

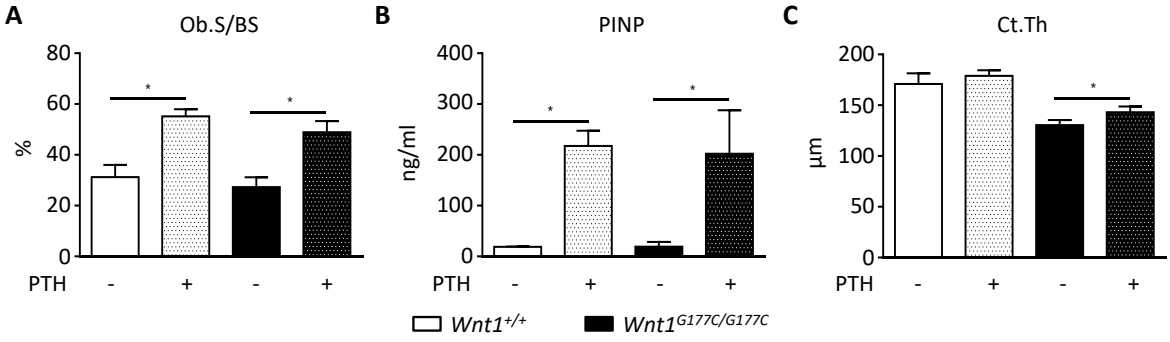

Figure 39: *Wnt1*$^{G177C/G177C}$ mice respond to PTH(1-34) treatment. (A) Quantification of Ob.S/BS in lumbar vertebral bodies of 12 weeks old female *Wnt1*$^{+/+}$ and *Wnt1*$^{G177C/G177C}$ mice after 2 weeks of daily injections of 80 µg/kg PTH(1-34) (+) compared to untreated controls (-). **(B)** Serum PINP levels of mice from A. **(C)** Quantification of Ct.Th of mice from A. Data were analyzed by two-tailed Student´s t test. n≥5 samples per group; *p<0.05 vs. control animals of the same genotype.

5.4.6 Genome-wide expression analysis of *Wnt1*$^{G177C/G177C}$ osteoblasts

To analyze whether the *Wnt1 G177C* mutation had an effect on other genes related to OI and thus causing a reduction in mechanical quality of the bone, Affymetrix Gene Chip hybridization was performed on pooled RNA samples obtained from cultured calvarial osteoblasts after 10 days of osteogenic differentiation. This array revealed that the expression of most of the 17 known OI-related genes was slightly reduced in *Wnt1*$^{G177C/G177C}$ osteoblasts showing a SLR lower than -1. However, the expression of *Ifitm5* showed the strongest reduction with a SLR lower than -4. Only the expression of *Mbtps2* and *Bmp1* were unchanged, and the expression of *Tmem38b* was slightly induced showing a SLR above +1 (Figure 40). These results provide a first possible molecular explanation for the observed phenotype and suggest that Ifitm5, an osteoblast-specific transmembrane protein, might act downstream of Wnt1. It further provides the basis for additional experiments to uncover the function of Wnt1 in bone quality regulation at the molecular level.

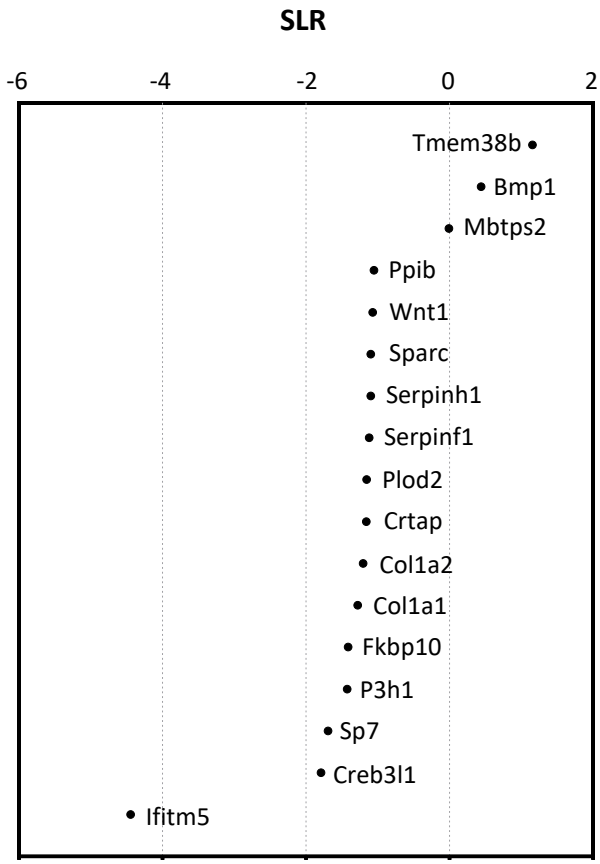

Figure 40: *Wnt1*$^{G177C/G177C}$ osteoblasts display reduced expression of most OI-related genes. Affymetrix Gene Chip hybridization showing the SLR of OI-related genes expressed in pooled RNA samples obtained from *Wnt1*$^{G177C/G177C}$ calvarial osteoblasts compared to wild-type littermate controls, both cultured for 10 days under osteogenic conditions.

6 Discussion

Although both the Notch and the Wnt signaling pathway play key roles in embryonic development, their role in bone metabolism is not fully clarified. The recent identification of mutations in either *NOTCH2* or *WNT1* in patients with early-onset osteoporosis highlighted the relevance for further investigations[83, 105]. The generation of mouse models carrying the above-mentioned specific mutations, found in humans, provided an ideal system to study underlying cellular mechanisms in the course of this thesis.

6.1 The Notch signaling pathway

The Notch signaling pathway is evolutionary conserved and plays a critical role during embryonic and postnatal development, especially in neuronal processes[115]. By controlling lateral inhibition, which allows one cell to undergo differentiation, while the neighboring cells are inhibited from adapting the same fate, this pathway is involved in cell fate determination, proliferation, differentiation, and apoptosis[116]. The 4 identified *Notch* genes encode single-pass transmembrane receptors of which the extracellular domain is responsible for ligand binding while the intracellular domain is required for transcriptional activation of Notch target genes. More specifically, the receptors (Notch1-4) can be bound by different canonical ligands such as Jagged1, Jagged2, Dll1, Dll3, or Dll4 expressed on a neighboring, signaling cell[69]. Upon binding of a ligand to a receptor on the signal-receiving cell, a proteolytic cleavage is faciliated within the juxtamembrane region by ADAM metalloproteases. This is followed by an additional proteolytic cleavage within the transmembrane domain mediated by a γ–secretase complex containing either presenilin-1 or presenilin-2 as a catalytic subunit. The second cleavage results in the release of the NICD from the plasma membrane. The NICD subsequently translocates into the nucleus of the cell, where it forms a protein complex with the transcription factor Epstein-Barr Virus Latency CBF1 (in mice termed RBP-Jκ) and its coactivator Mastermind-Like (Maml). This complex allows binding to DNA, hence, transcriptional activation of canonical Notch target genes like *Hes* and *Hey* transcription factors[70, 71]. Negative regulation of this signaling pathway is mediated by the C-terminal PEST-domain that is targeted for polyubiquitination and thus required for proteasomal degradation of the NICD[72, 73].

The identification of truncating mutations in *NOTCH2* that were associated with HCS has highlighted its importance in bone metabolism. HCS is described as a rare autosomal dominant disorder of the skeleton. It is characterized by osteoporosis, acro-osteolyses, short stature, coarse facies, and renal cysts[83-85]. To further investigate the role of Notch2 in the pathophysiology of bone turnover, a Notch2 HCS mouse line carrying the 6272delT mutation in the *Notch2* gene was generated by homologous recombination in the Department for Osteology and Biomechanics by Timur Yorgan in cooperation with the Transgenic Mouse Facility of the University Medical Center Hamburg-Eppendorf prior to this thesis. The initial analysis of this mouse line was expanded in the context of this thesis.

6.2 Characterization of *Notch$^{+/HCS}$* mice regarding pathologies found in HCS patients

As the value of a mouse model for a specific human disease increases with phenotypical accordance, *Notch2$^{+/HCS}$* mice were analyzed regarding patient pathologies. Inconsistent with the pathologies observed in human patients, generated *Notch2$^{+/HCS}$* mice did not develop acro-osteolyses. In patients, 84 % of all cases display this specific symptom[117], which emerges due to microdamages or inflammatory events[118, 119]. Experimental mice, however, might not be exposed to sufficient mechanical loading, abrasion, or pathogens that could promote the development of acro-osteolyses.

In contrast, the abnormal skull morphology found in HCS patients could partly be confirmed in 24 weeks old animals with a decrease in skull length, a reduced nasal length, and a decreased skull width. As the prevalence of this symptom is only reported in a subset of patients ranging from 9 to 67 %, depending on the specific type of characteristic[117], the partial presence of abnormalities in the mouse model was not surprising. Some patients further display a short stature, which could be confirmed in *Notch2$^{+/HCS}$* mice, when detecting shortened femur lengths, tibia lengths and vertebral body heights at most ages analyzed.

Apart from some limitations of the mouse model, further analyses of the skeleton of these mice demonstrated decreased trabecular bone mass in long bones and in vertebral bodies at all ages analyzed, correlating to the decreased BMD in HCS patients[83-85]. Importantly, also consistent with symptoms observed in previously published HCS patients[120, 121], *Notch2$^{+/HCS}$*

mice displayed an increase in bone formation and bone resorption, resulting in overall high bone turnover osteopenia. These observations further matched with observations found in one HCS patient analyzed at the Department for Osteology and Biomechanics (Figure 4).

In contrast, the very recently and first published mouse model of HCS harbouring a 6955C>T mutation in *Notch2* was reported to display osteopenia due to increased osteoclastogenesis potentially mediated by increased Rankl expression[122]. However in line with our model, this mouse model did not display acro-osteolyses either. Nevertheless, it has to be taken into consideration that these mice were only analyzed up to the age of 12 weeks, with the most severe phenotypical differences at the age of 4 weeks. Our own HCS mouse model, however, displayed the most severe phenotype in animals older than 12 weeks of age. Additionally, different mutations identified in HCS patients may result in subtly phenotypical differences, potentially due to divergent effects on signal duration, affinity, and degrading processes.

Overall the findings demonstrate the value of the *Notch2*$^{+/HCS}$ mice as a disease model for HCS with some minor limitations.

6.3 Analysis of molecular mechanisms leading to high bone turnover in *Notch2*$^{+/HCS}$ mice

Analyses of primary osteoblasts and osteoclasts of *Notch2*$^{+/HCS}$ mice revealed no cell-autonomous gain-of-function. However, the RNA of bone marrow cells cultured under osteoblastogenic conditions and treated or not with short-term administration of the ligand Dll1, enabled an unbiased approach, *i.e.* RNA sequencing. Using this technique, several genes could be identified with *Heyl* being the most strongly induced gene after the treatment with Dll1 in RNA obtained from *Notch2*$^{+/HCS}$ mice. Since *Heyl* is known to be a Notch signaling target gene[71, 123, 124], this finding confirms the prolonged Notch signal in *Notch2*$^{+/HCS}$ mice due to the absence of the PEST-domain. Importantly, a marked increase in the expression of pro-osteoclastogenic genes such as *Il6* and *Tnfs11*, encoding for IL-6 and Rankl, could be identified after the treatment with Dll1 in RNA obtained from *Notch2*$^{+/HCS}$ osteoblasts compared to wild-type controls. IL-6 is known to indirectly stimulate osteoclastogenesis by promoting the production of Rankl[125]. Moreover, Rankl is an established osteoblast-expressed stimulator of osteoclastogenesis[31]. An increased production of IL-6 could further be confirmed in conditioned cell culture medium of cultured

Notch2$^{+/HCS}$ osteoblasts compared to wild-type controls. Similarly, the concentration of IL-6 was increased in the serum of *Notch2*$^{+/HCS}$ animals. Also immunohistochemical analyses of bone marrow sections from *Notch2*$^{+/HCS}$ mice further revealed a higher number of IL-6 positive cells compared to wild-type controls.

Although Rankl concentrations were unchanged in *Notch2*$^{+/HCS}$ animals, the production of this molecule could still be increased, as Rankl is produced as a membrane-bound protein on osteoblasts that is cleaved into a soluble form by metalloproteases[126]. Together, these findings lead to the assumption, that the increased osteoclastogenic phenotype of *Notch2*$^{+/HCS}$ mice is secondary to enhanced expression of pro-osteoclastogenic genes like *Il6* and *Tnfsf11* by osteoblastic cells.

These findings are in agreement with a recently published study on a mouse model carrying an osteoblast-specific truncation of the *Notch2* gene, showing increased osteoblastogenesis[127] as well as the previously published mouse model carrying another HCS mutation leading to osteopenia due to increased osteoclastogenesis that is potentially mediated by increased Rankl expression[122]. Taken together, these observations support the hypothesis that increased osteoclastogenesis in HCS mice is caused by Notch signaling alterations in the osteoblast lineage.

To uncover a potential mechanism causing the osteoanabolic part of the *Notch2*$^{+/HCS}$ phenotype, wild-type and *Notch2*$^{+/HCS}$ mice were treated by weekly alendronate injection. This primarily anti-resorptive treatment is known to cause a secondary reduction of bone formation due to impaired release of pro-osteoblastogenic coupling factors by osteoclasts[111-113]. In our mouse model, alendronate treatment increased trabecular bone mass by reducing bone resorption. Most importantly, however, this treatment led to a significant decrease in osteoblast number and activity in wild-type and *Notch2*$^{+/HCS}$ mice. This finding suggests that increased osteoblastogenesis in *Notch2*$^{+/HCS}$ mice could be secondary to increased osteoclastogenesis, potentially explained by a higher production of osteoclast-derived coupling factors. Although the impact of this treatment could not be examined regarding to acro-osteolyses in this *Notch2*$^{+/HCS}$ mouse model, the resulting normalization of bone mass in *Notch2*$^{+/HCS}$ mice suggests that it could be a reasonable approach to prevent osteopenia and to decrease the risk of fractures in individual HCS patients. That anti-

resorptive therapy improves the HCS phenotype in humans has been published, showing increased BMD in HCS patients after bisphosphonate treatment[128, 129]. Other published treatment options performed on HCS patients include osteoanabolic treatment by Teriperatide[130] or the Rankl inhibitor Denosumab[131, 132]. Both Teriparatide and Denosumab treatments also resulted in increased BMD in HCS patients.

6.4 S1P and Wnt1 as potential coupling factors causing increased bone formation in *Notch2*$^{+/HCS}$ mice

The observed elevated bone formation in *Notch2*$^{+/HCS}$ mice potentially develops secondary to increased osteoclastogenesis. Therefore, the understanding of mechanisms coupling bone resorption and bone formation is very important. One coupling factor that is released by osteoclasts and stimulates bone formation is the signaling lipid S1P. More specifically, it has been shown that S1P is produced by osteoclasts and stimulates bone formation by binding to its receptor S1pr3 on osteoblasts[42, 44, 45]. Therefore, by mating *S1pr3*$^{-/-}$ and *Notch2*$^{+/HCS}$ mice, the signal transduction on osteoblasts and bone formation from osteoclast-released S1P was assumed to be impaired. However, investigations addressing this hypothesis could be neglected, since structural bone analysis of *Notch2*$^{+/HCS}$*; S1pr3*$^{-/-}$ mice showed that there was no correction of the HCS-specific phenotype.

A second potentially relevant coupling factor is Wnt1, which has been shown to be released by osteoclasts in response to TGF-β1[46]. Generally, Wnt signaling is an evolutionary conserved signaling pathway that is required for cell fate determination, proliferation, polarity and cell death, both during embryonic development and also throughout adult life[88]. WNT proteins represent a family of 19 different secreted glycoproteins that are required for the activation of their cell-surface receptors, thereby transducing and activating the transcription of WNT target genes[133].

The specific role of Wnt1 as a potential coupling factor has been analyzed in this thesis by utilizing mice with an osteoclast-specific inactivation of *Wnt1* (*Wnt1*$^{fl/fl;\ Lyz2\text{-}Cre}$). Since there was no skeletal phenotype observed in *Wnt1*$^{fl/fl;\ Lyz2\text{-}Cre}$ mice compared to littermate controls, it could be demonstrated that osteoclasts are not the main source of Wnt1 secretion promoting increased bone formation. In contrast, osteoblast-specific inactivation of Wnt1

resulted in a dramatic osteoporotic phenotype with skeletal fractures, which led us to investigate the role of Wnt1 in bone remodeling in greater detail.

6.5 The role of Wnt1 in bone remodeling

The recently published identification of WNT1 mutations causing EOOP and OI type XV has highlighted the impact of WNT1 on bone metabolism[105-108]. OI is a rare monogenetic disorder primarily affecting the quality of the bone matrix[61]. Whereas the majority of OI forms are related to defective collagen type I fibrils or altered posttranslational modifications of collagen type I, some more recently identified mutations, including the mutation of *WNT1*, are considered to represent a state of severely impaired osteoblast differentiation or function[59].

To investigate the role of Wnt1 in osteoblastogenesis, a mouse model carrying a previously identified G177C mutation of *Wnt1* causing OI type XV was generated[105]. Mice, homozygous for the G177C mutation, displayed a reduction of trabecular and cortical bone mass compared to littermate controls already present at the age of 4 weeks. Moreover, at 24 weeks of age, this osteopenic phenotype was still present, but most importantly, these mice additionally displayed multiple skeletal fractures. These observations confirmed the value of $Wnt1^{G177C/G177C}$ mice as a model of OI type XV. Remarkably however, other genetically modified mouse models with a much stronger reduction of trabecular and cortical bone mass did not display spontaneous fractures until the age of 24 weeks[53, 134]. Furthermore, mouse models with Wnt1 loss-of-function, *i.e*. $Wnt1^{sw/sw}$[109], $Wnt1^{fl/fl;\ Dmp1\text{-}Cre}$[110] and $Wnt1^{fl/fl;\ Runx2\text{-}Cre}$ (Luther *et al*., 2018, submitted), display a very strong reduction in trabecular and cortical bone mass, but the fracture rate of these mice was comparable to $Wnt1^{G177C/G177C}$ mice.

Of note, previous mouse models of *Wnt1*-deficiency have highlighted its potential role in brain development. More specifically, the $Wnt1^{sw/sw}$ mouse model was first described in 1967 displaying cerebellar defects and increased postnatal lethality. Only recently, the skeletal phenotype of these mice has been investigated in more detail[109]. Furthermore, a *Wnt1*-deficiency model was also described having severe defects of brain development, including the cerebellum[114]. Compared to $Wnt1^{sw/sw}$ mice and *Wnt1*-deficient mice, our $Wnt1^{G177C/G177C}$ mice did not exhibit any obvious brain abnormalities. Also in humans, this

specific G177C mutation was not reported to result in abnormal brain development and function, whereas other mutations associated with OI type XV were reported to cause brain abnormalities. Furthermore, the swaying mutation results in a truncated Wnt1, whereas the G177C mutation in the crystal structure of XWnt8 is predicted to result in impaired binding to its receptor, due to a destabilized core[105]. These structural differences may also lead to differential effects on brain development. However, the consistent absence of a brain phenotype in patients of OI type XV and *Wnt1*$^{G177C/G177C}$ mice further underlines the value of *Wnt1*$^{G177C/G177C}$ mice as a putative model of OI type XV.

Moreover, both *Wnt1*-deficient and *Wnt1*$^{sw/sw}$ mice displayed embryonic lethality, whereas this phenotype was not observed in *Wnt1*$^{G177C/G177C}$ mice. Instead, *Wnt1*$^{+/+}$, *Wnt1*$^{+/G177C}$, and *Wnt1*$^{G177C/G177C}$ mice were viable and the majority of mice survived until adulthood.

6.6 High skeletal fracture rate in *Wnt1*$^{G177C/G177C}$ mice

Since the high fracture rate in *Wnt1*$^{G177C/G177C}$ mice in the light of only moderate osteopenia suggested that Wnt1 primarily controls bone quality, a thorough mechanical analysis on femur fracture behavior was performed. This analysis clearly revealed altered bone matrix quality in comparison to littermate control mice when measuring the work required until plastic deformation, especially when normalizing the parameters for geometric properties of the bone. In addition, monitoring the degree of mineralization in cortical bone of the tibia of *Wnt1*$^{G177C/G177C}$ mice revealed an overall shift towards lower mineralization in *Wnt1*$^{G177C/G177C}$ mice compared to wild-type controls. This latter finding, in turn, might be the reason for the overall high fracture rate in *Wnt1*$^{G177C/G177C}$ mice. Moreover, cells isolated from *Wnt1*$^{G177C/G177C}$ mice demonstrated a reduced expression in most of the 17 known OI-related genes, especially Ifitm5, which is an osteoblast-specific transmembrane protein that might act downstream of Wnt1. Furthermore, a reduced mineralization capacity and a reduced expression of osteoblast marker genes including *Runx2* and *Col1a1* in cells of *Wnt1*$^{G177C/G177C}$ mice were found *in vitro*. Collectively, these *in vitro* findings support the hypothesis that reduced osteoblast function accounts for fragile bones in *Wnt1*$^{G177C/G177C}$ mice.

6.7 PTH treatment of *Wnt1*$^{G177C/G177C}$ mice

Currently, the vast majority of OI patients are treated by anti-resorptives, which was reported to reduce the fracture risk[135]. Furthermore, recent publications demonstrated that specific forms of OI could be treated by the inhibition of TGF-β signaling or Sost, although this has not been established for OI patients yet[136, 137]. Moreover, individuals with WNT1-dependent EOOP were reported to respond to osteoanabolic treatment with Teriparatide. Whether this osteoanabolic treatment is effective for patients of WNT1-dependent OI type XV, however, still remains to be established.

As the results of the G177C mouse model demonstrate its value as a disease model for OI type XV, it was of immediate clinical relevance to investigate the responsiveness of *Wnt1*$^{G177C/G177C}$ mice towards an osteoanabolic treatment. Since Wnt1 inactivation specifically affects osteoblast function, a treatment should attempt at restoring bone formation rather than impairing bone resorption. Furthermore, since the osteoanabolic influence of PTH treatment has already been reported to activate Wnt signaling in humans by reducing its inhibitor Sost[138, 139], it was important to address the question, if the Wnt^{G177C} mutation would interfere with the osteoanabolic influence of intermittent PTH(1-34) treatment. Therefore, it was a very important finding that both *in vitro* and *in vivo* PTH treatments of cells and mice carrying the G177C mutations were able to respond to PTH in the same way like wild-type cells and mice did. More specifically, PTH-responsive genes like *Cited1* and *Tnfs11* were clearly induced after treatment of PTH in both wild-type and *Wnt1*$^{G177C/G177C}$ cultures. Moreover, increased osteoblast indices and increased serum PINP levels in treated *Wnt1*$^{G177C/G177C}$ mice and controls confirmed an equal interference with the influence of PTH. Despite the relatively short duration of the treatment, there was a positive influence on the bone phenotype of *Wnt1*$^{G177C/G177C}$ mice, indicated by significantly increased cortical thickness in *Wnt1*$^{G177C/G177C}$ mice after PTH treatment. These findings together fully agree with the recently published response of patients with WNT1-dependent EOOP to Teriparatide[140].

7 Prospect

The results of this thesis demonstrate that the underlying mechanisms causing a low bone mass phenotype in *Notch2*$^{+/HCS}$ and *Wnt1*$^{G177C/G177C}$ mice are fundamentally different. While the mutation in *Notch2*$^{+/HCS}$ mice promote enhanced expression of pro-osteoclastogenic genes, thereby triggering a high bone turnover pathology, the mutation in *Wnt1*$^{G177C/G177C}$ mice affects bone formation and bone matrix quality. Furthermore, both models were utilized to demonstrate possible treatment options.

In case of the *Notch2*$^{+/HCS}$ mutation, future experiments should include more functional and molecular analyses. More specifically, as the expression of *Il6* as a pro-osteoclastogenic cytokine was elevated in *Notch2*$^{+/HCS}$ mice, it would be interesting to analyze a corresponding mouse deficiency model crossed into the *Notch2*$^{+/HCS}$ background. In fact, an *Il6*-deficiency model is already established at the UKE animal facility. This *in vivo* approach could eventually elucidate the important role of IL-6 downstream of Notch2. Additionally, the administration of the monoclonal antibody against Notch2, Tarexumab[141], could be used in *Notch2*$^{+/HCS}$ mice to examine whether this treatment corrects the osteopenic phenotype.

Regarding *Wnt1*$^{G177C/G177C}$ mice, future experiments should include deeper analysis of the bone matrix quality. Since a recent publication reported on osteocytes being the source of Wnt1 [110], the osteocyte morphology and the osteocyte canalicular network should be analyzed for alterations. Furthermore, analyzing bones of *Wnt1*$^{G177C/G177C}$ mice by Fourier-transform infrared spectroscopy (FTIR) could give information about the mineral to matrix and carbonate to phosphate ratios. Apart from bone quality analyses, also the behavior of *ex vivo* cultured primary bone cells from *Wnt1*$^{G177C/G177C}$ mice should be studied regarding proliferation, differentiation, activity, and putative downstream targets.

8 Material and methods

8.1 Material

8.1.1 Chemicals and substances

Name	Abbreviation	Manufacturer
(2E)-3-(4-Hydroxyphenyl)-prop-2-enoic acid	p-Coumaric acid	Sigma-Aldrich Corp. (St. Louis, US)
1,2-dihydroxyanthraquinon	Alizarinred S	Chroma GmbH & Co. KG (Münster, DE)
1,4-Dimethylbenzene	p-Xylene	Merck KGaA (Darmstadt, DE)
1α,25-Dihydroxyvitamin-D_3	Vitamin-D_3	Sigma-Aldrich Corp. (St. Louis, US)
3',3",5',5"-tetrabromophenol-sulfonphthalein	Brom-phenol blue	Carl Roth GmbH & Co. KG (Karlsruhe, DE)
4-(2-hydroxyethyl)-1-piperazineethanesulfonic acid	HEPES	Sigma-Aldrich Corp. (St. Louis, US)
5-Amino-2,3-dihydrophthalazine-1,4-dione	Luminol	Sigma-Aldrich Corp. (St. Louis, US)
Acetic acid		Sigma-Aldrich Corp. (St. Louis, US)
Acid fuchsin		Merck KGaA (Darmstadt, DE)
Agarose (SeaKem® LE)		Lonza Group AG (Basel, CH)
Ammonium hydroxide		Sigma-Aldrich Corp. (St. Louis, US)
Ammonium persulfate	APS	Sigma-Aldrich Corp. (St. Louis, US)
Benzoyl peroxide	BPO	Merck KGaA (Darmstadt, DE)
Carbon dioxide		TMG GmbH (Krefeld, DE)
Diethyl pyrocarbonate	DEPC	Sigma-Aldrich Corp. (St. Louis, US)
Dimethyl sulfoxide	DMSO	Carl Roth GmbH & Co. KG (Karlsruhe, DE)
Dithiothreitol	DTT	Sigma-Aldrich Corp. (St. Louis, US)
Ethanol	EtOH	Merck KGaA (Darmstadt, DE)
Ethylenediaminetetraacetic acid	EDTA	Merck KGaA (Darmstadt, DE)
Fast Red Violet LB Salt		Sigma-Aldrich Corp. (St. Louis, US)
Formaldehyde		Sigma-Aldrich Corp. (St. Louis, US)
Glycerol		Carl Roth GmbH & Co. KG (Karlsruhe, DE)
Glycin		Carl Roth GmbH & Co. KG (Karlsruhe, DE)
Hydrochloric acid	HCl	Sigma-Aldrich Corp. (St. Louis, US)
Hydrogen peroxide	H_2O_2	Merck KGaA (Darmstadt, DE)
Isopropyl alcohol		Carl Roth GmbH & Co. KG (Karlsruhe, DE)
L-Ascorbic acid	Asc	Sigma-Aldrich Corp. (St. Louis, US)
Magnesium chloride	$MgCl_2$	Merck KGaA (Darmstadt, DE)
Methanol	MeOH	Carl Roth GmbH & Co. KG (Karlsruhe, DE)
Methyl methacrylate	MMA	Merck KGaA (Darmstadt, DE)
Monoglycol butylether		Sigma-Aldrich Corp. (St. Louis, US)
N,N-Dimethyl formamide		Fluka Chemie GmbH (Buchs, CH)
N,N-Dimethyl-p-toluidine	DMT	Merck KGaA (Darmstadt, DE)
Nitric acid		Sigma-Aldrich Corp. (St. Louis, US)
Nitrogen		TMG GmbH (Krefeld, DE)
Nonyl phenoxypolyethoxyl-ethanol	NP40	Sigma-Aldrich Corp. (St. Louis, US)
Nonylphenyl-polyethylenglycol-acetate	NPG	Sigma-Aldrich Corp. (St. Louis, US)
Penicillin	Pen	Thermo Fisher Scientific Inc. (Waltham, US)
Picric acid		Sigma-Aldrich Corp. (St. Louis, US)
Polyoxyethylene (20) sorbitan monolaurate	Polysorbat 20	Carl Roth GmbH & Co. KG (Karlsruhe, DE)
Potassium chloride		Merck KGaA (Darmstadt, DE)
Potassium phosphate		Merck KGaA (Darmstadt, DE)
Prop-2-enamide	Acrylamide	Carl Roth GmbH & Co. KG (Karlsruhe, DE)
Silver nitrate		Merck KGaA (Darmstadt, DE)

Sodium acetate		Merck KGaA (Darmstadt, DE)
Sodium carbonate		Carl Roth GmbH & Co. KG (Karlsruhe, DE)
Sodium chloride	NaCl	Sigma-Aldrich Corp. (St. Louis, US)
Sodium deoxycholate		Sigma-Aldrich Corp. (St. Louis, US)
Sodium dodecyl sulfate	SDS	Carl Roth GmbH & Co. KG (Karlsruhe, DE)
Sodium hydrogen carbonate	$NaHCO_3$	Sigma-Aldrich Corp. (St. Louis, US)
Sodium hydroxide	NaOH	Avantor Performance Materials (Center Valley, US)
Sodium hypochloride		Carl Roth GmbH & Co. KG (Karlsruhe, DE)
Sodium phosphate		Sigma-Aldrich Corp. (St. Louis, US)
Sodium tartrate		Sigma-Aldrich Corp. (St. Louis, US)
Streptomycin	Strep	Thermo Fisher Scientific Inc. (Waltham, US)
Tetramethylethylenediamine	TEMED	Sigma-Aldrich Corp. (St. Louis, US)
Toluidin blue O		Sigma-Aldrich Corp. (St. Louis, US)
Tris(hydroxymethyl)amino-methane base	Tris/Base	Sigma-Aldrich Corp. (St. Louis, US)
Tris(hydroxymethyl)amino-methane hydrochloride	Tris/HCl	Sigma-Aldrich Corp. (St. Louis, US)
β-Mercapto ethanol		Sigma-Aldrich Corp. (St. Louis, US)

8.1.2 Buffer and staining solutions

Acrylate	0,33 % (w/v) 11 % (v/v)	Benzoyl peroxide Nonylphenyl-polyethylenglycol-acetate ad Methyl methacrylate (destabilized)
Alizarin Red staining solution	40 mM	Alizarinred S ad H_2O pH 4,2
Ascorbic acid (stock solution)	10 mg/mL	L-Ascorbic acid ad H_2O
Blocking buffer (Western Blot)	5 % (w/v)	BSA ad TBST
Calcein injection solution	150 mM 238 mM 16 mM	NaCl $NaHCO_3$ Calcein ad H_2O pH 7,4
Collecting buffer (Western Blot)	1,5 M 0,4 % (w/v)	Tris/HCl SDS ad H_2O pH 6,8
DEPC-H2O	0,2 % (v/v)	DEPC ad H_2O
ECL solution	0,1 M 0,0092 % (v/v) 2,47 mM 396 µM	Tris/Base H_2O_2 Luminol p-Coumaric acid ad H_2O pH 8,5
Infiltration Solution I	0,33 % (w/v)	Benzoyl peroxide ad Methyl methacrylate (destabilized)
Infiltration Solution II	0,33 % (w/v) 11 % (v/v)	Benzoyl peroxide Nonylphenyl-polyethylenglycol-acetate ad Methyl methacrylate (destabilized)
M-CSF (stock solution)	10 µg/mL	M-CSF ad H_2O
Proteinase K (stock solution)	1 % (w/v)	Proteinase-K ad H_2O
Rankl (stock solution)	10 µg/mL	msRANKL ad H_2O
RIPA Buffer	1 % (v/v) 1 % (w/v) 0,1 % (w/v) 150 mM 2 mM 10 mM	NP-40 Sodium deoxycholate SDS NaCl EDTA Sodium phosphate ad H_2O pH 7,4
Running buffer (10x) (Western Blot)	250 mM 1,92 M	Tris/Base Glycin

	1 % (w/v)	SDS ad H_2O
Sample buffer (4x) (Western Blot)	500 mM 4 % (w/v) 40 % (v/v) 40 mM 1 Spatula tip	Tris/HCl SDS Glycerol DTT Brom phenol blue ad H_2O pH 6,8
Sectioning solution	0,1 % (v/v)	Polysorbat 20 ad H_2O
Seperation buffer (Western Blot)	1,5 M 0,4 % (w/v)	Tris/HCl SDS ad H_2O pH 8,8
Sodaformol solution	473 mM 24,8 % (v/v)	Sodium carbonate 37 % Formaldehyde ad H_2O
Stretching solution	80 % (v/v) 1 Drop/L	Isopropyl alcohol Monoglycol butylether ad H_2O
TAE buffer (50x)	2 M 50 mM	Tris/HCl EDTA ad H_2O pH 7,8
Tail Biopsy Lysis Buffer	100 mM 50 mM 100 mM 1 % (w/v)	EDTA Tris Base NaCl SDS ad H_2O pH 8,0
TBS buffer (10x)	500 mM 1,5 M	Tris/HCl NaCl ad H_2O pH 7,4
TBST buffer	0,1 % (v/v)	Polysorbat 20 ad TBS buffer
TE buffer	10 mM 1 mM	Tris Base EDTA ad H_2O pH 8,0
Toluidinblue staining solution	32,7 mM	Toluidin blue O ad H_2O pH 4,5
Transfer buffer (Western Blot)	25 mM 192 mM 20 % (v/v)	Tris/HCl Glycin Methanol ad H_2O pH 8,3
TRAP buffer	40 mM 10 mM	Sodium acetate Sodium tartrate ad H_2O pH 5
TRAP substrate solution	10 mg 1000 µl 60 mg	Naphtol AS-MX Phosphate Dimethyl formamide Fast Red Violet LB Salt ad 100 ml Trap buffer
Van Gieson staining solution	4,27 mM 10 % (v/v) 0,5 % (v/v)	Acid fuchsin Glycerol 65 % Nitric acid ad saturated Picric acid
Vitamin D3 (stock solution)	10 µM	Vitamin-D_3 ad EtOH
Von Kossa staining solution	194 mM	Silver nitrate ad H_2O
β-Glycerophosphate (stock solution)	2 M	β-Glycerophosphate ad H_2O

8.1.3 Cell culture media

Digestion medium	100 mg 200 mg 100 ml	Collagenase Ia Dispase II Minimal medium
Minimal medium	32,5 g/L 2,2 g/L	α-MEM Powder $NaHCO_3$ ad H_2O pH 7,4
Osteoblastic differentiation medium	50 µg/mL 10 mM	Ascorbic acid β-Glycerophosphate ad Osteoblastic medium
Osteoblastic medium	10 % (v/v) 100 U/mL	FCS (Obl) Penicillin/Streptomycin ad Minimal medium
Osteoclastic differentiation medium	10 nM	VitaminD_3

	20 ng/mL 40 ng/mL	MCSF msRANKL ad Osteoclastic medium
Osteoclastic medium	10 % (v/v) 100 U/mL	FCS (Ocl) Penicillin/Streptomycin ad Minimal medium

8.1.4 Ready to use solutions and substances

Name	Type	Manufacturer
30 % Acrylamide solution	Rotiphorese® Gel 30	Carl Roth GmbH & Co. KG (Karlsruhe, DE)
Alendronate		Sigma-Aldrich Corp. (St. Louis, US)
Bradford solution	Bio-Rad Protein Assay	Bio-Rad Laboratories, Inc. (Hercules, US)
BSA stock solution	Albumin Standard 2 mg/mL	Thermo Fisher Scientific Inc. (Waltham, US)
Calcein		Sigma-Aldrich Corp. (St. Louis, US)
DAB substrate	DAB	DakoCytomation (Glostrup, DK)
Developing solution	Citroline 2000	Adefo-Chemie GmbH (Dietzenbach, DE)
DNA-Ladder	GeneRuler 1 kb Plus DNA Ladder	Thermo Fisher Scientific Inc. (Waltham, US)
dNTP-Mix	dNTP Mix, 10 mM	Thermo Fisher Scientific Inc. (Waltham, US)
Ethanol	Ethanol	Walter CMP GmbH (Hamburg, DE)
Fast Blue RR Salt		Sigma-Aldrich Corp. (St. Louis, US)
Fetal Bovine Serum (Obl)	FBS (Hyclone, RYL35914)	Thermo Fisher Scientific Inc. (Waltham, US)
Fetal Bovine Serum (Ocl)	FBS (Gibco, 41G8512K)	Thermo Fisher Scientific Inc. (Waltham, US)
Fixation solution	Adefofix	Adefo-Chemie GmbH (Dietzenbach, DE)
Fixation solution	Formafix 3,5 %	Grimm med. Logistic GmbH (Turgelow, DE)
Hematoxylin		Merck KGaA (Darmstadt, DE)
Hydrogen peroxide (30 % solution)		Merck KGaA (Darmstadt, DE)
Mounting solution	DPX Mounting Solution	Sigma-Aldrich Corp. (St. Louis, US)
Mounting solution (brain)	Fluoromount	Merck KGaA (Darmstadt, DE)
Naphtol AS-MX Phosphate		Sigma-Aldrich Corp. (St. Louis, US)
PBS	GIBCO® Dulbecco´s Phosphate-Buffered Saline	Thermo Fisher Scientific Inc. (Waltham, US)
PCR-Buffer	10x DreamTaq Green Buffer	Thermo Fisher Scientific Inc. (Waltham, US)
Penecillin/Streptomycin Mix	Penecillin-Streptomycin (10000 U/ mL)	Thermo Fisher Scientific Inc. (Waltham, US)
Pepsin	#S3002	DakoCytomation (Glostrup, DK)
Phenol Chloroform Isoamylalcohol		Carl Roth GmbH & Co. KG (Karlsruhe, DE)
Phosphatase-Inhibitor	PhosSTOP	Roche Applied Science AG (Penzberg, DE)
Protease-Inhibitor	cOmplete Protease Inhibitor	Roche Applied Science AG (Penzberg, DE)
Protein Ladder	Prosieve™ QuadColor™ Protein Marker	Lonza Group AG (Basel, CH)
RNA Isolation solution	peqGOLD Trifast™	Peqlab Biotechnologie GmbH (Erlangen, DE)
Skim milk powder	Milk powder blotting grade	Carl Roth GmbH & Co. KG (Karlsruhe, DE)
TaqMan Mastermix	TaqMan® Gene Expression Master Mix	Thermo Fisher Scientific Inc. (Waltham, US)
α-MEM cell culture medium	Minimum Essential Medium Eagle Alpha Modification	Sigma-Aldrich Corp. (St. Louis, US)
β-Glycerophosphate	β -Gly	Sigma-Aldrich Corp. (St. Louis, US)

8.1.5 Oligonucleotides

Primers for Genotyping were obtained from Eurofins Genomics GmbH (Ebersberg, DE) and dissolved in a concentration of 200 µM in H_2O.

8.1.5.1 Genotyping

Mouse	Primer Name	5'->3' Sequence
LysM Cre	LysM-Cre KI LysM-Cre WT	CCCAGAAATGCCAGATTACG TTACAGTCGGCCAGGCTGAC
Notch2 HCS	Notch2 HCS F Notch2 HCS R2	CCCTTGGCACTTCGTGTTGA GGCCGCTTCATAACTTCCCT
Runx2 Cre	Cbfa_24 Cbfa_25 Cbfa_30	CCAGGAAGACTGCAAGAAGG TGGCTTGCAGGTACAGGA GGAGCTGCCGAGTCAATAAC
S1pr3 KO	S1pr3 WT F S1pr3 WT R S1pr3 KO F S1pr3 KO R	TGGTGTGCGGCTGTCTAGTCAA CACAGCAAGCAGACCTCCAGA ATCGATACCGTCGATCGACCT CACAGCAAGCAGACCTCCAGA
Wnt1 floxed	Wnt1 5' arm Wnt1 3' arm	CTGCCCAGCTGGGTTTCTACTACG ACCAGCTGCAGACTCTTGGAATCCG
Wnt1 G177C	Wnt1 G177C F Wnt1 G177C R	GTACCTGGGAAGCTGATCTC TAGTCGCAGGTGCAGGACTC
Wnt1 Runx2/Lyz2 Recombination	Wnt1 rec F Wnt1 rec R	AGTGAGCTAGTACGGGGTCC- AGGACCATGAACTGATGGCG

8.1.5.2 TaqMan qRT PCR

Gene	TaqMan®-Probe
Abca8a	Mm00462440_m1
Alpl	Mm00475834_m1
Bglap	Mm03413826_mH
Cited1	Mm01235642_g1
Col1a1	Mm00801666_g1
Fmo2	Mm00490158_m1
Gapdh	4308313
HeyL	Mm0051655_m1
Ibsp	Mm00492555_m1
Il6	Mm00446190_m1
Mmp9	Mm00442991_m1
Ocstamp	Mm00512445_m1
Pth1r	Mm00441046_m1
Runx2	Mm00501580_m1
Tnfsf11	Mm00441906_m1

8.1.5.3 Sequencing

Name	5'->3' Sequence
HCS Seq F	TCAATTGACCGCGGAGCAG
HCS Seq R	TGTGGCATCGGAGACATACG
Wnt1 G177C Seq F	CAGCGTTCATCTTCGCAATC
Wnt1 G177C Seq R	GCCTGCTAATCTCTTCTG

8.1.6 Antibodies

8.1.6.1 Primary antibodies

Target	Host	Product number	Manufacturer
Notch2-PEST	Rabbit	#5732	Cell Signaling Technology Inc. (Danvers, US)
β-actin	Rabbit	#4967	Cell Signaling Technology Inc. (Danvers, US)
IL-6	Rabbit	bs-0782R	BiossInc. (Woburn, US)
Cux1	Rabbit	Cat# ABE217	Merck KGaA (Darmstadt, DE)
DCX	Rabbit	Cat#326003	Synaptic Systems GmbH (Göttingen, DE)

8.1.6.2 Secondary antibodies

Target	Host	Product number	Manufacturer
Goat anti Rabbit Immunoglobulins/HRP	Goat	#P0448	Dako/Agilent Technologies Inc. (Santa Clara, US)

8.1.7 Enzymes and proteins

Name	Manufacturer
Dll1 Fc chimera	R&D Systems Inc.
Bovine Serum Albumin	Sigma-Aldrich Corp. (St. Louis, US)
M-CSF	Peprotech (Rocky Hill, US)
msRankl	Peprotech (Rocky Hill, US)
Proteinase K, recombinant PCR Grade	Roche Applied Science AG (Penzberg, DE)
Collagenase Ia from *C.histolyticum*	Sigma-Aldrich Corp. (St. Louis, US)
Dispase II	Roche Applied Science AG (Penzberg, DE)
DNA Dreamtaq Polymerase	Thermo Fisher Scientific Inc. (Waltham, US)
hPTH	Bachem Inc.(Bubendorf, CH)

8.1.8 Kits and assays

Name	Type	Manufacturer
IL-6 ELISA	M6000B	R&D Systems Inc. (Minneapolis, US)
DNA Isolation Kit	Phire animal tissue kit	Thermo Fisher Scientific Inc. (Waltham, US)
cDNA synthesis kit	Verso cDNA Synthesis Kit	Thermo Fisher Scientific Inc. (Waltham, US)
Crosslaps ELISA	RatLaps™ EIA	Immunodiagnostic Systems Ltd. (Boldon, UK)
PINP ELISA	SEA957MU	Cloud-Clone Corp. (Houston, US)
RNA Isolation Kit	Nucleospin® RNA II	Macherey-Nagel GmbH & Co. KG (Düren, DE)
PCR Cleanup Kit	Nucleospin® Gel & PCR Cleanup	Macherey-Nagel GmbH & Co. KG (Düren, DE)

8.1.9 Consumables

Name	Manufacturer
1.5/ 2 mL Reaction tubes	Eppendorf AG (Hamburg, DE)
15/ 50 mL Tube	Greiner Bio-One International AG (Kremsmünster, AT)
Abrasive paper	Hermes Schleifmittel GmbH & Co. KG (Hamburg, DE)
Adhesive PCR plate foil	Thermo Fisher Scientific Inc. (Waltham, US)
Bottle Top Filter	Thermo Fisher Scientific Inc. (Waltham, US)
Cell Culture Plates	Becton, Dickinson and Co. (Franklin Lakes, US)
Cell Scraper	Sarstedt AG & Co. (Nümbrecht, DE)
Cell Strainer 70 µm	Becton, Dickinson and Co. (Franklin Lakes, US)
Cover slips	Carl Roth GmbH & Co. KG (Karlsruhe, DE)
Embedding cassettes	Carl Roth GmbH & Co. KG (Karlsruhe, DE)
Filter Tip 10-1000 µl	Sarstedt AG & Co. (Nümbrecht, DE)
GeneChip™ Mouse Genome 430 2.0 Array	Thermo Fisher Scientific Inc. (Waltham, US)
Glass vials rolled rims	Carl Roth GmbH & Co. KG (Karlsruhe, DE)
Microscope slide	Glaswarenfabrik Karl Hecht GmbH & Co. KG (Sondheim, DE)
Microtest plates 96-well	Sarstedt AG & Co. (Nümbrecht, DE)
Microtome blade	Leica Biosystems Nussloch GmbH (Nussloch, DE)
Optical 96-well plate	Thermo Fisher Scientific Inc. (Waltham, US)
Pasteur pipettes	VWR International, LLC (Radnor, US)
PCR reaction tubes	Biozym Scientific GmbH (Hessisch Oldendorf, DE)
Pipette Tips	Sarstedt AG & Co. (Nümbrecht, DE)
PVDF Membrane	GE Healthcare Ltd. (Little Chalfont, UK)
Scalpel blade	C. Bruno Bayha GmbH (Tuttlingen, DE)
Serological Pipettes	Becton, Dickinson and Co. (Franklin Lakes, US)
UV Cuvettes	Eppendorf AG (Hamburg, DE)
X-ray films	Agfa-Gevaert N.V. (Mortsel, BE)

8.1.10 Technical devices

Technical Device	Model	Manufacturer
Acrylate microtome	Reichert Jung Mod. 1140/Autocut	Cambridge Instruments Co. Ltd. (St. Neots, UK)
Affymetrix Gene Chip® Scanner	7G 3000	Thermo Fisher Scientific Inc. (Waltham, US)
Autoklave	5050ELC	Tuttnauer Europe B.V. (Breda, NL)
Autotechnicon	2050	Bavimed Laborgerate GmbH (Birkenau, DE)
BSE Detector	Type 202	K.E. Developments Ltd. (Cambridge, UK)
Camera	EOS 10D	Canon K.K. (Tokio, JP)
Centrifuge	5430R	Eppendorf AG (Hamburg, DE)
Centrifuge	5415D	Eppendorf AG (Hamburg, DE)
Centrifuge	GS-6	Beckman Coulter, Inc. (Brea, US)
Electrophoresis system	Sub-Cell	Bio-Rad Laboratories, Inc. (Hercules, US)
Electrophoresis system	SDS/PAGE Mini Protean	Bio-Rad Laboratories, Inc. (Hercules, US)
Gene Chip® Fluidics Station	450	Thermo Fisher Scientific Inc. (Waltham, US)
Gene Chip® Hybridization Oven	640	Thermo Fisher Scientific Inc. (Waltham, US)
Grinding machine	Exakt-Apparatebau D-2000	EXAKT Apparatebau GmbH & Co. KG (Norderstedt; DE)
Grinding machine	Phoenix Alpha	Buehler Inc. (Lake Bluff, US)
Ice machine	FM-120DE	Hoshizaki Denki K.K. (Toyoake, JP)
Incubator	BBD 6220	Heraeus Holding GmbH (Hanau, DE)

Incubator	B 6200	Heraeus Holding GmbH (Hanau, DE)
Keyence Fluorescence Microscope	BZ-9000	Keyence Corp. (Osaka, JP)
Light Table	1634	Hama GmbH & Co KG (Monheim, DE)
Magnetic stirrer	RCT Basic	IKAR-Werke GmbH & CO. KG (Staufen, DE)
Micropipette	Research Plus	Eppendorf AG (Hamburg, DE)
Micropipette	Research	Eppendorf AG (Hamburg, DE)
Microplate reader	Versamax	Molecular Devices, LLC (Sunnyvale, US)
Microscope	AxioskopA1	Carl Zeiss AG (Oberkochen, DE)
Microscope	Axioskop HBO50/AC	Carl Zeiss AG (Oberkochen, DE)
Microscope camera	Axiocam	Carl Zeiss AG (Oberkochen, DE)
Mikroskope camera	QI Cam Fast 1394	Qimaging Corporation (Surray, Ca)
Mini Trans-Blot	Mini Trans Blot® Electrophoretic Transfer Cell	Bio-Rad Laboratories, Inc. (Hercules, US)
Paraffin microtome	Reichert-Jung Mod. Hn40	Cambridge Instruments Co. Ltd. (St. Neots, UK)
PCR-System	Mastercycler pro S	Eppendorf AG (Hamburg, DE)
PCR-System	Mastercycler epgradient S	Eppendorf AG (Hamburg, DE)
pH meter	Hanna Instruments HI 2211	Hanna Instruments Deutschland GmbH (Vöhringen, DE)
Pipette controller	Pipetboy acu	INTEGRA Biosciences AG (Zizers, CH)
Power supply	200/2.0	Bio-Rad Laboratories, Inc. (Hercules, US)
Power supply	Powerpac HC	Bio-Rad Laboratories, Inc. (Hercules, US)
Real-Time PCR system	StepOnePlus	Applied Biosystems, Inc. (Foster City, US)
Safety cabinett	S1200	BDK Luft- und Reinraumtechnik GmbH (Sonnenbuhl, DE)
Safety cabinett	HS12	Heraeus Holding GmbH (Hanau, DE)
Safety cabinett	MSC Advantage	Thermo Fisher Scientific Inc. (Waltham, US)
Scale	TE2101	Sartorius AG (Göttingen, DE)
Scale	440-33	Kern & Sohn GmbH (Balingen, DE)
Scanner	Scanjet G4050	Hewlett-Packard Company, L.P. (Palo Alto, US)
Scanning electron microscope	LEO 435 VP	Leo Electron Microscopy Ltd. (Cambridge, UK)
Shaker	Innova 4000	New Brunswick Scientific Co., Inc. (Enfield, US)
Shaker	KS260 Basic	IKAR-Werke GmbH & CO. KG (Staufen, DE)
Shaker	Duomax 1030	Heidolph Instruments GmbH & Co.KG (Schwabach, DE)
Special accuracy scale	CPA224S	Sartorius AG (Göttingen, DE)
Spectrophotometer	Ultrospec 2100 pro	Biochrom Ltd. (Cambridge, UK)
Spectrophotometer	Nanodrop ND1000	Thermo Fisher Scientific Inc. (Waltham, US)
Tank Blotter	Mini-Trans Blot	Bio-Rad Laboratories, Inc. (Hercules, US)
Tape Station	TapeStation 2200	Agilent Technologies Inc.
Thermoblock	Thermostat Plus	Eppendorf AG (Hamburg, DE)
Thermoblock	Thermomixer Comfort	Eppendorf AG (Hamburg, DE)
Universal testing machine	Z2.5/TN1S	Zwick Roell (Ulm, DE)
UV Light Table	Universal Hood 75S	Bio-Rad Laboratories, Inc. (Hercules, US)
Vortex mixer	Certomat MV	B.Braun Biotechnologie International GmbH (Melsungen, DE)
Water bath	1012	GFL Gesellschaft fur Labortechnik mbH (Burgwedel, DE)
X-ray apparatus	Faxitron Xray Sterile	Faxitron Xray Corp. (Tucson, US)
X-ray Film Processor	Optimax 1170-1-0000	Protec GmbH & Co. KG (Oberstenfeld, DE)
X-ray microtomograph	µCT 40	Scanco Medical AG (Brüttisellen, CH)

8.1.11 Software

Program	Version	Manufacturer
Adobe Photoshop CS4	11.0	Adobe Systems Incorporated (San José, US)
BioEdit	7.2.5.0	Ibis Biosciences (Carlsbad, US)
Bioquant Osteo	7.00.10	BIOQUANT Image Analysis Corp. (Nashville, US)
ImageJ	1.46p	[142]
MicroCT Software Suite	4.05	Scanco Medical AG (Brüttisellen, CH)
MS Office 2010	14.0	Microsoft Corp. (Redmond, US)
Osteomeasure	3.2.1.1	Osteometrics, Inc. (Decatur, US)
Prism	6.01	GraphPad Software, Inc. (La Jolla, US)
Quantity One	4.2.1	Bio-Rad Laboratories, Inc. (Hercules, US)
Softmax Pro	3.1.2	Molecular Devices, LLC (Sunnyvale, US)
StepOneTM Software	2.2.2	Applied Biosystems, Inc. (Foster City, US)
Transcriptomics Analysis Console (TAC)	4.0.1	Thermo Fisher Scientific Inc. (Waltham, US)

8.2 Methods

8.2.1 Molecular biological methods

8.2.1.1 Genomic DNA isolation

DNA was isolated for genotyping from tail biopsies of neonatal mice. The isolation was performed using the Phire animal tissue kit according to the manufacturer's instructions.

A second method to isolate DNA from tail biopsies was an extraction by phenol and chloroform. To digest the biopsy, 400 µl of Tail Biopsy Lysis Buffer together with 50 µl of Proteinase K was added and the solution was incubated for at least 2 hours at 55 °C. Subsequently 450 µl of ready for use Phenol/Chloroform was added and strongly mixed. After 10 minutes of centrifugation at 13000 rpm, two distinct phases were formed and 400 µl of the upper aqueously phase containing the nucleic acids was transferred into a new reaction tube and mixed with 400 µl isopropyl alcohol. The solution was thoroughly mixed and centrifuged under the same conditions as the previous time. The supernatant was decanted while the formed pellet was washed by adding 400 µl of 70 % ethanol and centrifuged for 5 minutes at 13000 rpm. After decanting the supernatant and after evaporation of the remaining ethanol, the pellet was resuspended in 50 µl TE buffer.

8.2.1.2 Polymerase chain reaction

Polymerase chain reaction (PCR) was used to amplify genomic DNA that was obtained during genomic DNA isolation to genotype mice. A selective amplification of a particular DNA sequence provided details on the presence of a specific mutation. Primer sequences that were used in this thesis are listed 8.1.5.1. PCR reaction mixtures as well as appropriate reaction programs are listed below. For the amplification of DNA, DreamTaq Polymerase was used. The analysis of the generated DNA target was done by agarose gel electrophoresis (1.5 %). The visualization of DNA in the gel was performed by ethidiumbromide (500 ng/µl).

Mouse line		Notch2 HCS	S1pr3 WT/KO	Wnt1 floxed	Wnt1 Rec
Reaction mixture (µl)	Water	9.7	9.2	8.2	9.2
	10x Buffer	2	2	2	2
	DMSO	0.5	0.5	2	0.5
	dNTPs	0.5	1	0.5	1
	Primer1	3	3	3	3
	Primer2	3	3	3	3
	Primer3	0	0	0	0
	Polymerase	0.3	0.3	0.3	0.3
	Genomic DNA	1	1	1	1
	Total volume	20	20	20	20
	Expected product	WT: 403 bp KI: 441 bp	WT: 300 bp KO: 200 bp	WT: 696 bp fl: >696 bp	No rec: no band Rec: 368 bp
Reaction program	Initialization	94 °C 4 min	94 °C 4 min	94 °C 4 min	94 °C 4 min
	Denaturation	94 °C 30 s	94 °C 30 s	94 °C 30 s	94 °C 30 s
	Annealing	58 °C 40 s	58 °C 30 s	58 °C 30 s	53 °C 30 s
	Elongation	72 °C 1 min	72 °C 1 min	72 °C 1 min	72 °C 1 min
	Final Elongation	72 °C 10 min	72 °C 10 min	72 °C 10 min	72 °C 10 min
	Cycles	40	40	40	40

Mouse line		Runx2 Cre	Lyz2-Cre WT	Lyz2-Cre KO	Wnt1G177C
Reaction mixture (µl)	Water	8.5	12.5	12.5	9.2
	10x Buffer	2.5	2.5	2.5	2
	DMSO	0.25	0.25	0.25	0.5
	dNTPs	0.5	0.5	0.5	1
	Primer1	4	4	4	3
	Primer2	4	4	4	3
	Primer3	4	0	0	0
	Polymerase	0.25	0.25	0.25	0.3
	Genomic DNA	1	1	1	1
	Total volume	25	25	25	20
	Expected product	Cre-: 780 bp Cre+: 600+780 bp	Cre-: 350 bp Cre+: 700 bp	Cre-: 350 bp Cre+: 700 bp	WT: 404 bp KI: 503 bp
Reaction program	Initialization	94 °C 4 min	94 °C 4 min	94 °C 4 min	94 °C 4 min
	Denaturation	94 °C 30 s	94 °C 30 s	94 °C 30 s	94 °C 30 s
	Annealing	59 °C 30 s	63 °C 30 s	55 °C 30 s	58 °C 30 s
	Elongation	72 °C 1 min	72 °C 45 s	72 °C 45 s	72 °C 1 min
	Final Elongation	72 °C 10 min	72 °C 10 min	72 °C 10 min	72 °C 10 min
	Cycles	40	40	40	40

8.2.1.3 DNA-sequencing

DNA sequencing was performed by Seqlab (Seqlab Sequence Laboratories GmbH, Göttingen, Germany) with the method of Sanger to analyze or confirm genotypes[143]. To obtain amplified DNA sequences, a PCR was performed using specific sequencing primers that are listed in 8.1.5.3. DNA of appropriate PCR products was isolated from the agarose gel by the PCR Cleanup Kit. The reaction mixture is shown below. Chromatograms were analyzed by Bioedit software.

4.5 mM	Tris, pH 8.5
30 pmol	Sequencing primer
22.5 ng/100 bp	DNA from PCR product
ad 15 µl	dd H_2O

8.2.1.4 RNA isolation

RNA was isolated to analyze the expression of particular genes. To isolate RNA from cultivated cells, the RNA Isolation Kit NucleospinRNA II was used according to the manufacturer's instructions. Different from the manufacturer's instructions the RNA was eluted in 50 µl dd H_2O and stored at -80 °C.

The concentration and quality of RNA were measured using a NanoDrop and the TapeStation instrument.

8.2.1.5 cDNA synthesis

To analyze gene expression of tissues or cells, isolated RNA was reversed-transcribed into cDNA using Verso cDNA Synthesis Kit according to the manufacturer´s instructions. The cDNA was stored at -20 °C.

8.2.1.6 Quantitative real time PCR

A quantitative Real Time PCR (qRT PCR) enables the detection and quantification of PCR products during each cycle of PCR process by measuring fluorescence signals. In this thesis the TaqMan™ system was used. The measurements were performed by the StepOne™ Plus Real Time Machine and predesigned TaqMan gene expression probes that are listed in 8.1.5.2. Glycerinaldehyde-3-phosphate-dehydrogenase (Gapdh) was used as an internal reference transcript. Relative quantification was performed according to the $\Delta\Delta C_T$ method. The reaction mixture and the reaction conditions are listed in the table below.

Reaction mixture			
TaqMan™ Gene Expression Master-Mix (2x)			10 µl
TaqMan™ probes			1 µl
cDNA (1:5 dilution)			2 µl
dd H_2O			ad 20 µl
Reaction conditions			
PCR step	Temperature (°C)	Time (min:s)	Cycles
1	50	2:00	1
2	95	10:00	1
3	95 60	00:15 1:00	40

8.2.1.7 RNA sequencing by GATC

RNA sequencing was performed for genome-wide expression analysis. For that, 1 µg of RNA isolated from bone marrow cells was used. The analysis was performed on pooled samples of three independent experiments by GATC Biotech AG (Konstanz, Germany) in the context of the Inview Transcriptome Discover package and on an Illumina Inc. (San Diego, CA, USA) platform with a eukaryotic standard library, 150 bp paired-end-reads and at least 30 million read pairs. Sequencing quality, the normalization of the data, and the generation of fragments per kilobase million (FPKM) values were performed by GATC Biotech AG. The latter were used to generate signal log ratios with base 2.

8.2.1.8 Affymetrix Gene Chip hybridization

Affymetrix Gene Chip hybridization was performed for genome-wide expression analysis. More specifically, primary calvarial osteoblasts were cultured for 10 days under osteogenic conditions. After RNA isolation (8.2.1.4), samples were reverse-transcribed into cDNA (8.2.1.5). This cDNA was hybridized on Affymetrix Gene Chips according to the manufacturer´s protocol. The resulting expression pattern was analyzed using Affymetrix software (TAC).

8.2.2 Cell biological analysis

8.2.2.1 Isolation of primary osteoblasts

To obtain bone marrow for osteoblast cultures, tibiae, femora and pelves were dissected from 8 weeks old or older mice. The medullary cavities of these bones were opened under sterile conditions and put into a PCR reaction tube with a small hole on the ground. These PCR reaction tubes were put into 1.5 ml reaction tubes. With a 16 seconds centrifugation step at 8000 xg, bone marrow was separated from the bone into the 1.5 ml reaction tube. Bone marrow samples of the same genotypes were supplied with osteoblastic medium, pooled and strained (70 µm). After cell counting, the isolated cells were plated in a concentration of 5 x 10^6 cells per ml.

To obtain calvarial osteoblast cultures, the calvariae of 3 to 5 days old mice pups were dissected, separated from surrounding tissues and washed in phosphate buffered saline (PBS). Next, the calvariae were digested for 15 minutes in 10 ml digestion medium at 37 °C and 225 rpm. The supernatant was discarded and the samples were digested for another

45 minutes in 18 ml digestion medium at 37 °C and 225 rpm. After straining (70 µm), the supernatant was centrifuged for 5 minutes at 1400 rpm to obtain a pellet with calvarial osteoblastic cells. After discarding the supernatant, the cells were supplied with osteoblastic medium, counted and plated in a concentration of 5 x 10^4 cells per ml.

For both isolation methods, the cells were cultivated at 37 °C, 5 % CO_2 and 100 % rH in osteoblastic medium. At 80 % to 90 % confluence, cells were differentiated by adding differentiation medium. The change of medium was performed every second to third day.

8.2.2.2 Isolation of primary osteoclasts

To obtain osteoclast cultures, bone marrow cells were isolated like described in 8.2.2.1 for primary bone marrow osteoblasts. Different from the osteoblast isolation, osteoclasts were supplied with osteoclastic medium, pooled and strained (70 µm). After cell counting, the isolated cells were plated in a concentration of 5 x 10^6 cells per ml together with 10 nM of VitD. The cells were cultivated at 37 °C, 5 % CO_2 and 100 % rH. After 2 to 3 days of cultivation, osteoclastic differentiation medium was used for cultivation. The change of medium was performed every second to third day.

8.2.2.3 Stimulation of cultured cells

To test the influence of the Notch2 ligand Dll1 on cultured *Notch2*$^{+/+}$ and *Notch2* $^{+/HCS}$ calvarial osteoblasts on transcriptional level, these cells were treated for 6 hours, 12 hours, and 24 hours either with 100 ng/ml recombinant mouse Dll1 Fc chimera in minimal medium or PBS in minimal medium as a control after 7 days of differentiation. Before treatment, cells were serum starved for 18 hours with minimal medium. To test the influence of the Notch2 ligand Dll1 on cultured *Notch2*$^{+/+}$ and *Notch2* $^{+/HCS}$ calvarial osteoblasts on a protein level, the cells were treated for 30 minutes with 100 ng/ml recombinant mouse Dll1 Fc chimera in minimal medium or PBS in minimal medium as a control after 7 days of differentiation. Before treatment, cells were also serum starved for 18 hours with minimal medium.

To test the influence of human parathyroid hormone PTH(1-34) on cultured *Wnt1*$^{+/+}$ and *Wnt1*$^{G177C/G177C}$ calvarial osteoblasts, these cells were treated for 6 hours with 10 nM of PTH(1-34) (Bachem) in minimal medium or PBS in minimal medium as a control after 20 days of differentiation. Before treatment, cells were serum starved for 18 hours with minimal medium.

8.2.2.4 Mineralization assay

To analyze the ability of cultured osteoblasts to form mineralized matrix, alizarin red staining was performed. After 5 to 20 days of differentiation, cells were fixed with cold 90 % ethanol, washed twice with water and incubated with 40 mM alizarin red staining solution at room temperature for 10 minutes. This staining was followed by 5 washes with water. Quantification of stained cultures was performed by 30 minutes incubation with 800 µl of 10 % acetic acid followed by scraping the cell layer off and transferring it into a 1.5 ml reaction tube. These reaction tubes were heated for 10 minutes at 85 °C and subsequently centrifuged for 10 minutes at 13000 xg at room temperature. To bring the pH to 4.1 up to 4.5, 400 µl of supernatant was neutralized with 50 µl of 10 % ammonium hydroxide and then 150 µl of each sample was taken to measure the absorption at 405 nm at the photometer.

8.2.2.5 Dentin resorption assay

To analyze the ability of cultured osteoclasts to form resorption pits, sterile dentin slices of 1 mm thickness (obtained from the IOBM) were placed into 12-well plates and 5 x 10^6 bone marrow cells were seeded onto it. After 10 days of differentiation, the dentin slices were incubated in 2 ml sodium hypochloride for 10 minutes. The remaining cells were removed from the dentin slices by a cell scraper. For visualization of resorbed areas, the dentin slices were incubated 3 times in 0.2 % toluidine blue staining solution for a few seconds, rinsed and the resorbed area was quantified by ImageJ.

8.2.2.6 Tartrate-resistant-acid-phosphatase assay

The tartrate-resistance-acid-phosphatase (TRAP) assay was performed to visualize the activity and quantity of cultured osteoclasts. The cells were cultured for 5 to 10 days and were then rinsed with PBS, fixed with cold methanol for 5 minutes and rinsed again. After fixation, the cells were exposed to 1 ml TRAP-substrate solution per 12-well for 60 minutes. After staining, the cells were rinsed, stored in PBS and the number of TRAP-positive cells was determined by visual inspection.

8.2.3 Biochemical analysis

8.2.3.1 Protein isolation

To detect specific proteins from total cell lysates, cultured cells were lysed by 100 µl radio-immunoprecipitation assay buffer (RIPA buffer) per 12-well at day 5 of differentiation, scratched from the plate surface and incubated at 4 °C for 10 minutes. Subsequently, the lysed cells were transferred into a 1.5 ml reaction tube, centrifuged at 16000 xg at 4 °C for 10 minutes and the supernatant was frozen in liquid nitrogen and stored at -80 °C.

8.2.3.2 Bradford protein assay

The Bradford assay is a colorimetric protein assay to measure the concentration of protein in a solution[144]. Bovine serum albumin (BSA) was used to generate a standard curve with 0 µg, 5 µg, 10 µg, 15 µg and 20 µg of protein that was diluted with water to a total volume of 800 µl. Then 200 µl of Bradford solution was added to each sample and the optical density at 595 nm was measured at a microplate reader after 5 minutes of incubation. The protein concentrations were calculated on the basis of the linear standard curve.

8.2.3.3 Sodiumdodecyl sulfate-polyacrylamide gel electrophoresis

Sodiumdodecyl sulfate-polyacrylamide gel electrophoresis (SDS-PAGE) is a biochemical analytical method to separate charged molecules by molecular mass in an electric field. In this thesis, a mini electrophoresis system was used. The composition of gels is listed below. For analysis, 10 µg of isolated protein was mixed with sample buffer, heated for 5 to 10 minutes at 95 °C and loaded onto the gel. The gel ran for 15 minutes at 100 V, followed by further 60 minutes at 150 V.

	Seperation Gel	**Stacking Gel**
Concentration	12.5 %	-
Water	3.3 ml	3 ml
Seperation/ Stacking Buffer	2.5 ml	1.25 ml
30 % Acrylamide	4.2 ml	0.75 ml
TEMED	8 µl	10 µl
10 % APS	50 µl	50 µl

8.2.3.4 Western blot

A western blot is an antibody-based method to detect specific proteins within a given sample or set of samples. In this thesis, the Mini Trans-Blot was used. After electrophoretic separation by SDS-PAGE, the protein samples were immobilized onto a polyvinylidene

difluoride (PVDF) membrane. The SDS-gel and filter papers were equilibrated in transfer buffer for 15 minutes prior to electroblotting. The PVDF membrane was activated in methanol for 15 seconds, rinsed in water and then equilibrated in transfer buffer for 15 minutes prior to electroblotting. The process of transfer was performed at 90 V for 2 hours or 30 V overnight. After successful transfer, the membrane was blocked for 120 minutes with 5 % skim milk. For the detection of proteins, primary antibody incubation with the PVDF membrane was performed at 4 °C on a rotating shaker overnight. After primary antibody incubation, the membrane was rinsed three times with washing buffer for 5 minutes and subsequently incubated with the horseradish peroxidase-conjugated secondary antibody for 1 hour at room temperature and rinsed again for three times with washing buffer for 5 minutes. Used primary and secondary antibodies are listed in 8.1.6. For final protein detection, the membrane was incubated with 5 ml enhanced chemiluminescence solution (ECL solution) for 1 minute and put into a dark chamber. A western blot film was put onto the membrane in the dark chamber for 15 seconds to 30 minutes. The western blot film was developed in a x-ray film processor.

8.2.3.5 Enzyme-linked immunosorbent assay

In this thesis, enzyme-linked immunosorbent assays (ELISAs) were used to study the presence of specific substances in murine serum samples. Analysis of serum concentrations of crosslaps (CTx), IL-6, and procollagen N-terminal peptide (PINP) were performed according to manufacturer´s instructions.

8.2.3.6 Immunohistochemistry of bone marrow

Immunohistochemistry is a method to selectively visualize antigens on cells. For that, decalcified paraffin-embedded sections of 5 µm thickness were used (8.2.8.2). To remove paraffin wax, sections were placed 3 times into xylene for 5 minutes each. Afterwards, sections were rehydrated by placing them 2 times into 100 % EtOH for 10 minutes each, followed by 2 times in 95 % EtOH for 10 minutes each. For rehydration completion, the sections were placed 2 times into distilled water for 5 minutes each. After digestion for 10 minutes at 37 °C in pepsin, the sections were washed and subsequently incubated in 3 % hydrogen peroxide for 15 minutes. This step was followed by incubation with 5 % BSA for 30 minutes to block non-specific antibody binding in a humidified chamber. After incubation with the primary antibody at 4°C overnight, the secondary antibody was used, followed by

incubation with a streptavidin/HRP. The activity of peroxidase was detected by using DAB as a chromogenic substrate. Finally, the sections were counterstained with hematoxylin, dehydrated, and mounted.

8.2.3.7 Immunohistochemistry of the brain

For immunohistochemical analysis polyclonal rabbit anti-Cux1 (1:100) or polyclonal rabbit anti-doublecortin (anti-DCX) (1:400) antibodies were utilized. Nuclei were visualized by DAPI staining prior to mounting using Fluoromount. Images were taken using a Keyence Fluorescence Microscope and processed with ImageJ software. The experiments were done in cooperation with Ahmed Sharaf from the Center for Molecular Neurobiology Hamburg.

8.2.4 Animal experiments

8.2.4.1 Mouse models

8.2.4.1.1 Notch2^{HCS} mice

Notch HCS mice were generated at the Department for Osteology and Biomechanics by Timur Yorgan in cooperation with the Transgenic Mouse Facility of the University Medical Center Hamburg-Eppendorf. A targeting construct harboring the *Notch2* 6272delT mutation (Gene Bridges GmbH) was used to generate modified 129Sv-derived R1 embryonic stem cells by homologous recombination.

8.2.4.1.2 S1pr3-deficient mice

S1pr3-deficient mice were obtained from the University of San Diego and generated by Jerold Chun[145].

8.2.4.1.3 Wnt1-floxed mice

Wnt1 floxed mice (B6.B6--Wnt1^{tm2Hhtg}/UKE) were obtained from and generated by EUCOMM (Wnt1tm1a(EUCOMM)Wtsi). Here, exon 2 up to exon 4 are flanked by loxP sites enabling Cre recombinase-mediated inactivation of the gene.

8.2.4.1.4 Lyz2-Cre mice

Lyz2-Cre mice (B6.129P2-$^{Lyz2tm1(cre)Ifo}$/J) were obtained from Jackson Laboratory (Maine, US). Initially, these mice were generated at the University of Cologne[146]. The expression of Cre-recombinase is controlled by the Lyz2 transcription factor, which is expressed in myoloid

cells such as granylocytes and macrophages. Because osteoclasts derive from these cells, this mouse line allows osteoclast-specific inactivation of loxP flanked genes.

8.2.4.1.5 Runx2-Cre mice

Runx2-Cre mice (Tg(Runx2-icre)1Jtuc) were obtained from the University of Ulm and generated by Jan Tuckermann. The expression of Cre-recombinase is controlled by the Runx2 transcription factor, which is active during early osteoblast differentiation. Therefore, these mice allow osteoblast-specific inactivation of loxP flanked genes.

8.2.4.1.6 Wnt1^{G177C} mice

Wnt1 G177C mice (B6;129-Wnt1^{tmPG}/UKE) were generated by Polygene AG (Swizerland) by homologous recombination. The targeting construct harbors a disease causing *Wnt1* c.529G>T and a silent *Wnt1* c534G>A mutation.

8.2.4.2 Animal husbandry

Mice were kept in a specific pathogen-free environment in open or individually ventilated cages with wood shavings bedding and nesting material at the Forschungstierhaltung (FTH) of the animal facility of the University Medical Center Hamburg-Eppendorf. The FTH provided a 12-hour-light/dark cycle, 45 to 65 % relative humidity and 20 to 24 °C ambient temperature. The mice were kept in groups not surpassing 6 animals and had access to tap water and standard rodent chow (1328P, Altromin Spezialfutter GmbH & Co. KG) *ad libitum*.

8.2.4.3 Treatment of mice

After the initiation of a specific treatment, the welfare of mice was assessed by daily overall appearance and body weight inspection. The animal experiments were approved by the animal facility of the University Medical Center Hamburg-Eppendorf and by the "Behörde für Soziales, Familie, Gesundheit und Verbraucherschutz".

8.2.4.4 Organ taking

To obtain the skeleton or other organs, mice were first anesthetized with 80 % (v/v) CO_2/O_2 mixture followed by euthanization with 100 % CO_2. The blood was taken by cardiac puncture *post mortem* and transferred into a 1.5 ml reaction tube. After centrifugation at 6000 rpm for 6 minutes, the serum supernatant was transferred into a new 1.5 ml reaction tube and stored at -80 °C. The skeleton was taken and fixed in 3.5 % formaldehyde for 24 hours before

they were transferred into 80 % Ethanol for long time storage. The application numbers are Org529 and Org869.

8.2.4.5 Alendronate treatment of mice

To analyze the influence of bisphosphonates on bone metabolism, *Notch2*$^{+/+}$ and *Notch2*$^{+/HCS}$ mice were treated for 6 weeks until the age of 24 weeks with 300 µg/kg/wk alendronate or an equivalent volume of PBS as a control through intraperitoneal injection. The animal application number is G15/131.

8.2.4.6 Calcein treatment of mice

For assessment of kinetic histomorphometry, 10 and 3 days prior to sacrifice, mice were treated with 30 mg/kg of calcein solution through intraperitoneal injection. The animal application numbers are G14/035, G17/034.

8.2.4.7 Parathyroid hormone treatment of mice

To analyze the influence of PTH(1-34) on bone formation, *Wnt1*$^{+/+}$ and *Wnt1*$^{G177C/G177C}$ mice were treated for 2 weeks until the age of 12 weeks with 2 µg/d PTH(1-34) by intraperitoneal injection. The animal application number is G16/117.

8.2.4.8 Bone marrow transplantation of mice

At 8 weeks of age, female *Notch2*$^{+/+}$ and *Notch2*$^{+/HCS}$ mice were irradiated with 9.5 Gy before receiving a full bone marrow transplantation (BMT) from 8 weeks old male donor *Notch2*$^{+/+}$ mice intravenously. The animal application number is G14/104.

8.2.5 Radiologic analysis

8.2.5.1 Contact X-rays

Fixed skeletons or single bones were analyzed by contact radiography at 35 kV for 2 seconds in the X-ray apparatus on x-ray films before they were developed in an X-ray Film Processor.

8.2.5.2 Micro-computed tomography

Micro-computed tomography (µCT) analyses were performed to obtain 3-dimensional reconstructions of bones and to analyze relevant parameters. The right femur of each mouse was dissected and fixed as described in section 8.2.2.4. The scanning procedure was performed with a voxel resolution of 10 µm using a µCT 40 desktop cone-beam µCT. The

trabecular bone was analyzed in the distal metaphysis in a volume situated 2500 µm to 500 µm proximal of the distal growth plate. Cortical bone was analyzed in a 1000 µm long volume situated in the middle of the diaphysis. The evaluation of cortical bone was performed with a threshold of 300, whereas a threshold of 250 was used for the evaluation of trabecular bone.

8.2.6 Biomechanical analysis

8.2.6.1 3-point bending

A 3-point-bending test was performed to analyze biomechanical properties of bone. To do so, femora were dissected and tested using a universal testing machine Z2.5/TN1S. The femora were centrally positioned in a horizontally state with the anterior surface facing downward at a bearing distance of 7 mm. To ensure no movement of the sample, a preforce of 2 N was applied. Load-displacement data was recorded at 100 Hz until failure of the bone. These experiments were performed in cooperation with Felix Schmidt from the Department for Osteology and Biomechanics.

8.2.7 Bone mineral density distribution

8.2.7.1 Quantitative backscattered electron imaging

The method of quantitative backscattered electron imaging (qBEI) was performed to analyze the bone mineral density distribution. For that, embedded tibiae were coated with carbon. Subsequently, identical regions of cortical bone were analyzed using a scanning electron microscope at 20 kV and 680 pA with a constant working distance of 20 mm. Grey-value images were used for analyses according to previously described protocols[147-149]. Calibration was performed using a carbon-aluminium standard. These experiments were performed in cooperation with Tim Rolvien from the Department for Osteology and Biomechanics.

8.2.8 Histologic analysis

8.2.8.1 Acrylate histology

The lumbar vertebral bodies L1 to L4 and the left tibia of each mouse were dehydrated in ascending alcohol (EtOH) concentrations (1 h to 5 h 70 % EtOH, 2 times 1 h 80 % EtOH, 4 times 1 h 96 % EtOH, 4 times 1 h 96 % EtOH). After 24 hours of incubation in Infiltration

solution I at 4 °C, the samples were transferred into Infiltration solution II for another 24 hours at 4 °C. After that, the samples were embedded in methylmethacrylate in a small glass vial with rolled rims for sectioning. After polymerization at 4 °C, the block was released from the glass and sections of 4 µm thickness (for structural and cellular histomorphometry) and 12 µm (for dynamic histomorphometry) were cut on an acrylate microtome in the sagittal plane. After picking up the sections by a microscope slide coated with potassium alum, the sections were stretched with 80 % isopropyl alcohol and dibutyl ether. Finally, the slides were dried at 60 °C overnight.

8.2.8.2 Paraffin histology

Fixed decalcified bone or fixed soft tissues were dehydrated in ascending alcohol concentrations (2 times 1 h 70 % EtOH, 1 time 1 h 80 % EtOH, 2 times 1 h 96 % EtOH, 2 times 1 h 100 % EtOH, 2 times 1 h xylene). The dehydrated samples were immediately embedded in warm and liquid paraffin. As soon as the embedded samples in paraffin were dried, sections of 2 µm to 3 µm were cut on a paraffin microtome and picked up by a microscope slide. The paraffin sections were fixed on the slide by heating them for 30 minutes at 60 °C.

8.2.8.3 Histologic stainings

8.2.8.3.1 Von Kossa/van Giesson staining

Von Kossa/van Giesson stainings were performed for analysis of structural histomorphometry. Mineralized bone was stained in black, whereas osteoid and soft tissues were stained in red. To dispose the samples of 4 µm thickness of plastic, they were incubated for 3 times in 2-Methoxyethylacetate for 5 minutes. After that, the slides were rehydrated in descending alcohol concentrations (2 times 2 min 100 % EtOH, 2 min 96 % EtOH, 2 min 80 % EtOH, 2 min 70 % EtOH, 2 min 50 % EtOH). The samples were rinsed with water, stained with 3 % silver nitrate for 5 minutes, rinsed with water for 10 minutes, stained in soda-formol solution, rinsed with water for 10 minutes, stained in 5 % sodium thiosulfate for 5 minutes, rinsed in water for 10 minutes and counterstained with van Giesson solution for another 20 minutes. Finally, the slides were dehydrated in ascending alcohol concentrations, 3 times incubated in xylene for 5 minutes, mounted with DPX mounting solution, and covered with a coverslip.

8.2.8.3.2 Toluidinblue Staining

Toluidinblue stainings were performed to analyze cellular histomorphometry. More specifically, different tissues and cellular compartments were stained in different shades of blue, depending on the DNA and RNA contents of the cell compartments. To dispose the samples of 4 µm thickness of plastic, they were incubated 3 times in 2-Methoxyethylacetate for 5 minutes. This was followed by a rehydration in descending alcohol concentrations (2 times 2 min 100 % EtOH, 2 min 96 % EtOH, 2 min 80 % EtoH, 2 min 70 % EtOH, 2 min 50 % EtOH), rinsing in water, staining in toluidinblue staining solution for 30 minutes, another rinse in water followed by dehydration through ascending alcohol concentrations. Finally, the slides were incubated 3 times in xylene for 5 minutes, mounted with DPX mounting solution, and covered with a coverslip.

8.2.8.4 Histomorphometric quantification

The analysis of bone volume per tissue volume (BV/TV), trabecular number (Tb.N), trabecular thickness (Tb.Th) and trabecular spacing (Tb.Sp) was performed using Bioquant software on van Kossa/van Giesson slides. Histomorphometric measurements of cellular parameters like number of osteoblasts per bone perimeter (N.Ob/B.Pm), number of osteoclasts per bone perimeter (N.Oc/B.Pm), osteoblast surface per bone surface (Ob.S/BS), osteoclast surface per bone surface (Oc.S/BS), number of osteocytes per bone area (N.Ot/B.Ar), as well as dynamic parameters like bone formation rate per bone surface (BFR/BS) were performed using the OsteoMeasure histomorphometry system. Cellular histomorphometry was performed using toluidinblue stained slides of lumbar vertebral sections, whereas dynamic histomorphometry was carried out on 12 µm non-stained slides of lumbar vertebral sections.

8.2.9 Statistical analysis

All data shown in this thesis are presented as means ± standard deviation. Statistical analysis was performed using unpaired, two-tailed Student's t-test, Mantel-Cox log rank test or χ^2 test. Any *p* values below 0.05 were considered as statistically significant.

9 References

1. Zaidi, M., *Skeletal remodeling in health and disease.* Nat Med, 2007. **13**(7): p. 791-801.

2. Clarke, B., *Normal bone anatomy and physiology.* Clin J Am Soc Nephrol, 2008. **3 Suppl 3**: p. S131-9.

3. Brodsky, B. and A.V. Persikov, *Molecular structure of the collagen triple helix.* Adv Protein Chem, 2005. **70**: p. 301-39.

4. Wu, M. and J.S. Crane, *Biochemistry, Collagen Synthesis*, in *StatPearls*. 2018: Treasure Island (FL).

5. Yoshiko, Y., G.A. Candeliere, N. Maeda, and J.E. Aubin, *Osteoblast autonomous Pi regulation via Pit1 plays a role in bone mineralization.* Mol Cell Biol, 2007. **27**(12): p. 4465-74.

6. Roberts, S., S. Narisawa, D. Harmey, J.L. Millan, and C. Farquharson, *Functional involvement of PHOSPHO1 in matrix vesicle-mediated skeletal mineralization.* J Bone Miner Res, 2007. **22**(4): p. 617-27.

7. Florencio-Silva, R., G.R. Sasso, E. Sasso-Cerri, M.J. Simoes, and P.S. Cerri, *Biology of Bone Tissue: Structure, Function, and Factors That Influence Bone Cells.* Biomed Res Int, 2015. **2015**: p. 421746.

8. Bennett, C.N., K.A. Longo, W.S. Wright, L.J. Suva, T.F. Lane, K.D. Hankenson, and O.A. MacDougald, *Regulation of osteoblastogenesis and bone mass by Wnt10b.* Proc Natl Acad Sci U S A, 2005. **102**(9): p. 3324-9.

9. Capulli, M., R. Paone, and N. Rucci, *Osteoblast and osteocyte: games without frontiers.* Arch Biochem Biophys, 2014. **561**: p. 3-12.

10. Ducy, P., R. Zhang, V. Geoffroy, A.L. Ridall, and G. Karsenty, *Osf2/Cbfa1: a transcriptional activator of osteoblast differentiation.* Cell, 1997. **89**(5): p. 747-54.

11. Fakhry, M., E. Hamade, B. Badran, R. Buchet, and D. Magne, *Molecular mechanisms of mesenchymal stem cell differentiation towards osteoblasts.* World J Stem Cells, 2013. **5**(4): p. 136-48.

12. Nakashima, K., X. Zhou, G. Kunkel, Z. Zhang, J.M. Deng, R.R. Behringer, and B. de Crombrugghe, *The novel zinc finger-containing transcription factor osterix is required for osteoblast differentiation and bone formation.* Cell, 2002. **108**(1): p. 17-29.

13. Yoshida, C.A., H. Komori, Z. Maruyama, T. Miyazaki, K. Kawasaki, T. Furuichi, R. Fukuyama, M. Mori, K. Yamana, K. Nakamura, W. Liu, S. Toyosawa, T. Moriishi, H. Kawaguchi, K. Takada, and T. Komori, *SP7 inhibits osteoblast differentiation at a late stage in mice.* PLoS One, 2012. **7**(3): p. e32364.

14. Glass, D.A., 2nd, P. Bialek, J.D. Ahn, M. Starbuck, M.S. Patel, H. Clevers, M.M. Taketo, F. Long, A.P. McMahon, R.A. Lang, and G. Karsenty, *Canonical Wnt signaling in differentiated osteoblasts controls osteoclast differentiation.* Dev Cell, 2005. **8**(5): p. 751-64.

15. Hu, H., M.J. Hilton, X. Tu, K. Yu, D.M. Ornitz, and F. Long, *Sequential roles of Hedgehog and Wnt signaling in osteoblast development.* Development, 2005. **132**(1): p. 49-60.

16. Boivin, G., Y. Bala, A. Doublier, D. Farlay, L.G. Ste-Marie, P.J. Meunier, and P.D. Delmas, *The role of mineralization and organic matrix in the microhardness of bone tissue from controls and osteoporotic patients.* Bone, 2008. **43**(3): p. 532-8.

17. Del Fattore, A., A. Teti, and N. Rucci, *Bone cells and the mechanisms of bone remodelling.* Front Biosci (Elite Ed), 2012. **4**: p. 2302-21.

18. Bellido, T., *Osteocyte-driven bone remodeling.* Calcif Tissue Int, 2014. **94**(1): p. 25-34.

19. Franz-Odendaal, T.A., B.K. Hall, and P.E. Witten, *Buried alive: how osteoblasts become osteocytes.* Dev Dyn, 2006. **235**(1): p. 176-90.

20. Dudley, H.R. and D. Spiro, *The Fine Structure of Bone Cells.* J Biophys Biochem Cytol, 1961. **11**(3): p. 627-49.

21. Paic, F., J.C. Igwe, R. Nori, M.S. Kronenberg, T. Franceschetti, P. Harrington, L. Kuo, D.G. Shin, D.W. Rowe, S.E. Harris, and I. Kalajzic, *Identification of differentially expressed genes between osteoblasts and osteocytes.* Bone, 2009. **45**(4): p. 682-92.

22. Bonewald, L.F., *The amazing osteocyte.* J Bone Miner Res, 2011. **26**(2): p. 229-38.

23. Suda, T., N. Takahashi, and T.J. Martin, *Modulation of osteoclast differentiation.* Endocr Rev, 1992. **13**(1): p. 66-80.

24. Roodman, G.D., *Advances in bone biology: the osteoclast.* Endocr Rev, 1996. **17**(4): p. 308-32.

25. Kwon, O.H., C.K. Lee, Y.I. Lee, S.G. Paik, and H.J. Lee, *The hematopoietic transcription factor PU.1 regulates RANK gene expression in myeloid progenitors.* Biochem Biophys Res Commun, 2005. **335**(2): p. 437-46.

26. Yavropoulou, M.P. and J.G. Yovos, *Osteoclastogenesis--current knowledge and future perspectives.* J Musculoskelet Neuronal Interact, 2008. **8**(3): p. 204-16.

27. Yoshida, H., S. Hayashi, T. Kunisada, M. Ogawa, S. Nishikawa, H. Okamura, T. Sudo, L.D. Shultz, and S. Nishikawa, *The murine mutation osteopetrosis is in the coding region of the macrophage colony stimulating factor gene.* Nature, 1990. **345**(6274): p. 442-4.

28. Insogna, K.L., M. Sahni, A.B. Grey, S. Tanaka, W.C. Horne, L. Neff, M. Mitnick, J.B. Levy, and R. Baron, *Colony-stimulating factor-1 induces cytoskeletal reorganization*

and c-src-dependent tyrosine phosphorylation of selected cellular proteins in rodent osteoclasts. J Clin Invest, 1997. **100**(10): p. 2476-85.

29. Sodek, J., B. Ganss, and M.D. McKee, *Osteopontin.* Crit Rev Oral Biol Med, 2000. **11**(3): p. 279-303.

30. Teitelbaum, S.L. and F.P. Ross, *Genetic regulation of osteoclast development and function.* Nat Rev Genet, 2003. **4**(8): p. 638-49.

31. Takahashi, N., N. Udagawa, and T. Suda, *A new member of tumor necrosis factor ligand family, ODF/OPGL/TRANCE/RANKL, regulates osteoclast differentiation and function.* Biochem Biophys Res Commun, 1999. **256**(3): p. 449-55.

32. Mulari, M., J. Vaaraniemi, and H.K. Vaananen, *Intracellular membrane trafficking in bone resorbing osteoclasts.* Microsc Res Tech, 2003. **61**(6): p. 496-503.

33. Kular, J., J. Tickner, S.M. Chim, and J. Xu, *An overview of the regulation of bone remodelling at the cellular level.* Clin Biochem, 2012. **45**(12): p. 863-73.

34. Li, X., L. Qin, M. Bergenstock, L.M. Bevelock, D.V. Novack, and N.C. Partridge, *Parathyroid hormone stimulates osteoblastic expression of MCP-1 to recruit and increase the fusion of pre/osteoclasts.* J Biol Chem, 2007. **282**(45): p. 33098-106.

35. Teitelbaum, S.L., *Osteoclasts: what do they do and how do they do it?* Am J Pathol, 2007. **170**(2): p. 427-35.

36. Harada, S. and G.A. Rodan, *Control of osteoblast function and regulation of bone mass.* Nature, 2003. **423**(6937): p. 349-55.

37. Centrella, M., T.L. McCarthy, and E. Canalis, *Transforming growth factor-beta and remodeling of bone.* J Bone Joint Surg Am, 1991. **73**(9): p. 1418-28.

38. Hayden, J.M., S. Mohan, and D.J. Baylink, *The insulin-like growth factor system and the coupling of formation to resorption.* Bone, 1995. **17**(2 Suppl): p. 93S-98S.

39. Wozney, J.M., V. Rosen, A.J. Celeste, L.M. Mitsock, M.J. Whitters, R.W. Kriz, R.M. Hewick, and E.A. Wang, *Novel regulators of bone formation: molecular clones and activities.* Science, 1988. **242**(4885): p. 1528-34.

40. Sobacchi, C., A. Frattini, M.M. Guerrini, M. Abinun, A. Pangrazio, L. Susani, R. Bredius, G. Mancini, A. Cant, N. Bishop, P. Grabowski, A. Del Fattore, C. Messina, G. Errigo, F.P. Coxon, D.I. Scott, A. Teti, M.J. Rogers, P. Vezzoni, A. Villa, and M.H. Helfrich, *Osteoclast-poor human osteopetrosis due to mutations in the gene encoding RANKL.* Nat Genet, 2007. **39**(8): p. 960-2.

41. Guerrini, M.M., C. Sobacchi, B. Cassani, M. Abinun, S.S. Kilic, A. Pangrazio, D. Moratto, E. Mazzolari, J. Clayton-Smith, P. Orchard, F.P. Coxon, M.H. Helfrich, J.C. Crockett, D. Mellis, A. Vellodi, I. Tezcan, L.D. Notarangelo, M.J. Rogers, P. Vezzoni, A. Villa, and A. Frattini, *Human osteoclast-poor osteopetrosis with*

hypogammaglobulinemia due to TNFRSF11A (RANK) mutations. Am J Hum Genet, 2008. **83**(1): p. 64-76.

42. Pederson, L., M. Ruan, J.J. Westendorf, S. Khosla, and M.J. Oursler, *Regulation of bone formation by osteoclasts involves Wnt/BMP signaling and the chemokine sphingosine-1-phosphate.* Proc Natl Acad Sci U S A, 2008. **105**(52): p. 20764-9.

43. Keller, J., P. Catala-Lehnen, A.K. Huebner, A. Jeschke, T. Heckt, A. Lueth, M. Krause, T. Koehne, J. Albers, J. Schulze, S. Schilling, M. Haberland, H. Denninger, M. Neven, I. Hermans-Borgmeyer, T. Streichert, S. Breer, F. Barvencik, B. Levkau, B. Rathkolb, E. Wolf, J. Calzada-Wack, F. Neff, V. Gailus-Durner, H. Fuchs, M.H. de Angelis, S. Klutmann, E. Tsourdi, L.C. Hofbauer, B. Kleuser, J. Chun, T. Schinke, and M. Amling, *Calcitonin controls bone formation by inhibiting the release of sphingosine 1-phosphate from osteoclasts.* Nat Commun, 2014. **5**: p. 5215.

44. Ryu, J., H.J. Kim, E.J. Chang, H. Huang, Y. Banno, and H.H. Kim, *Sphingosine 1-phosphate as a regulator of osteoclast differentiation and osteoclast-osteoblast coupling.* EMBO J, 2006. **25**(24): p. 5840-51.

45. Ishii, M., J.G. Egen, F. Klauschen, M. Meier-Schellersheim, Y. Saeki, J. Vacher, R.L. Proia, and R.N. Germain, *Sphingosine-1-phosphate mobilizes osteoclast precursors and regulates bone homeostasis.* Nature, 2009. **458**(7237): p. 524-8.

46. Weivoda, M.M., M. Ruan, L. Pederson, C. Hachfeld, R.A. Davey, J.D. Zajac, J.J. Westendorf, S. Khosla, and M.J. Oursler, *Osteoclast TGF-beta Receptor Signaling Induces Wnt1 Secretion and Couples Bone Resorption to Bone Formation.* J Bone Miner Res, 2016. **31**(1): p. 76-85.

47. Ma, Y.L., R.L. Cain, D.L. Halladay, X. Yang, Q. Zeng, R.R. Miles, S. Chandrasekhar, T.J. Martin, and J.E. Onyia, *Catabolic effects of continuous human PTH (1--38) in vivo is associated with sustained stimulation of RANKL and inhibition of osteoprotegerin and gene-associated bone formation.* Endocrinology, 2001. **142**(9): p. 4047-54.

48. Martin, T.J., *Osteoblast-derived PTHrP is a physiological regulator of bone formation.* J Clin Invest, 2005. **115**(9): p. 2322-4.

49. Horwood, N.J., J. Elliott, T.J. Martin, and M.T. Gillespie, *Osteotropic agents regulate the expression of osteoclast differentiation factor and osteoprotegerin in osteoblastic stromal cells.* Endocrinology, 1998. **139**(11): p. 4743-6.

50. Ragab, A.A., J.L. Nalepka, Y. Bi, and E.M. Greenfield, *Cytokines synergistically induce osteoclast differentiation: support by immortalized or normal calvarial cells.* Am J Physiol Cell Physiol, 2002. **283**(3): p. C679-87.

51. Aubin, J.E. and E. Bonnelye, *Osteoprotegerin and its ligand: a new paradigm for regulation of osteoclastogenesis and bone resorption.* Osteoporos Int, 2000. **11**(11): p. 905-13.

52. Tatsumi, S., K. Ishii, N. Amizuka, M. Li, T. Kobayashi, K. Kohno, M. Ito, S. Takeshita, and K. Ikeda, *Targeted ablation of osteocytes induces osteoporosis with defective mechanotransduction.* Cell Metab, 2007. **5**(6): p. 464-75.

53. Yorgan, T.A., S. Peters, A. Jeschke, P. Benisch, F. Jakob, M. Amling, and T. Schinke, *The Anti-Osteoanabolic Function of Sclerostin Is Blunted in Mice Carrying a High Bone Mass Mutation of Lrp5.* J Bone Miner Res, 2015. **30**(7): p. 1175-83.

54. Winkler, D.G., M.K. Sutherland, J.C. Geoghegan, C. Yu, T. Hayes, J.E. Skonier, D. Shpektor, M. Jonas, B.R. Kovacevich, K. Staehling-Hampton, M. Appleby, M.E. Brunkow, and J.A. Latham, *Osteocyte control of bone formation via sclerostin, a novel BMP antagonist.* EMBO J, 2003. **22**(23): p. 6267-76.

55. Stark, Z. and R. Savarirayan, *Osteopetrosis.* Orphanet J Rare Dis, 2009. **4**: p. 5.

56. Appelman-Dijkstra, N.M. and S.E. Papapoulos, *From disease to treatment: from rare skeletal disorders to treatments for osteoporosis.* Endocrine, 2016. **52**(3): p. 414-26.

57. Li, X., Y. Zhang, H. Kang, W. Liu, P. Liu, J. Zhang, S.E. Harris, and D. Wu, *Sclerostin binds to LRP5/6 and antagonizes canonical Wnt signaling.* J Biol Chem, 2005. **280**(20): p. 19883-7.

58. Kang, H., A.C.S. Aryal, and J.C. Marini, *Osteogenesis imperfecta: new genes reveal novel mechanisms in bone dysplasia.* Transl Res, 2017. **181**: p. 27-48.

59. Marini, J.C., A. Reich, and S.M. Smith, *Osteogenesis imperfecta due to mutations in non-collagenous genes: lessons in the biology of bone formation.* Curr Opin Pediatr, 2014. **26**(4): p. 500-7.

60. Lindahl, K., B. Langdahl, O. Ljunggren, and A. Kindmark, *Treatment of osteogenesis imperfecta in adults.* Eur J Endocrinol, 2014. **171**(2): p. R79-90.

61. Marini, J.C., A. Forlino, H.P. Bachinger, N.J. Bishop, P.H. Byers, A. Paepe, F. Fassier, N. Fratzl-Zelman, K.M. Kozloff, D. Krakow, K. Montpetit, and O. Semler, *Osteogenesis imperfecta.* Nat Rev Dis Primers, 2017. **3**: p. 17052.

62. Johnell, O. and J.A. Kanis, *An estimate of the worldwide prevalence and disability associated with osteoporotic fractures.* Osteoporos Int, 2006. **17**(12): p. 1726-33.

63. Kanis, J.A., E.V. McCloskey, H. Johansson, C. Cooper, R. Rizzoli, J.Y. Reginster, C. Scientific Advisory Board of the European Society for, O. Economic Aspects of, Osteoarthritis, and F. the Committee of Scientific Advisors of the International Osteoporosis, *European guidance for the diagnosis and management of osteoporosis in postmenopausal women.* Osteoporos Int, 2013. **24**(1): p. 23-57.

64. Camacho, P.M., S.M. Petak, N. Binkley, B.L. Clarke, S.T. Harris, D.L. Hurley, M. Kleerekoper, E.M. Lewiecki, P.D. Miller, H.S. Narula, R. Pessah-Pollack, V. Tangpricha, S.J. Wimalawansa, and N.B. Watts, *American Association of Clinical Endocrinologists and American College of Endocrinology Clinical Practice Guidelines for the Diagnosis*

and Treatment of Postmenopausal Osteoporosis - 2016--Executive Summary. Endocr Pract, 2016. **22**(9): p. 1111-8.

65. Cosman, F., S.J. de Beur, M.S. LeBoff, E.M. Lewiecki, B. Tanner, S. Randall, and R. Lindsay, *Erratum to: Clinician's guide to prevention and treatment of osteoporosis.* Osteoporos Int, 2015. **26**(7): p. 2045-7.

66. Watts, N.B., R.A. Adler, J.P. Bilezikian, M.T. Drake, R. Eastell, E.S. Orwoll, J.S. Finkelstein, and S. Endocrine, *Osteoporosis in men: an Endocrine Society clinical practice guideline.* J Clin Endocrinol Metab, 2012. **97**(6): p. 1802-22.

67. Buckley, L., G. Guyatt, H.A. Fink, M. Cannon, J. Grossman, K.E. Hansen, M.B. Humphrey, N.E. Lane, M. Magrey, M. Miller, L. Morrison, M. Rao, A.B. Robinson, S. Saha, S. Wolver, R.R. Bannuru, E. Vaysbrot, M. Osani, M. Turgunbaev, A.S. Miller, and T. McAlindon, *2017 American College of Rheumatology Guideline for the Prevention and Treatment of Glucocorticoid-Induced Osteoporosis.* Arthritis Rheumatol, 2017. **69**(8): p. 1521-1537.

68. Cabrera, C.V., *Lateral inhibition and cell fate during neurogenesis in Drosophila: the interactions between scute, Notch and Delta.* Development, 1990. **110**(1): p. 733-42.

69. D'Souza, B., A. Miyamoto, and G. Weinmaster, *The many facets of Notch ligands.* Oncogene, 2008. **27**(38): p. 5148-67.

70. Kopan, R. and M.X. Ilagan, *The canonical Notch signaling pathway: unfolding the activation mechanism.* Cell, 2009. **137**(2): p. 216-33.

71. Iso, T., L. Kedes, and Y. Hamamori, *HES and HERP families: multiple effectors of the Notch signaling pathway.* J Cell Physiol, 2003. **194**(3): p. 237-55.

72. Fortini, M.E., *Notch signaling: the core pathway and its posttranslational regulation.* Dev Cell, 2009. **16**(5): p. 633-47.

73. Rechsteiner, M. and S.W. Rogers, *PEST sequences and regulation by proteolysis.* Trends Biochem Sci, 1996. **21**(7): p. 267-71.

74. Shen, J., R.T. Bronson, D.F. Chen, W. Xia, D.J. Selkoe, and S. Tonegawa, *Skeletal and CNS defects in Presenilin-1-deficient mice.* Cell, 1997. **89**(4): p. 629-39.

75. Dunwoodie, S.L., M. Clements, D.B. Sparrow, X. Sa, R.A. Conlon, and R.S. Beddington, *Axial skeletal defects caused by mutation in the spondylocostal dysplasia/pudgy gene Dll3 are associated with disruption of the segmentation clock within the presomitic mesoderm.* Development, 2002. **129**(7): p. 1795-806.

76. Zhang, N. and T. Gridley, *Defects in somite formation in lunatic fringe-deficient mice.* Nature, 1998. **394**(6691): p. 374-7.

77. Hilton, M.J., X. Tu, X. Wu, S. Bai, H. Zhao, T. Kobayashi, H.M. Kronenberg, S.L. Teitelbaum, F.P. Ross, R. Kopan, and F. Long, *Notch signaling maintains bone marrow*

mesenchymal progenitors by suppressing osteoblast differentiation. Nat Med, 2008. **14**(3): p. 306-14.

78. Zanotti, S., A. Smerdel-Ramoya, L. Stadmeyer, D. Durant, F. Radtke, and E. Canalis, *Notch inhibits osteoblast differentiation and causes osteopenia.* Endocrinology, 2008. **149**(8): p. 3890-9.

79. Engin, F., Z. Yao, T. Yang, G. Zhou, T. Bertin, M.M. Jiang, Y. Chen, L. Wang, H. Zheng, R.E. Sutton, B.F. Boyce, and B. Lee, *Dimorphic effects of Notch signaling in bone homeostasis.* Nat Med, 2008. **14**(3): p. 299-305.

80. Bulman, M.P., K. Kusumi, T.M. Frayling, C. McKeown, C. Garrett, E.S. Lander, R. Krumlauf, A.T. Hattersley, S. Ellard, and P.D. Turnpenny, *Mutations in the human delta homologue, DLL3, cause axial skeletal defects in spondylocostal dysostosis.* Nat Genet, 2000. **24**(4): p. 438-41.

81. McDaniell, R., D.M. Warthen, P.A. Sanchez-Lara, A. Pai, I.D. Krantz, D.A. Piccoli, and N.B. Spinner, *NOTCH2 mutations cause Alagille syndrome, a heterogeneous disorder of the notch signaling pathway.* Am J Hum Genet, 2006. **79**(1): p. 169-73.

82. Oda, T., A.G. Elkahloun, B.L. Pike, K. Okajima, I.D. Krantz, A. Genin, D.A. Piccoli, P.S. Meltzer, N.B. Spinner, F.S. Collins, and S.C. Chandrasekharappa, *Mutations in the human Jagged1 gene are responsible for Alagille syndrome.* Nat Genet, 1997. **16**(3): p. 235-42.

83. Simpson, M.A., M.D. Irving, E. Asilmaz, M.J. Gray, D. Dafou, F.V. Elmslie, S. Mansour, S.E. Holder, C.E. Brain, B.K. Burton, K.H. Kim, R.M. Pauli, S. Aftimos, H. Stewart, C.A. Kim, M. Holder-Espinasse, S.P. Robertson, W.M. Drake, and R.C. Trembath, *Mutations in NOTCH2 cause Hajdu-Cheney syndrome, a disorder of severe and progressive bone loss.* Nat Genet, 2011. **43**(4): p. 303-5.

84. Isidor, B., P. Lindenbaum, O. Pichon, S. Bezieau, C. Dina, S. Jacquemont, D. Martin-Coignard, C. Thauvin-Robinet, M. Le Merrer, J.L. Mandel, A. David, L. Faivre, V. Cormier-Daire, R. Redon, and C. Le Caignec, *Truncating mutations in the last exon of NOTCH2 cause a rare skeletal disorder with osteoporosis.* Nat Genet, 2011. **43**(4): p. 306-8.

85. Majewski, J., J.A. Schwartzentruber, A. Caqueret, L. Patry, J. Marcadier, J.P. Fryns, K.M. Boycott, L.G. Ste-Marie, F.E. McKiernan, I. Marik, H. Van Esch, F.C. Consortium, J.L. Michaud, and M.E. Samuels, *Mutations in NOTCH2 in families with Hajdu-Cheney syndrome.* Hum Mutat, 2011. **32**(10): p. 1114-7.

86. Yorgan, T., N. Vollersen, C. Riedel, A. Jeschke, S. Peters, B. Busse, M. Amling, and T. Schinke, *Osteoblast-specific Notch2 inactivation causes increased trabecular bone mass at specific sites of the appendicular skeleton.* Bone, 2016. **87**: p. 136-46.

87. Vollersen, N., I. Hermans-Borgmeyer, K. Cornils, B. Fehse, T. Rolvien, I. Triviai, A. Jeschke, R. Oheim, M. Amling, T. Schinke, and T.A. Yorgan, *High Bone Turnover in Mice Carrying a Pathogenic Notch2 Mutation Causing Hajdu-Cheney Syndrome.* J Bone Miner Res, 2018. **33**(1): p. 70-83.

88. Saito-Diaz, K., T.W. Chen, X. Wang, C.A. Thorne, H.A. Wallace, A. Page-McCaw, and E. Lee, *The way Wnt works: components and mechanism.* Growth Factors, 2013. **31**(1): p. 1-31.

89. Pinson, K.I., J. Brennan, S. Monkley, B.J. Avery, and W.C. Skarnes, *An LDL-receptor-related protein mediates Wnt signalling in mice.* Nature, 2000. **407**(6803): p. 535-8.

90. Tamai, K., M. Semenov, Y. Kato, R. Spokony, C. Liu, Y. Katsuyama, F. Hess, J.P. Saint-Jeannet, and X. He, *LDL-receptor-related proteins in Wnt signal transduction.* Nature, 2000. **407**(6803): p. 530-5.

91. Clevers, H., *Wnt/beta-catenin signaling in development and disease.* Cell, 2006. **127**(3): p. 469-80.

92. Westendorf, J.J., R.A. Kahler, and T.M. Schroeder, *Wnt signaling in osteoblasts and bone diseases.* Gene, 2004. **341**: p. 19-39.

93. Behrens, J., J.P. von Kries, M. Kuhl, L. Bruhn, D. Wedlich, R. Grosschedl, and W. Birchmeier, *Functional interaction of beta-catenin with the transcription factor LEF-1.* Nature, 1996. **382**(6592): p. 638-42.

94. Gong, Y., R.B. Slee, N. Fukai, G. Rawadi, S. Roman-Roman, A.M. Reginato, H. Wang, T. Cundy, F.H. Glorieux, D. Lev, M. Zacharin, K. Oexle, J. Marcelino, W. Suwairi, S. Heeger, G. Sabatakos, S. Apte, W.N. Adkins, J. Allgrove, M. Arslan-Kirchner, J.A. Batch, P. Beighton, G.C. Black, R.G. Boles, L.M. Boon, C. Borrone, H.G. Brunner, G.F. Carle, B. Dallapiccola, A. De Paepe, B. Floege, M.L. Halfhide, B. Hall, R.C. Hennekam, T. Hirose, A. Jans, H. Juppner, C.A. Kim, K. Keppler-Noreuil, A. Kohlschuetter, D. LaCombe, M. Lambert, E. Lemyre, T. Letteboer, L. Peltonen, R.S. Ramesar, M. Romanengo, H. Somer, E. Steichen-Gersdorf, B. Steinmann, B. Sullivan, A. Superti-Furga, W. Swoboda, M.J. van den Boogaard, W. Van Hul, M. Vikkula, M. Votruba, B. Zabel, T. Garcia, R. Baron, B.R. Olsen, M.L. Warman, and G. Osteoporosis-Pseudoglioma Syndrome Collaborative, *LDL receptor-related protein 5 (LRP5) affects bone accrual and eye development.* Cell, 2001. **107**(4): p. 513-23.

95. Boyden, L.M., J. Mao, J. Belsky, L. Mitzner, A. Farhi, M.A. Mitnick, D. Wu, K. Insogna, and R.P. Lifton, *High bone density due to a mutation in LDL-receptor-related protein 5.* N Engl J Med, 2002. **346**(20): p. 1513-21.

96. Ellies, D.L., B. Viviano, J. McCarthy, J.P. Rey, N. Itasaki, S. Saunders, and R. Krumlauf, *Bone density ligand, Sclerostin, directly interacts with LRP5 but not LRP5G171V to modulate Wnt activity.* J Bone Miner Res, 2006. **21**(11): p. 1738-49.

97. Semenov, M.V. and X. He, *LRP5 mutations linked to high bone mass diseases cause reduced LRP5 binding and inhibition by SOST.* J Biol Chem, 2006. **281**(50): p. 38276-84.

98. Ai, M., S.L. Holmen, W. Van Hul, B.O. Williams, and M.L. Warman, *Reduced affinity to and inhibition by DKK1 form a common mechanism by which high bone mass-associated missense mutations in LRP5 affect canonical Wnt signaling.* Mol Cell Biol, 2005. **25**(12): p. 4946-55.

99. Zhong, Z., C.R. Zylstra-Diegel, C.A. Schumacher, J.J. Baker, A.C. Carpenter, S. Rao, W. Yao, M. Guan, J.A. Helms, N.E. Lane, R.A. Lang, and B.O. Williams, *Wntless functions in mature osteoblasts to regulate bone mass.* Proc Natl Acad Sci U S A, 2012. **109**(33): p. E2197-204.

100. Kobayashi, Y., S. Uehara, N. Udagawa, and N. Takahashi, *Regulation of bone metabolism by Wnt signals.* J Biochem, 2016. **159**(4): p. 387-92.

101. Kobayashi, Y., G.J. Thirukonda, Y. Nakamura, M. Koide, T. Yamashita, S. Uehara, H. Kato, N. Udagawa, and N. Takahashi, *Wnt16 regulates osteoclast differentiation in conjunction with Wnt5a.* Biochem Biophys Res Commun, 2015. **463**(4): p. 1278-83.

102. Kulkarni, N.H., D.L. Halladay, R.R. Miles, L.M. Gilbert, C.A. Frolik, R.J. Galvin, T.J. Martin, M.T. Gillespie, and J.E. Onyia, *Effects of parathyroid hormone on Wnt signaling pathway in bone.* J Cell Biochem, 2005. **95**(6): p. 1178-90.

103. Holmen, S.L., C.R. Zylstra, A. Mukherjee, R.E. Sigler, M.C. Faugere, M.L. Bouxsein, L. Deng, T.L. Clemens, and B.O. Williams, *Essential role of beta-catenin in postnatal bone acquisition.* J Biol Chem, 2005. **280**(22): p. 21162-8.

104. Kramer, I., C. Halleux, H. Keller, M. Pegurri, J.H. Gooi, P.B. Weber, J.Q. Feng, L.F. Bonewald, and M. Kneissel, *Osteocyte Wnt/beta-catenin signaling is required for normal bone homeostasis.* Mol Cell Biol, 2010. **30**(12): p. 3071-85.

105. Keupp, K., F. Beleggia, H. Kayserili, A.M. Barnes, M. Steiner, O. Semler, B. Fischer, G. Yigit, C.Y. Janda, J. Becker, S. Breer, U. Altunoglu, J. Grunhagen, P. Krawitz, J. Hecht, T. Schinke, E. Makareeva, E. Lausch, T. Cankaya, J.A. Caparros-Martin, P. Lapunzina, S. Temtamy, M. Aglan, B. Zabel, P. Eysel, F. Koerber, S. Leikin, K.C. Garcia, C. Netzer, E. Schonau, V.L. Ruiz-Perez, S. Mundlos, M. Amling, U. Kornak, J. Marini, and B. Wollnik, *Mutations in WNT1 cause different forms of bone fragility.* Am J Hum Genet, 2013. **92**(4): p. 565-74.

106. Pyott, S.M., T.T. Tran, D.F. Leistritz, M.G. Pepin, N.J. Mendelsohn, R.T. Temme, B.A. Fernandez, S.M. Elsayed, E. Elsobky, I. Verma, S. Nair, E.H. Turner, J.D. Smith, G.P. Jarvik, and P.H. Byers, *WNT1 mutations in families affected by moderately severe and progressive recessive osteogenesis imperfecta.* Am J Hum Genet, 2013. **92**(4): p. 590-7.

107. Laine, C.M., K.S. Joeng, P.M. Campeau, R. Kiviranta, K. Tarkkonen, M. Grover, J.T. Lu, M. Pekkinen, M. Wessman, T.J. Heino, V. Nieminen-Pihala, M. Aronen, T. Laine, H. Kroger, W.G. Cole, A.E. Lehesjoki, L. Nevarez, D. Krakow, C.J. Curry, D.H. Cohn, R.A. Gibbs, B.H. Lee, and O. Makitie, *WNT1 mutations in early-onset osteoporosis and osteogenesis imperfecta.* N Engl J Med, 2013. **368**(19): p. 1809-16.

108. Fahiminiya, S., J. Majewski, J. Mort, P. Moffatt, F.H. Glorieux, and F. Rauch, *Mutations in WNT1 are a cause of osteogenesis imperfecta.* J Med Genet, 2013. **50**(5): p. 345-8.

109. Joeng, K.S., Y.C. Lee, M.M. Jiang, T.K. Bertin, Y. Chen, A.M. Abraham, H. Ding, X. Bi, C.G. Ambrose, and B.H. Lee, *The swaying mouse as a model of osteogenesis imperfecta caused by WNT1 mutations.* Hum Mol Genet, 2014. **23**(15): p. 4035-42.

110. Joeng, K.S., Y.C. Lee, J. Lim, Y. Chen, M.M. Jiang, E. Munivez, C. Ambrose, and B.H. Lee, *Osteocyte-specific WNT1 regulates osteoblast function during bone homeostasis.* J Clin Invest, 2017. **127**(7): p. 2678-2688.

111. Ravn, P., S.R. Weiss, J.A. Rodriguez-Portales, M.R. McClung, R.D. Wasnich, N.L. Gilchrist, P. Sambrook, I. Fogelman, D. Krupa, A.J. Yates, A. Daifotis, and G.E. Fuleihan, *Alendronate in early postmenopausal women: effects on bone mass during long-term treatment and after withdrawal. Alendronate Osteoporosis Prevention Study Group.* J Clin Endocrinol Metab, 2000. **85**(4): p. 1492-7.

112. Chavassieux, P.M., M.E. Arlot, C. Reda, L. Wei, A.J. Yates, and P.J. Meunier, *Histomorphometric assessment of the long-term effects of alendronate on bone quality and remodeling in patients with osteoporosis.* J Clin Invest, 1997. **100**(6): p. 1475-80.

113. Teufel, S., B. Grotsch, J. Luther, A. Derer, T. Schinke, M. Amling, G. Schett, D. Mielenz, and J.P. David, *Inhibition of bone remodeling in young mice by bisphosphonate displaces the plasma cell niche into the spleen.* J Immunol, 2014. **193**(1): p. 223-33.

114. Thomas, K.R. and M.R. Capecchi, *Targeted disruption of the murine int-1 proto-oncogene resulting in severe abnormalities in midbrain and cerebellar development.* Nature, 1990. **346**(6287): p. 847-50.

115. Corbin, J.G., N. Gaiano, S.L. Juliano, S. Poluch, E. Stancik, and T.F. Haydar, *Regulation of neural progenitor cell development in the nervous system.* J Neurochem, 2008. **106**(6): p. 2272-87.

116. Engin, F. and B. Lee, *NOTCHing the bone: insights into multi-functionality.* Bone, 2010. **46**(2): p. 274-80.

117. Brennan, A.M. and R.M. Pauli, *Hajdu--Cheney syndrome: evolution of phenotype and clinical problems.* Am J Med Genet, 2001. **100**(4): p. 292-310.

118. Iwaya, T., K. Taniguchi, J. Watanabe, K. Iinuma, Y. Hamazaki, and S. Yoshikawa, *Hajdu-Cheney syndrome.* Arch Orthop Trauma Surg, 1979. **95**(4): p. 293-302.

119. Zhao, W., E. Petit, R.I. Gafni, M.T. Collins, P.G. Robey, M. Seton, K.K. Miller, and M. Mannstadt, *Mutations in NOTCH2 in patients with Hajdu-Cheney syndrome.* Osteoporos Int, 2013. **24**(8): p. 2275-81.

120. Udell, J., H.R. Schumacher, Jr., F. Kaplan, and M.D. Fallon, *Idiopathic familial acroosteolysis: histomorphometric study of bone and literature review of the Hajdu-Cheney syndrome.* Arthritis Rheum, 1986. **29**(8): p. 1032-8.

121. Nunziata, V., G. di Giovanni, P. Ballanti, and E. Bonucci, *High turnover osteoporosis in acro-osteolysis (Hajdu-Cheney syndrome).* J Endocrinol Invest, 1990. **13**(3): p. 251-5.

122. Canalis, E., L. Schilling, S.P. Yee, S.K. Lee, and S. Zanotti, *Hajdu Cheney Mouse Mutants Exhibit Osteopenia, Increased Osteoclastogenesis, and Bone Resorption.* J Biol Chem, 2016. **291**(4): p. 1538-51.

123. Jarriault, S., C. Brou, F. Logeat, E.H. Schroeter, R. Kopan, and A. Israel, *Signalling downstream of activated mammalian Notch.* Nature, 1995. **377**(6547): p. 355-8.

124. Maier, M.M. and M. Gessler, *Comparative analysis of the human and mouse Hey1 promoter: Hey genes are new Notch target genes.* Biochem Biophys Res Commun, 2000. **275**(2): p. 652-60.

125. Feng, W., H. Liu, T. Luo, D. Liu, J. Du, J. Sun, W. Wang, X. Han, K. Yang, J. Guo, N. Amizuka, and M. Li, *Combination of IL-6 and sIL-6R differentially regulate varying levels of RANKL-induced osteoclastogenesis through NF-kappaB, ERK and JNK signaling pathways.* Sci Rep, 2017. **7**: p. 41411.

126. Nakashima, T., Y. Kobayashi, S. Yamasaki, A. Kawakami, K. Eguchi, H. Sasaki, and H. Sakai, *Protein expression and functional difference of membrane-bound and soluble receptor activator of NF-kappaB ligand: modulation of the expression by osteotropic factors and cytokines.* Biochem Biophys Res Commun, 2000. **275**(3): p. 768-75.

127. Zanotti, S., J. Yu, A. Sanjay, L. Schilling, C. Schoenherr, A.N. Economides, and E. Canalis, *Sustained Notch2 signaling in osteoblasts, but not in osteoclasts, is linked to osteopenia in a mouse model of Hajdu-Cheney syndrome.* J Biol Chem, 2017. **292**(29): p. 12232-12244.

128. Drake, W.M., M.P. Hiorns, and D.L. Kendler, *Hadju-Cheney syndrome: response to therapy with bisphosphonates in two patients.* J Bone Miner Res, 2003. **18**(1): p. 131-3.

129. Hwang, S., D.Y. Shin, S.H. Moon, E.J. Lee, S.K. Lim, O.H. Kim, and Y. Rhee, *Effect of zoledronic acid on acro-osteolysis and osteoporosis in a patient with Hajdu-Cheney syndrome.* Yonsei Med J, 2011. **52**(3): p. 543-6.

130. McKiernan, F.E., *Integrated anti-remodeling and anabolic therapy for the osteoporosis of Hajdu-Cheney syndrome.* Osteoporos Int, 2007. **18**(2): p. 245-9.

131. Adami, G., M. Rossini, D. Gatti, G. Orsolini, L. Idolazzi, O. Viapiana, A. Scarpa, and E. Canalis, *Hajdu Cheney Syndrome; report of a novel NOTCH2 mutation and treatment with denosumab.* Bone, 2016. **92**: p. 150-156.

132. Cummings, S.R., J. San Martin, M.R. McClung, E.S. Siris, R. Eastell, I.R. Reid, P. Delmas, H.B. Zoog, M. Austin, A. Wang, S. Kutilek, S. Adami, J. Zanchetta, C. Libanati, S. Siddhanti, C. Christiansen, and F. Trial, *Denosumab for prevention of fractures in postmenopausal women with osteoporosis.* N Engl J Med, 2009. **361**(8): p. 756-65.

133. Rao, T.P. and M. Kuhl, *An updated overview on Wnt signaling pathways: a prelude for more.* Circ Res, 2010. **106**(12): p. 1798-806.

134. Schulze, J., S. Seitz, H. Saito, M. Schneebauer, R.P. Marshall, A. Baranowsky, B. Busse, A.F. Schilling, F.W. Friedrich, J. Albers, A.S. Spiro, J. Zustin, T. Streichert, K. Ellwanger, C. Niehrs, M. Amling, R. Baron, and T. Schinke, *Negative regulation of bone formation by the transmembrane Wnt antagonist Kremen-2.* PLoS One, 2010. **5**(4): p. e10309.

135. Palomo, T., T. Vilaca, and M. Lazaretti-Castro, *Osteogenesis imperfecta: diagnosis and treatment.* Curr Opin Endocrinol Diabetes Obes, 2017. **24**(6): p. 381-388.

136. Grafe, I., T. Yang, S. Alexander, E.P. Homan, C. Lietman, M.M. Jiang, T. Bertin, E. Munivez, Y. Chen, B. Dawson, Y. Ishikawa, M.A. Weis, T.K. Sampath, C. Ambrose, D. Eyre, H.P. Bachinger, and B. Lee, *Excessive transforming growth factor-beta signaling is a common mechanism in osteogenesis imperfecta.* Nat Med, 2014. **20**(6): p. 670-5.

137. Grafe, I., S. Alexander, T. Yang, C. Lietman, E.P. Homan, E. Munivez, Y. Chen, M.M. Jiang, T. Bertin, B. Dawson, F. Asuncion, H.Z. Ke, M.S. Ominsky, and B. Lee, *Sclerostin Antibody Treatment Improves the Bone Phenotype of Crtap(-/-) Mice, a Model of Recessive Osteogenesis Imperfecta.* J Bone Miner Res, 2016. **31**(5): p. 1030-40.

138. Keller, H. and M. Kneissel, *SOST is a target gene for PTH in bone.* Bone, 2005. **37**(2): p. 148-58.

139. Silva, B.C. and J.P. Bilezikian, *Parathyroid hormone: anabolic and catabolic actions on the skeleton.* Curr Opin Pharmacol, 2015. **22**: p. 41-50.

140. Valimaki, V.V., O. Makitie, R. Pereira, C. Laine, K. Wesseling-Perry, J. Maatta, M. Kirjavainen, H. Viljakainen, and M.J. Valimaki, *Teriparatide Treatment in Patients With WNT1 or PLS3 Mutation-Related Early-Onset Osteoporosis: A Pilot Study.* J Clin Endocrinol Metab, 2017. **102**(2): p. 535-544.

141. Yen, W.C., M.M. Fischer, F. Axelrod, C. Bond, J. Cain, B. Cancilla, W.R. Henner, R. Meisner, A. Sato, J. Shah, T. Tang, B. Wallace, M. Wang, C. Zhang, A.M. Kapoun, J. Lewicki, A. Gurney, and T. Hoey, *Targeting Notch signaling with a Notch2/Notch3 antagonist (tarextumab) inhibits tumor growth and decreases tumor-initiating cell frequency.* Clin Cancer Res, 2015. **21**(9): p. 2084-95.

142. Schindelin, J., I. Arganda-Carreras, E. Frise, V. Kaynig, M. Longair, T. Pietzsch, S. Preibisch, C. Rueden, S. Saalfeld, B. Schmid, J.Y. Tinevez, D.J. White, V. Hartenstein, K. Eliceiri, P. Tomancak, and A. Cardona, *Fiji: an open-source platform for biological-image analysis.* Nat Methods, 2012. **9**(7): p. 676-82.

143. Sanger, F., S. Nicklen, and A.R. Coulson, *DNA sequencing with chain-terminating inhibitors.* Proc Natl Acad Sci U S A, 1977. **74**(12): p. 5463-7.

144. Bradford, M.M., *A rapid and sensitive method for the quantitation of microgram quantities of protein utilizing the principle of protein-dye binding.* Anal Biochem, 1976. **72**: p. 248-54.

145. Ishii, I., B. Friedman, X. Ye, S. Kawamura, C. McGiffert, J.J. Contos, M.A. Kingsbury, G. Zhang, J.H. Brown, and J. Chun, *Selective loss of sphingosine 1-phosphate signaling with no obvious phenotypic abnormality in mice lacking its G protein-coupled receptor, LP(B3)/EDG-3.* J Biol Chem, 2001. **276**(36): p. 33697-704.

146. Clausen, B.E., C. Burkhardt, W. Reith, R. Renkawitz, and I. Forster, *Conditional gene targeting in macrophages and granulocytes using LysMcre mice.* Transgenic Res, 1999. **8**(4): p. 265-77.

147. Milovanovic, P., E.A. Zimmermann, C. Riedel, A. vom Scheidt, L. Herzog, M. Krause, D. Djonic, M. Djuric, K. Puschel, M. Amling, R.O. Ritchie, and B. Busse, *Multi-level characterization of human femoral cortices and their underlying osteocyte network reveal trends in quality of young, aged, osteoporotic and antiresorptive-treated bone.* Biomaterials, 2015. **45**: p. 46-55.

148. Roschger, P., P. Fratzl, J. Eschberger, and K. Klaushofer, *Validation of quantitative backscattered electron imaging for the measurement of mineral density distribution in human bone biopsies.* Bone, 1998. **23**(4): p. 319-26.

149. Roschger, P., E.P. Paschalis, P. Fratzl, and K. Klaushofer, *Bone mineralization density distribution in health and disease.* Bone, 2008. **42**(3): p. 456-66.

10 Appendix

10.1 List of hazardous substances used in the study according to GHS

All chemicals were used according to safety data sheets.

10.1.1 Hazard (H)- and precautionary (P) phrases

Chemicals	CAS #	H-Phrases	P-Phrases
(2E)-3-(4-Hydroxyphenyl)-prop-2-enoic acid	501-98-4	315-319-335	261-305+351+338
1,2-dihydroxyanthraquinon	72-48-0	302	305+351+338
1,4-Dimethylbenzene	95-47-6	226-304-312+332-315-319-335-412-	210-261-273-301+310-302+352-312-331
1α,25-Dihydroxyvitamin-D_3	67-97-0	330-311-301-372	280-304+340-302+352-309+310
3',3",5',5"-tetrabromophenol-sulfonphthalein	115-39-9		
4-(2-hydroxyethyl)-1-piperazineethanesulfonic acid	7365-45-9		
5-Amino-2,3-dihydrophthalazine-1,4-dione	521-31-3	315-319-335	261-305+351+338
Acetic acid	64-19-7	226-290-314	210-280-301+330+331-305+351+338-308-310
Acid fuchsin	3244-88-0	315-319-335	261-305+351+338
Agarose (SeaKem® LE)	9012-36-6		
Ammonium hydroxide	1336-21-6	290-314-335-400	260-273-280-301+330+331-303+361+353-305+351+338
Ammonium persulfate	7727-54-0	272-302-315-317-319-334-335	220-261-280-305+351+338-342+311
Benzoyl peroxide	94-36-0	241-317-319-410	210-261-273-280-305+351+338-333+313-420-501
Carbon dioxide	124-38-9	280	403
Diethyl pyrocarbonate	1609-47-8	302-315-319-335	261-305+351+338
Dimethyl sulfoxide	67-68-5		
Dithiothreitol	7634-42-6	302-315-319-335	261-305+351+338
Ethanol	64-17-5	225-319	210-240-305+351+338-403+233
Ethylenediaminetetraacetic acid	60-00-4	319	305+351+338
Fast Red Violet LB Salt	32348-81-5	302+312+332-351	261-280-301+312+330
Formaldehyde	50-00-0	301+311+331-314-317-335-341-350-370	201-260-280-301+310-330-303+361+353-304+340-310-305+351+338-308+310-403+233
Glycerol	56-81-5		
Glycin	56-40-6		
Hydrochloric acid	7647-01-0	290-314-335	260-280-303+361+353-304+340+310-305+351+338
Hydrogen peroxide	7722-84-1	271-302-314-332-335-412	280-305+351+338-310
Isopropyl alcohol	67-63-0	225-319-336	210-233-240-305+351+338-403+235
L-Ascorbic acid	50-81-7		
Magnesium chloride	7791-18-6		

Methanol	67-56-1	225-331-311-301-370	210-233-280-302+352-304+340-308+310-403+235
Methyl methacrylate	80-62-6	225-315-317-335	210-233-280-302+351-304+340-403+235
Monoglycol butylether	111-76-2	302-311-331-315-319	261-270-280-301+312-302+352-305+351+338
N,N-Dimethyl formamide	68-12-2	226-312-332-319-360D	201-210-302+352-304+340-305+351+338-308+313
N,N-Dimethyl-p-toluidine	99-97-8	301-311-373-412	261-273-280-301+310-311
Nitric acid	7697-37-2	272-290-331-314	280-301+330+331-305+351+338-308+310
Nitrogen	7727-37-9	280	403
Nonyl phenoxypolyethoxyl-ethanol	9016-45-9	302+332-318-411	273-280-305+351+338
Nonylphenyl-polyethylenglycol-acetate	54612-40-7	-	260-262
Penicillin	118-53-6	315-317-320-334-335-361	264-304+340-305+351+338-312-337+313-332+313
Picric acid	88-89-1	201-301-311-331	210-280-301+310-312
Polyoxyethylene (20) sorbitan monolaurat	9005-64-5		
Potassium chloride	7447-40-7		
Potassium phosphate	7778-53-2	318-335	280-304+340+312-305+351+338
Prop-2-enamide	79-06-1	301-312-332-315-317-319-340-350-361f-372	201-280-302+352-304+340-305+351+338-308+310
Silver nitrate	7761-88-8	272-290-314-410	210-220-260-280-305+351+338-370+378-308+310
Sodium acetate	6131-90-4		
Sodium carbonate	5968-11-6-	319	260-305+351+338
Sodium chloride	7647-14-5		
Sodium deoxycholate	302—95-4	302-315-319	280-302+352-305+351+338
Sodium dodecyl sulfate	151-21-3	228-302+332-315-318-335-412	210-261-280-301+312+330-301+312+330-305+351+338+310-370+378
Sodium hydrogen carbonate	144-55-8		
Sodium hydroxide	23340-32-1	290-314	280-301+330+331-305+351+338-308+310
Sodium hypochloride	7681-52-9	314-400	260-280-303+361+353-304+340+310+305+351+338
Sodium phosphate	7601-54-9	315-319-335	261-305+351+338
Sodium tartrate	51307-92-7		
Streptomycin	57-92-1	302-361	281
Tetramethylethylenediamine	110-18-9	225-332-302-314	210-280-305+351+338-310
Toluidin blue O	92-31-9		
Tris(hydroxymethyl)amino-methane base	77-86-1	315-319-335	261-305+351+338
Tris(hydroxymethyl)amino-methane hydrochloride	1185-53-1	315-319-335	261-305+351+338
β-Mercapto ethanol	60-24-2	301+331-310-315-317-318-373-410	273-280-302+352-304+340-305+351+338-308+310

10.1.1.1 List of hazard statements

201	Explosive; mass explosion hazard
225	Highly flammable liquid and vapour
226	Flammable liquid and vapour
228	Flammable solid
241	Heating may cause a fire or explosion
271	May cause fire or explosion; strong oxidizer
272	May intensify fire; oxidizer
280	Contains gas under pressure; may explode if heated
290	May be corrosive to metals
301	Toxic if swallowed
302	Harmful if swallowed
304	May be fatal if swallowed and enters airways
311	Toxic in contact with skin
312	Harmful in contact with skin
314	Causes severe skin burns and eye damage
315	Causes skin irritation
317	May cause an allergic skin reaction
318	Causes serious eye damage
319	Causes serious eye irritation
320	Causes eye irritation
330	Fatal if inhaled
331	Toxic if inhaled
332	Harmful if inhaled
334	May cause allergy or asthma symptoms or breathing difficulties if inhaled
335	May cause respiratory irritation
336	May cause drowsiness or dizziness
340	May cause genetic defects
341	Suspected of causing genetic defects
350	May cause cancer
351	Suspected of causing cancer
360	May damage fertility or the unborn child
361	Suspected of damaging fertility or the unborn child
370	Causes damage to organs
372	Causes damage to organs through prolonged or repeated exposure
373	May cause damage to organs through prolonged or repeated exposure
400	Very toxic to aquatic life
410	Very toxic to aquatic life with long lasting effects
411	Toxic to aquatic life with long lasting effects
412	Harmful to aquatic life with long lasting effects

10.1.1.2 List of precautionary statements

201	Obtain special instructions before use
210	Keep away from heat/sparks/open flames/hot surfaces – No smoking
220	Keep/Store away from clothing/.../combustible materials
233	Keep container tightly closed
235	Keep cool
240	Ground/bond container and receiving equipment
260	Do not breathe dust/fume/gas/mist/vapours/spray
261	Avoid breathing dust/fume/gas/mist/vapours/spray
262	Do not get in eyes, on skin, or on clothing
264	Wash ... thoroughly after handling
270	Do not eat, drink or smoke when using this product
273	Avoid release to the environment
280	Wear protective gloves/protective clothing/eye protection/face protection
281	Use personal protective equipment as required
301	IF SWALLOWED:
302	IF ON SKIN:
303	IF ON SKIN (or hair):
304	IF INHALED:
305	IF IN EYES:
308	IF exposed or concerned:
309	IF exposed or you feel unwell:
310	Immediately call a POISON CENTER or doctor/physician
311	Call a POISON CENTER or doctor/physician
312	Call a POISON CENTER or doctor/physician if you feel unwell
313	Get medical advice/attention
330	Rinse mouth
331	Do NOT induce vomiting
332	If skin irritation occurs:
333	If skin irritation or a rash occurs:
337	If eye irritation persists:
338	Remove contact lenses if present and easy to do. continue rinsing
340	Remove victim to fresh air and keep at rest in a position comfortable for breathing
342	If experiencing respiratory symptoms:
351	Rinse continuously with water for several minutes
352	Wash with soap and water
353	Rinse skin with water/shower
361	Remove/Take off immediately all contaminated clothing
370	In case of fire:
378	Use ... for extinction
403	Store in a well ventilated place
420	Store away from other materials
501	Dispose of contents/container to ...

11 Danksagungen

In erster Linie bedanke ich mich bei **Prof. Dr. Thorsten Schinke** und **Prof. Dr. Michael Amling** für die Möglichkeit, meine Promotion am Institut für Osteologie und Biomechanik durchzuführen. Außerdem danke ich speziell Prof. Dr. Thorsten Schinke für die Bereitstellung des spannenden Themas, die stetige Unterstützung und Hilfsbereitschaft, sowie die anregenden Diskussionen während der letzten Jahre.

Großer Dank geht ebenfalls an **Prof. Dr. Peter Heisig** für die Übernahme des Zweitgutachtens, sowie die spannenden Diskussionen im Rahmen meiner Fortschrittsberichte in seinem Arbeitskreis.

Des Weiteren möchte ich mich bei **Prof. Dr. Boris Fehse**, **Dr. Kerstin Cornils** und **Tanja Sonntag** für die Zusammenarbeit bei den Knochenmarktransplantationen, bei **Dr. Ioanna Triviai** für die Unterstützung bei Knochenmarksuntersuchungen, bei **Prof. Dr. Meliha Karsak** und **Dr. Ahmed Sharaf** für die Zusammenarbeit bei den Hirnanalysen und bei **Felix Schmidt** und **Kilian Stockhausen** für die Hilfe bei den Knochenqualitätsuntersuchungen bedanken.

Ein weiteres großes Dankeschön geht an alle Mitglieder des IOBMs, insberondere **Dr. Timur Yorgan**, **Dr. Anke Jeschke**, **Dr. Julia Luther**, **Dr. Jean-Pierre David**, **Dr. Gretl Hendrickx**, **Mona Neven**, **Lana Rosenthal**, **Nannan Liao**, **Dr. Laura Brylka**, **Claudia Reymers**, **Olga Winter**, **Marion Dietzmann** und **Elke Leicht** für jegliche Art von Hilfe und Unterstützung, sowie das tolle Arbeitsklima.

Den Tierpflegern des UKE´s, insbesondere **Maria Seidl-Steiner**, **Philipp Missberger** und **Gudrun Arndt**, danke ich für die allzeit freundliche Kooperation und die zuverlässige Verwaltung und Pflege der Mauslinien.

Zu guter Letzt danke ich meinem Freund, meinen Freunden und meiner Familie, die mich während der gesamten Zeit unterstützt und motiviert haben.

12 Eidesstattliche Versicherung

Hiermit versichere ich an Eides statt, die vorliegende Dissertation selbst verfasst und keine anderen als die angegebenen Hilfsmittel benutzt zu haben. Die eingereichte schriftliche Fassung entspricht der auf dem elektronischen Speichermedium. Ich versichere, dass diese Dissertation nicht in einem früheren Promotionsverfahren eingereicht wurde.

I hereby declare on oath, that I have written the present dissertation by my own and have not used other than the acknowledged resources and aids. The submitted written version corresponds to the version on the electronic storage medium. I hereby declare that I have not previously applied or pursued for a doctorate (Ph.D. studies).

Date

Signature